Universita' degli Studi di Napoli Federico II
Scuola di Dottorato in Ingegneria Industriale
Dottorato di Ricerca in Ingegneria Chimica - XXVI ciclo

Numerical simulations of deformable systems in flowing media

Tesi di Dottorato di
Massimiliano M. Villone

Comitato Scientifico

prof. ing. Pier Luca Maffettone
Universita' degli Studi di Napoli Federico II

dr. Francesco Greco
Istituto di Ricerche sulla Combustione - CNR

dr. ir. Martien A. Hulsen
prof. dr. ir. Patrick D. Anderson
Technische Universiteit Eindhoven

Contents

Abstract

Over the last 15 years, microfluidics has gained an increasing importance. In several microfluidic systems, as cytometric, sorting and diagnostic devices, suspensions of particles flow in miniaturized channels. In such a situation, a wide range of phenomena can arise due to the deformability and the elasticity of the suspended objects, the geometry of the channels, the interactions between the objects and the walls of the flow cells, and the complexity of the suspending media.

Aim of the present thesis is of developing and applying a finite element method-based code to study the dynamics of soft systems suspended in Newtonian and viscoelastic fluids under flow.

The code is developed by adapting and extending an arbitrary Lagrangian Eulerian finite element method based numerical code for viscoelastic fluids using well-known stabilization techniques (SUPG, DEVSS, log-conformation), and it is validated for drops and elastic particles in unbounded shear flow by comparison with available theoretical, experimental and numerical results. Then, a single-body problem is considered: the behavior of an initially spherical elastic particle suspended in confined shear flow of a Newtonian and a Giesekus viscoelastic liquid is studied. Finally, a multi-body system is investigated: the bulk linear viscoelastic properties of monodisperse emulsions of Newtonian drops in a Newtonian matrix are computed.

Chapter 1

Introduction

Microfluidics, i.e., the processing of fluids in channels which have a characteristic length in the order of microns, has gained an increasing importance over the last 15 years. In several microfluidic systems, such as cytometric, sorting and diagnostic devices, suspensions of particles flow in miniaturized channels (see, for example, [28, 81]). In such a situation, a wide range of phenomena can arise due to the deformability and the elasticity of the suspended objects, the geometry of the channels, the interactions between the objects and the walls of the flow cells, and the complexity of the suspending media.

1.1 Overview of the systems of interest

In the present work, with the generic term of 'soft system', several classes of systems are designated, like drops, elastic particles, capsules, and vesicles. A scheme of the general features of each class is reported in Table 1.1. Such objects are of interest from both a scientific and a technological point of view, since drops are major constituents of emulsions, elastic particles are present, for example, in filled polymers and are also models for more complicated systems (e.g., white blood cells), capsules and vesicles are models for red blood cells (RBCs) and vectors for controlled release drugs.

system	features
drops	bulk liquid objects, spherical undeformed shape, constant volume.
elastic particles	bulk elastic solid systems, constant volume.
capsules	liquid drops wrapped in thin elastic membranes, constant volume, variable surface area.
vesicles	liquid drops wrapped in thin elastic membranes, constant volume, constant surface area.

Table 1.1: Classification of soft systems.

In a large proportion of applications, the undeformed shape of the systems of our interest is ellipsoidal, thus being identified by the 3 semiaxes L, B and W, as shown in Figure 1.1; a sphere can be seen as a particular ellipsoid, for which $L = B = W$. When two of its three semiaxes have the same length, an ellipsoid can be also called spheroid. A spheroid for which $L > B = W$ is said prolate, and has a shape similar to that of a a cigar, whereas one for which $L = W > B$ is called oblate and has a lentil-like shape.

Numerous are the geometrical and physical parameters of interest for describing the dynamics of spheroidal deformable particles suspended in fluids under flow. It is worth to cite the deformation parameters (combinations of the lengths of the axes), the excess area, which is the surface area in excess with respect to a sphere with the same volume of the ellipsoid, the orientation angles with respect to flow direction and vorticity, the viscosity ratio between the suspended and the suspending phase (in case a drop is considered), the elastic modulus (in case an elastic particle is considered), the capillary number, which modulates the intensity of the flow, and the degree

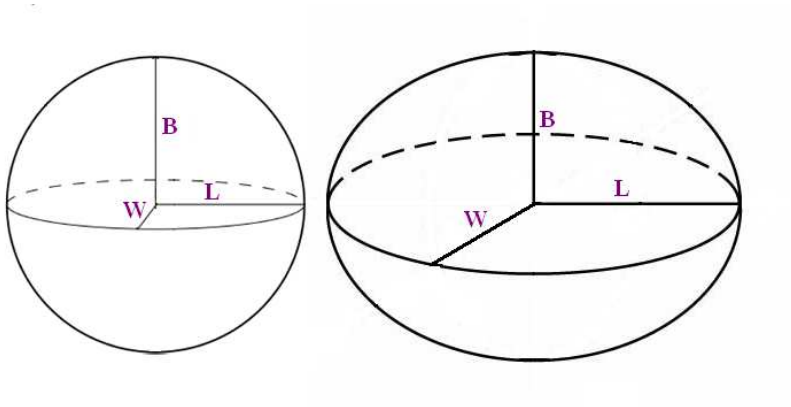

Figure 1.1: Schematic representation of some common undeformed shapes of soft systems.

of confinement, which is the ratio between the characteristic dimension of the suspended object and the characteristic dimension of the channel where it flows.

1.2 State of art

As reported above, many kinds of systems can be ascribed to the category of soft systems. In the present state, the greatest part of the scientific literature concerns drops.

1.2.1 Drops

The literature on the behavior of drops in flow is wide and dates back to the experimental work performed by Taylor in the 30^{s} of the 20^{th} century (see [94]), that studies the deformation of Newtonian drops in a Newtonian fluid under simple shear flow in the low capillary number regime (for drops, the capillary number is defined as $Ca = \eta_{\text{e}} R_0 \dot{\gamma}/\Gamma$, where η_{e} is the ambient fluid viscosity, R_0 is the radius of the undeformed (spherical) drop, $\dot{\gamma}$ is the shear rate and Γ is the surface tension between the two fluids). Drops are found to deform and assume an ellipsoidal shape, with the Taylor deformation

parameter D (defined as the ratio between the difference and the sum of the lengths of the major and the minor semiaxis of the ellipsoid in the shear plane) linearly depending on Ca according to the law:

$$D = \frac{19\lambda + 16}{16\lambda + 16} Ca \tag{1.1}$$

where λ is the viscosity ratio. The law is valid for Ca up to about 0.5. From then on, much has been done regarding drops from a theoretical, experimental and computational point of view, considering different flow fields and constitutive behaviors of the fluids.

In a Newtonian matrix under unconfined shear, a Newtonian drop deforms and attains a steady ellipsoidal shape with a fixed orientation angle θ with respect to the flow direction. The deformation of the drop increases with Ca; on the other hand, the angle decreases with it (see, for example, [49, 6, 7]). If λ is less than about 4, when Ca reaches a critical value, the surface tension is no more capable of contrasting the deformation and the drop breaks up [58]; on the contrary, above such critical λ-value, the drop does not break up even at high Ca-values: several papers focus on identifying $\lambda - Ca$ break-up conditions (see, for example, [18, 6, 19]). A typical feature of deformed drops in shear is circulation of the internal liquid; Pozrikidis [83] showed that the presence of interfacial viscosity suppresses the above mentioned vortices and reduces the magnitude of the deformation. A simple model that well describes the behavior of Newtonian drops in a Newtonian fluid under several 'slow' flow conditions has been developed by Maffettone and Minale [72]. The presence of solid walls in the vicinity of the drop can influence its deformation considerably: Shapira and Haber [92] computed analytically the shape of a Newtonian drop suspended near a solid wall in a Newtonian matrix in shear flow; very elongated non-ellipsoidal deformed shapes have been detected experimentally in confined shear flows (see, for example, [93]).

A rich phenomenology is also found in inertialess Poiseuille flow, i.e., drop lateral migration towards the region of the channel at lowest shear rate, which is its centerline [67, 44]. In the presence of surfactants on the surface of the

drop, migration towards the center still exists [55], but migration towards the walls can also be seen, as reported by Guido and Preziosi in their review [47]. If the system presents strong inertial effects, drops undergo an effect that is well known for solid particles as 'Segre-Silberberg effect', consisting in lateral migration towards a position in between the centerline and the wall [73].

If one considers the possibility that one of the two fluids, or both, is complex, and in particular viscoelastic, three cases can be distinguished: a viscoelastic drop in a Newtonian matrix (V/N), a Newtonian drop in a viscoelastic matrix (N/V), and a viscoelastic drop in a viscoelastic matrix (V/V). A new parameter has, then, to be taken into account, that measures the elasticity of the complex fluid, e.g., the Deborah number De, which is the ratio between the fluid and the flow characteristic times. On whatever side viscoelasticity acts, in shear flow, the steady orientation angle of the drop is lower than in the corresponding N/N case (see, for example, [43, 48]); a simple phenomenological model for drops under all flow conditions in the small deformation regime, which can handle viscoelasticity in both the matrix and the dispersed phase, has been developed by Maffettone and Greco [71]. For a viscoelastic drop suspended in a Newtonian fluid under shear flow, in the subcritical λ-range, elasticity is found to promote a decrease in the steady D- and θ-values, and an increase in the break-up Ca-value with respect to the corresponding N/N system [1]; fixed a value of the capillary number Ca, D decreases when increasing the Deborah number De [74]. If a Newtonian drop is suspended in a viscoelastic matrix in shear, the dynamics of its deformation and its steady state are significantly influenced by the complexity of the suspending fluid: in the startup of the process, non-Newtonian effects result in a deformation overshoot [93, 87], then, if the flow is stopped, the drop retracts in two steps due to its finite relaxation time [88, 97]. The steady D and θ are lower then the corresponding N/N case. Finally, a viscoelastic drop suspended in a viscoelastic fluid in shear shows some peculiar deformed structures which are not seen in the other above mentioned situations, such

as sheets, fibers or hooks [65, 14]. The presence of viscoelasticity on both sides is found to contrast or promote break-up depending on De [2].

Recently, lateral migration has been observed also for viscoelastic drops in confined shear [75] and Poiseuille flow [62].

1.2.2 Emulsions

Emulsions are heterogeneous systems constituted by liquid drops suspended in a continuous liquid phase, usually referred as 'matrix'. These systems are of outstanding scientific interest, since emulsions are found in several technological fields, as polymer processing, pharmaceutics, body care, and foods. Due to such wide variety of applications, in the last decades emulsions have been extensively studied, both from the theoretical and the experimental point of view.

Numerous works focus on emulsion bulk rheology. From the early work of Taylor [94], who extended the Einstein formula for the viscosity of a dilute suspension of rigid spheres to the case of dilute emulsions, it is known that the volume fraction of drops ϕ and the viscosity ratio λ between the dispersed and the continuous phase are key factors in the determination of bulk quantities such as viscosity, viscoelastic *moduli*, and normal stress differences. Taylor formula for the overall viscosity η of an emulsion of Newtonian drops in a Newtonian fluid has been experimentally verified by Nawab and Mason [77] for λ in the range 0.5 - 5, and empirically extended by Pal [79] outside the dilute regime. Commonly, an emulsion is defined 'dilute' for $\phi < 0.05$, 'semi-dilute' for $0.05 \leq \phi < 0.10$ and 'concentrated' for drop volume concentrations larger than 0.10.

When liquid drops are suspended in another liquid, even if the two fluids are Newtonian, the emulsion shows typical viscoelastic properties (e.g., see Larson [63]), such as nonzero elastic modulus and normal stress differences. By using a cell model approach, Oldroyd [78] derived general theoretical predictions of the linear viscoelastic properties of Newtonian/Newtonian emulsions, but concluded that those predictions are valid only in the dilute

regime. Further calculations were performed a couple of decades later by Choi and Schowalter [16]. Oldroyd's equations have been, then, generalized by Palierne [80] and Bousmina [10] to the case of viscoelastic suspended phase and matrix. All the above mentioned works refer to monodisperse emulsions, which are actually not simple to get in practice. Graebling et al. [41] adapted Palierne model to polydisperse systems.

In the literature, numerous works are present regarding emulsions where at least one phase is rheologically complex, with much attention devoted, in particular, to polymer blends (see, for example, [60, 98, 96, 20, 54]); on the contrary, very few experimental data are available on the linear viscoelasticity of emulsions of Newtonian drops in Newtonian matrices, at least under non-vanishing ϕ-conditions (a measure for a blend of nearly Newtonian polymers is given in [27]).

Another interesting phenomenon is that of interfacial slip, namely, that on in the interface that separates each drop from the suspending matrix the tangential components of the velocity in the two phases do not coincide. Such phenomenon is known to be responsible for the decrease in the viscosity of some polymer blends with respect to the individual viscosities of the constituent fluids: experimental observations (e.g., [68, 70, 11, 103, 64, 82, 61]) as well as theoretical models [78, 86, 85] are available on that.

1.2.3 Elastic particles

A somewhat limited attention has been devoted to such systems in the research literature; for sure, a wide comprehension of their mechanical behavior in flow is still lacking. In 1946, Fröhlich and Sack [34] investigated a suspension of elastic spheres in a Newtonian fluid under extensional flow, and derived an expression for the extensional stress of the suspension as a function of the strain rate. In 1967, Roscoe [90] studied theoretically the behavior of a dilute suspension of (visco)elastic spheres in a Newtonian fluid subjected to shear flow, predicting that the deformed particles attain a steady state, where they show an ellipsoidal shape with a fixed orientation with respect

to the flow; the author also gave quantitative predictions of the deformation of the suspended particles, the stress, and the viscosity of the suspension as a function of the flow conditions and the constitutive properties of the particles and the suspending fluid. In the same year, Goddard and Miller [39] derived a constitutive equation for dilute suspensions of slightly deformed elastic spheres. In 1981, Murata [76] studied the small deformation of an initially spherical elastic particle in an arbitrary weak flow of a Newtonian fluid by means of a perturbative analysis. Since then, very little has been done on elastic particles until the end of the last decade, when Gao and Hu [35] performed 2D arbitrary Lagrangian Eulerian finite element method (ALE FEM) simulations. In 2011, the same group [36] studied the behavior of an initially spherical elastic particle suspended in a Newtonian fluid in shear flow through a non-perturbative method [30, 31], coming to a validation and an extension of Roscoe results. More recently, the have focused their attention on the dynamics of elastic objects with non-spherical undeformed shape (i.e., ellipsoids) in sheared Newtonian fluids [37], and detected that, depending on the geometrical and physical parameters that describe the system, the particles undergo different regimes of motion, namely, steady state (SS), where the deformation and orientation angle of the particle with respect to the flow direction are fixed, tumbling (TU), where the whole object periodically rotates around the vorticity axis, and trembling (TR), where the orientation angle oscillates around a mean value.

1.2.4 Vesicles and capsules

Several theoretical, experimental, and numerical works are available concerning the deformation of vesicles and capsules in Newtonian fluids under unconfined shear flow, as reported in their review by Finken et al. [33]. Depending on the physical parameters that rule the system, different regimes of motion of such objects are detected, as stationary tank treading (TT), where the orientation angle of the vesicle/capsule with respect to the flow direction is fixed and the elastic membrane rotates around the internal fluid like the treads of

a tank, tumbling (TU), described above for elastic ellipsoids, vacillating-breathing (VB) (also known as oscillating (OS)), where the orientation angle oscillates around a mean value, and some intermittent regimes, that consist in a time evolution of the motion regime (e.g., $TU \rightarrow VB \rightarrow TT$). Stationary TT and TU being the two extreme behaviors, an increase in λ is found to promote TT, whereas an increase in flow intensity promotes TU.

A considerable amount of papers is also available on inertialess Poiseuille flow of vesicles (see, for example, [57, 17, 56]) and capsules (e.g., [84, 3, 29, 66]) in Newtonian fluids. The same regimes as above are detected, and, in addition, lateral migration is seen. The latter is always directed towards the centerline of the flow cell, where the shear rate is the the lowest and the object can minimize distortion. TU vesicles and capsules are found to migrate more slowly than TT ones. The migration rate is influenced by the physical parameters of the system: specifically, it increases with an increase in the shear rate and a decrease in the viscosity ratio or the membrane shear modulus. In very confined systems, i.e., where the characteristic dimension of the object is 0.7 - 0.8 times the characteristic dimension of the flow channel, and at large flow intensities, vesicles are found to assume parachute-like shapes [99, 89]. Such shapes are characteristic of RBCs flowing in capillaries; literature on those is very wide, but an analysis of it goes beyond the scope of this work.

1.3 Aim of the work

Aim of the present thesis is of developing and applying a code to simulate the dynamics of deformable systems suspended in flowing Newtonian and viscoelastic liquids. The thesis is organized as follows: in Chapter 2, the method is explained in detail and tested for drops and elastic particles in unbounded shear flow; in Chapter 3, the behavior of a single elastic particle suspended in Newtonian and viscoelastic fluids under confined shear flow is examined; in Chapter 4, a multi-body problem is considered, i.e., the small

amplitude oscillatory shear (SAOS) flow of an emulsion of Newtonian drops in a Newtonian matrix; finally, in Chapter 5, some conclusions are drawn, and future perspectives are outlined.

1.4 Numerical methods for the simulation of deformable systems

As we aim at developing a code for the simulation of deformable systems in complex fluids, it is worth dwelling briefly on the review of the numerical techniques employed in the literature.

For the numerical solution of problems modeled by linear differential equations, such as those involving Newtonian drops, vesicles, and capsules in Newtonian matrices, the most common choice is that of recurring to the boundary element/boundary integral methods (BEM/BIM) (for drops, see, for example, [6, 58, 67, 44, 55, 73]; for vesicles/capsules, [57, 17, 84]), whose greatest advantage is of only requiring discretization at the interface between the suspended object and the suspending medium (thus, a surface in 3D and a line in 2D or axisymmetric geometries): this allows for great computational saving, and very detailed description of the shape of the interface and its dynamics. As a non-linear equation appears in the model, e.g., a viscoelastic phase is considered, the BEM can still be used, but some modifications are needed [50]; more usually, methods based on volume-discretization, such as finite difference method (FDM) and finite element method (FEM) are employed. For problems involving one viscoelastic phase, the FDM is largely used [1, 87, 14, 62, 75], but, when both the suspended and the matrix phase are viscoelastic, i.e., the problem is fully non-linear, the FEM has shown to be the most accurate [51]. When a volume-discretization method is used, a technique for tracking the interface has to be coupled: popular approaches are front tracking [1, 75], volume of fluid [87, 97, 14, 62], and immersed boundary [3].

Since our objective is the simulation of a wide range of deformable sys-

tems, such as Newtonian and non-Newtonian drops, and elastic particles, in flowing simple and complex suspending media, we choose to base our code on the finite element method, that can ensure us great accuracy in the description of the phenomena of our interest. For the interface tracking, we propose an approach based on the FEM too, as it is explained in detail in Section 2.2.3 .

Chapter 2

The method

2.1 Introduction

In this chapter, an arbitrary Lagrangian Eulerian finite element method based code for viscoelastic fluids using well-known stabilization techniques such as SUPG [12], DEVSS [45, 9], and log-conformation [32, 53] is adapted and extended to study the behavior of soft systems suspended in Newtonian and viscoelastic fluids in 3D. The code is validated by comparison with literature results for Newtonian and viscoelastic drops, and elastic particles, suspended in a Newtonian fluid under unbounded shear flow.

2.2 Mathematical model

2.2.1 A liquid drop in a fluid under shear flow

In Figure 2.1, a schematic drawing is reported of an initially spherical liquid drop suspended in a fluid under simple shear flow. For both the suspended and the suspending phase it is assumed that inertia can be neglected and that the volume is constant (incompressible). Therefore, the mass and momentum balance for both the drop and the suspending phase reduce to

$$\boldsymbol{\nabla} \cdot \boldsymbol{u} = 0 \tag{2.1}$$

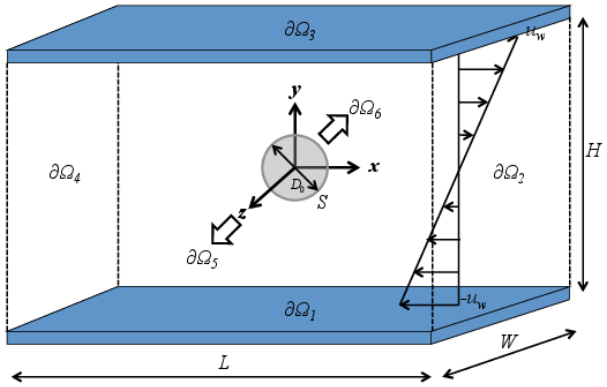

Figure 2.1: Geometry of a spherical drop/elastic particle suspended in a fluid under shear flow.

$$\boldsymbol{\nabla} \cdot \boldsymbol{\sigma} = \mathbf{0} \tag{2.2}$$

where $\boldsymbol{u}$ and $\boldsymbol{\sigma}$ are the velocity vector and the stress tensor, respectively. $\boldsymbol{\sigma}$ can in turn be expressed as

$$\boldsymbol{\sigma} = -p\boldsymbol{I} + \boldsymbol{T} \tag{2.3}$$

where p is the pressure, $\boldsymbol{I}$ is the identity tensor and $\boldsymbol{T}$ is the extra stress tensor.

A material model is specified by a constitutive equation for the extra-stress tensor $\boldsymbol{T}$. For a Newtonian matrix fluid we have

$$\boldsymbol{T} = 2\eta_{\mathrm{m}}\boldsymbol{D} \tag{2.4}$$

with η_{m} the viscosity and $\boldsymbol{D}$ the symmetric part of the velocity gradient tensor ($\boldsymbol{D} = \frac{1}{2}(\nabla\boldsymbol{u} + \nabla\boldsymbol{u}^{\mathrm{T}})$). For a Newtonian fluid inside the drop we have the same constitutive equation, however η_{m} is replaced by the viscosity of the drop η_{d}. The viscosity ratio is defined as $\lambda = \eta_{\mathrm{d}}/\eta_{\mathrm{m}}$.

For a viscoelastic matrix fluid we write

$$\boldsymbol{T} = 2\mu_{\mathrm{m}}\boldsymbol{D} + \boldsymbol{\tau} \tag{2.5}$$

with μ_{m} the solvent viscosity and $\boldsymbol{\tau}$ the viscoelastic contribution to the extra-stress. For $\boldsymbol{\tau}$ we adopt the Giesekus (Gsk) model, which is given by

$$\boldsymbol{\tau} = G_{\mathrm{m}}(\boldsymbol{c} - \boldsymbol{I}) \tag{2.6}$$

$$\lambda_{\mathrm{m}}\overset{\triangledown}{\boldsymbol{c}} + \boldsymbol{c} - \boldsymbol{I} + \alpha_{\mathrm{m}}(\boldsymbol{c} - \boldsymbol{I})^2 = \boldsymbol{0} \tag{2.7}$$

with $\boldsymbol{c}$ the conformation tensor, G_{m} the modulus, λ_{m} the relaxation time and α_{m} the mobility parameter. The upper-convected derivative is defined by

$$\overset{\triangledown}{\boldsymbol{c}} = \dot{\boldsymbol{c}} - (\nabla \boldsymbol{u})^T \cdot \boldsymbol{c} - \boldsymbol{c} \cdot \nabla \boldsymbol{u} \tag{2.8}$$

The mobility parameter α_{m} modulates the shear thinning. For $\alpha_{\mathrm{m}} = 0$ the Gsk model reduces to the Oldroyd-B model, which has a constant viscosity of

$$\eta_{\mathrm{m}} = \mu_{\mathrm{m}} + G_{\mathrm{m}}\lambda_{\mathrm{m}} \tag{2.9}$$

For the Gsk model the viscosity becomes equal to η_{m} in the limit of zero shear rate (zero-shear-rate viscosity). If the solvent viscosity vanishes ($\mu_{\mathrm{m}} = 0$), the model is called the Upper Convected Maxwell (UCM) model. If the drop fluid is viscoelastic, we use the same equations, however we replace the constants with μ_{d}, G_{d}, λ_{d}, α_{d} and η_{d}. The viscosity ratio is again defined as $\lambda = \eta_{\mathrm{d}}/\eta_{\mathrm{m}}$, where the viscosities η_{d} and η_{m} are defined as above for both Newtonian and viscoelastic fluids.

The log-conformation representation (LCR) [53] is a transformation of the original equation for the conformation tensor $\boldsymbol{c}$, as given by Eq. (2.7), to an equivalent equation for $\boldsymbol{s} = \log \boldsymbol{c}$ (and thus $\boldsymbol{c} = \exp(\boldsymbol{s})$):

$$\dot{\boldsymbol{s}} + \boldsymbol{h}(\nabla \boldsymbol{u}, \boldsymbol{s}) = \boldsymbol{0} \tag{2.10}$$

We refer to [53] for details on the expression for $\boldsymbol{h}(\nabla \boldsymbol{u}, \boldsymbol{s})$. Solving the equation for $\boldsymbol{s}$ instead of the equation for $\boldsymbol{c}$ leads to major stability improvements.

The balance equations that model the system shown in Figure 2.1 are solved with the following boundary conditions:

$$\boldsymbol{u} = (-u_{\mathrm{w}}, 0, 0) \text{ on } \partial\Omega_1 \tag{2.11}$$

$$\boldsymbol{u} = (u_{\mathrm{w}}, 0, 0) \text{ on } \partial\Omega_3 \tag{2.12}$$

$$\boldsymbol{u}|_{\partial\Omega_2} = \boldsymbol{u}|_{\partial\Omega_4} \tag{2.13}$$

$$\boldsymbol{t}|_{\partial\Omega_2} = -\boldsymbol{t}|_{\partial\Omega_4} \tag{2.14}$$

$$\boldsymbol{u}|_{\partial\Omega_5} = \boldsymbol{u}|_{\partial\Omega_6} \tag{2.15}$$

$$\boldsymbol{t}|_{\partial\Omega_5} = -\boldsymbol{t}|_{\partial\Omega_6} \tag{2.16}$$

Equations (2.11) and (2.12) are the adherence conditions on the matrix velocity on the lower and the upper walls of the flow cell, respectively; Equations (2.13) and (2.14) express the periodicity of velocity and stress in the matrix along the flow direction, where the traction $\boldsymbol{t}$ is defined as: $\boldsymbol{t} = \boldsymbol{\sigma} \cdot \boldsymbol{m}$, with $\boldsymbol{m}$ the outwardly directed unit vector normal to the boundary; finally, Equations (2.15) and (2.16) are the periodical conditions on velocity and stress in the matrix along the vorticity direction.

The boundary conditions on the drop - matrix interface S are

$$(\boldsymbol{u}_{\mathrm{m}} \cdot \boldsymbol{n})|_S = (\boldsymbol{u}_{\mathrm{d}} \cdot \boldsymbol{n})|_S \tag{2.17}$$

$$\begin{aligned}(\boldsymbol{I} - \boldsymbol{nn}) \cdot (\boldsymbol{u}_{\mathrm{m}} - \boldsymbol{u}_{\mathrm{d}})|_S = \\ -\alpha(\boldsymbol{I} - \boldsymbol{nn}) \cdot (\boldsymbol{\sigma}_{\mathrm{m}} \cdot \boldsymbol{n})|_S\end{aligned} \tag{2.18}$$

and

$$(\boldsymbol{\sigma}_{\mathrm{m}} - \boldsymbol{\sigma}_{\mathrm{d}})|_S \cdot \boldsymbol{n} = \Gamma \boldsymbol{n} \boldsymbol{\nabla} \cdot \boldsymbol{n} \tag{2.19}$$

where $\boldsymbol{n}$ is the outwardly directed unit vector normal to the drop-matrix interface, and Γ is the interfacial tension between the suspended and the suspending liquids. Equations (2.17)-(2.18) express a slip condition on the drop surface, with α the slip coefficient. More specifically, Equation (2.17) imposes the equality of the normal components of the fluid and drop velocities on the drop surface, whereas Equation (2.18) is the Navier-slip condition (acting on

the tangential components of the velocities). Notice that the minus sign on the right-hand side of Equation (2.18) is related to the use of the unit normal vector $\boldsymbol{n}$ in the traction. It is readily observed that the no-slip condition is recovered by setting $\alpha = 0$. Equation (2.19) expresses the discontinuity of traction across the drop-matrix interface due to the presence of surface tension Γ. Finally, since both the continuous and the suspended phase are inertialess, whereas an initial condition is needed on the conformation tensor, if one of the two phases or both are considered to be viscoelastic. If this is the case, we assume that the phase is initially stress-free, which means

$$\boldsymbol{c}|_{t=0} = \boldsymbol{I} \tag{2.20}$$

It is worth remarking that the conformation tensor is defined only in a viscoelastic phase. A pressure level has to be specified in an arbitrary point of the domain.

The equations presented in this section can be made dimensionless by using the initial drop radius $R_0 = D_0/2$ as the characteristic length, the inverse of the imposed shear rate $1/\dot{\gamma}$ (H being the dimension of the channel in the velocity gradient direction) as the characteristic time, and $\eta_\mathrm{m}\dot{\gamma}$ as the characteristic stress. By proceeding in this way, the capillary number $Ca = \eta_\mathrm{m}\dot{\gamma}R_0/\Gamma$, which is the ratio between the viscous shear forces and the interfacial forces to which the drop is subjected, arises from Equation (2.19). In case viscoelastic phases are considered, for each viscoelastic fluid another dimensionless parameter appears, which expresses the ratio between the complex fluid and the interfacial relaxation times [46]. For the matrix, such parameter is $p = \frac{\Psi_{1,\mathrm{m}}\Gamma}{2R_0\eta_\mathrm{m}^2}$, whereas for the drop it reads $p_\mathrm{d} = \frac{\Psi_{1,\mathrm{d}}\Gamma}{2R_0\eta_\mathrm{d}^2}$, with Ψ_1 the first normal stress difference coefficient . Finally, if slip acts on the drop-matrix interface, the slip parameter is made dimensionless through R_0/η_m.

2.2.2 An elastic particle in a fluid under shear flow

It is quite common to use a displacement based formulation for solids. However, our aim is to maintain a conforming mesh across the interface and a mesh updating scheme (ALE) that filters out the tank treading motion to avoid big mesh distortion within a short time. Therefore, we apply here the velocity based approach for an elastic solid as proposed in [35]. This approach is basically the same as considering the droplet as a viscoelastic fluid with infinite relaxation time $\lambda_\mathrm{d} \to \infty$. In that case, Eq. (2.7) (with λ_m replaced by λ_d) becomes

$$\overset{\triangledown}{\boldsymbol{c}} = \boldsymbol{0} \tag{2.21}$$

Together with the initial condition Eq. (2.20), this shows that the solution for $\boldsymbol{c}$ is the Finger tensor $\boldsymbol{B}$. The stress expression Eq. (2.6) now gives

$$\boldsymbol{\tau} = G_\mathrm{d}(\boldsymbol{B} - \boldsymbol{I}) \tag{2.22}$$

which is the neo-Hookean elastic model with a modulus G_d, assuming $\mu_\mathrm{d} = 0$. Taking $\mu_\mathrm{d} \neq 0$ leads to a Kelvin-Voigt viscoelastic solid.

All other equations (mass balance, momentum balance) and the boundary conditions remain the same, assuming a no-slip boundary condition on the particle/matrix interface (i.e., $\alpha = 0$ in Equation (2.18)). Since interfacial tension does not play a role here, we set $\Gamma = 0$ in Eq. (2.19):

$$(\boldsymbol{\sigma} \cdot \boldsymbol{n})|_\mathrm{m} - (\boldsymbol{\sigma} \cdot \boldsymbol{n})|_\mathrm{d} = \boldsymbol{0} \tag{2.23}$$

The equations for a solid particle in a fluid matrix are made dimensionless by using the initial particle radius $R_0 = D_0/2$ as the characteristic length, the inverse of the imposed shear rate $1/\dot{\gamma}$ as the characteristic time, $\eta_\mathrm{m}\dot{\gamma}$ as the characteristic stress in the matrix, and the shear modulus of the elastic material G_d as the characteristic stress in the particle. In analogy with the case where the suspended object is a drop, the elastic capillary number defined as $Ca_\mathrm{e} = \eta_\mathrm{m}\dot{\gamma}/G_\mathrm{d}$, which is the ratio between the viscous forces and the elastic forces to which the particle is subjected, arises from Equation (2.23). In case a viscoelastic matrix is considered, the number $p = \frac{\Psi_{1,\mathrm{m}}G}{2\eta_\mathrm{m}^2}$

arises, that relates the complex fluid constitutive relaxation time and the particle elastic relaxation time. All the quantities that appear in the following sections are dimensionless. For the sake of clarity, no superscripts are used to denote them.

2.2.3 Interface tracking

It is well known from literature that all kinds of deformable objects (ranging from drops to elastic particles to vesicles and capsules) undergo circulation motions when they get deformed [90, 40, 4]. That can easily lead to computational difficulties, since rotation of the interface between the two phases would soon significantly deform the mesh and make simulations break down. Thus a preliminary problem to be solved is that of finding a proper way of updating the interface between the internal and the external phases. Other authors overcome this issue by frequent remeshing [18]. We adopt, instead, the approach proposed by Yon and Pozrikidis [102], i.e. the mesh nodes on the solid-fluid interface move with the velocity normal to the interface. This allows the problems in this thesis to be solved without any remeshing at all.

An interface can be described explicitly by a moving curvilinear coordinate system given by

$$\boldsymbol{x} = \bar{\boldsymbol{x}}(\underset{\sim}{\xi}, t) \tag{2.24}$$

where $\underset{\sim}{\xi} = (\xi^1, \xi^2)$ are the curvilinear coordinates and $\bar{\boldsymbol{x}}$ is the function that maps the coordinates $\underset{\sim}{\xi}$ onto the spatial coordinates $\boldsymbol{x}$. Note, that the mapping is a function of time (moving coordinates). We will call $\underset{\sim}{\xi}$ the grid coordinates, or simply the grid.

The velocity of the grid is given by

$$\dot{\boldsymbol{x}} = \frac{\partial \bar{\boldsymbol{x}}}{\partial t}\Big|_{\underset{\sim}{\xi} \text{ is constant}} \tag{2.25}$$

Only material interfaces are considered here, thus the velocity of the interface $\dot{\boldsymbol{x}}$ must be such that

$$\dot{\boldsymbol{x}} \cdot \boldsymbol{n} = \boldsymbol{u} \cdot \boldsymbol{n} \tag{2.26}$$

where $\boldsymbol{u}$ is the material velocity at the interface and $\boldsymbol{n}$ is the normal vector of the surface. Note, that $\dot{\boldsymbol{x}}$ is equal the velocity of the material in the normal direction only. In the tangential direction the grid can move arbitrarily.

In this work we employ the following equation for the motion of the interface grid [102]:

$$\dot{\boldsymbol{x}} = ((\boldsymbol{u} - \boldsymbol{U}) \cdot \boldsymbol{n})\boldsymbol{n} + \boldsymbol{U} = (\boldsymbol{u} \cdot \boldsymbol{n})\boldsymbol{n} + \boldsymbol{U} \cdot (\boldsymbol{I} - \boldsymbol{n}\boldsymbol{n}) \tag{2.27}$$

where $\boldsymbol{U}$ is the velocity of the center of volume of the droplet. The main purpose for introducing $\boldsymbol{U}$ is to make the motion of the coordinates $\boldsymbol{x}$ on the interface Galilean frame independent. This motion is determined by solving

$$\dot{\boldsymbol{x}} = (\boldsymbol{u} \cdot \boldsymbol{n})\boldsymbol{n} \tag{2.28}$$

in a frame relative to the motion of the center of volume. The additional term with $\boldsymbol{U}$ is only due to the relative motion of the frames, creating an additional tangential motion of the interface grid proportional to $\boldsymbol{U}$.

Although Eq. (2.27) removes the tank-treading motion of the droplet from the motion of the interface, there is another problem in practise. The interface (grid) is discretized by a finite element mesh and elements become unequally distributed. In order to prevent that, we add an additional tangential velocity to Eq. (2.27):

$$\dot{\boldsymbol{x}} = ((\boldsymbol{u} - \boldsymbol{U}) \cdot \boldsymbol{n})\boldsymbol{n} + \boldsymbol{U} + \boldsymbol{u}_\mathrm{t} \tag{2.29}$$

where $\boldsymbol{u}_\mathrm{t}$ is a vector field tangential to the interface. By requesting $\boldsymbol{u}_\mathrm{t}$ to be tangential to the interface, Eq. (2.26) is still fulfilled and the interface is not modified. We choose $\boldsymbol{u}_\mathrm{t}$ to be proportional to the surface gradient of a scalar field c defined on the interface:

$$\boldsymbol{u}_\mathrm{t} = k\nabla_\mathrm{s} c \tag{2.30}$$

with k a factor and ∇_s the surface gradient. Note, that due to the surface gradient the velocity vector $\boldsymbol{u}_\mathrm{t}$ is indeed tangential to the interface. The scalar field c is given by the Poisson problem

$$-\nabla_\mathrm{s}^2 c = 1 - \frac{1}{g} \tag{2.31}$$

with g the element area function, which has been scaled such that

$$\int_S 1/g \, ds = \text{area of } S \tag{2.32}$$

The tangential interface velocity $\boldsymbol{u}_\mathrm{t}$ tries to make the elements of equal size. Using the flux of a Poisson problem has been inspired by the grid deformation technique [101, 42]. This technique defines an adaptive computational mesh from a uniform base mesh in 2D or 3D, using a monitor function f, specifying the requested size of elements. The computational mesh is found by solving an ODE in a pseudo time interval between 0 and 1. We have adapted this technique for our problem by blending the pseudotime problem with the real time problem of the interface motion. Furthermore $f = 1$ (equally distributed elements), the Laplace operator is now defined on a curved surface and the expression for the grid velocity is simpler, i.e. proportional to the surface gradient by a constant factor.

2.3 Numerical discretization

2.3.1 Volume discretization

Both the matrix fluid and the droplet fluid (or solid particle) domain are discretized using the finite element method employing a mesh of quadratic tetrahedra. The interface mesh aligns with element faces (quadratic triangles), which are the same on the matrix and droplet side (conforming geometry).

In Figure 2.2, the mesh employed in the simulations presented in this thesis is shown. In the box on the right, a zoom of the interface mesh of the initially spherical suspended object is displayed.

We use quadratic (P_2) interpolation for the velocity $\boldsymbol{u}$, linear (P_1) interpolation for the pressure p (Taylor-Hood elements) and linear (P_1) interpolation for both the log-conformation tensor $\boldsymbol{s}$ and the conformation tensor $\boldsymbol{c}$. Since the droplet mesh is decoupled from the matrix mesh, all nodes at the interface are double. The velocities in the interface nodes are coupled by using collocated Lagrange multipliers, leading to a continuous normal velocity field

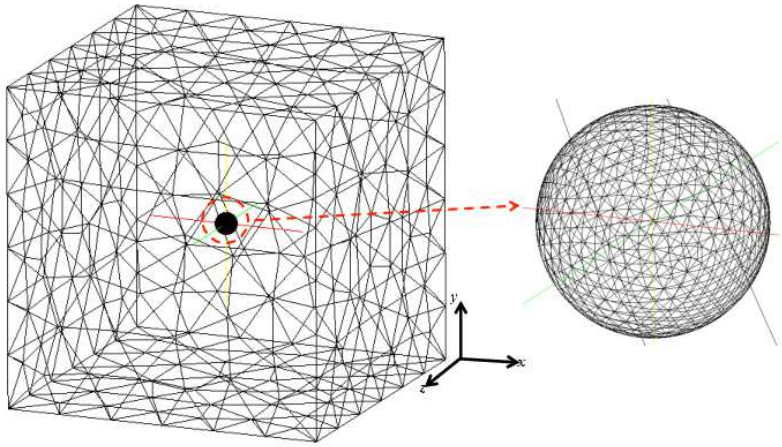

Figure 2.2: Mesh of an initially spherical drop/elastic particle suspended in a shear flow cell. A zoom of the spherical surface of the suspended object is displayed in the box on the right.

across the interface (the tangential velocity is also continuous in the no-slip case, otherwise a discontinuity is allowed on the interface). However, the pressure and conformation fields are allowed to jump across the interface.

We apply an arbitrary Lagrangian Eulerian (ALE) approach, where a motion of the interface mesh generates a velocity field $\boldsymbol{u}_{\mathrm{m}}$ of the domain mesh (see Sec. 2.3.3 on how the mesh velocity $\boldsymbol{u}_{\mathrm{m}}$ is computed). The substantial derivative in Eq. (2.8) (and Eq. (2.10)) is splitted into a mesh derivative and a convective derivative as follows:

$$\dot{\boldsymbol{c}} = \frac{\delta \boldsymbol{c}}{\delta t} + (\boldsymbol{u} - \boldsymbol{u}_{\mathrm{m}}) \cdot \nabla \boldsymbol{c} \tag{2.33}$$

where $\delta \boldsymbol{c}/\delta t$ is the time derivative when keeping the grid coordinates constant. With an actual mesh, the grid coordinates can be interpreted as the reference coordinates when evaluating element quantities.

For the discretization of the momentum balance we use the DEVSS-G technique (see [45, 8]) for stabilizing the velocity-stress interpolation. The

weak form of the momentum balance and the continuity equation becomes:

$$\begin{aligned}\big((\nabla \boldsymbol{v})^T, \theta(\nabla \boldsymbol{u} - \boldsymbol{G}^T) + \boldsymbol{\tau}\big) - (\nabla \cdot \boldsymbol{v}, p) \\ + \int_S (\nabla_{\mathrm{s}} \boldsymbol{v})^T : \Gamma(\boldsymbol{I} - \boldsymbol{nn})\, ds = 0\end{aligned} \tag{2.34}$$

$$(q, \nabla \cdot \boldsymbol{u}) = 0 \tag{2.35}$$

$$(\boldsymbol{H}, -\nabla \boldsymbol{u} + \boldsymbol{G}^T) = 0 \tag{2.36}$$

with $\boldsymbol{v}$, q and $\boldsymbol{H}$ the test functions for the velocity $\boldsymbol{u}$, the pressure p and the projected velocity gradient $\boldsymbol{G}$, respectively. Furthermore, proper inner products $(.,.)$ are defined on the full domain Ω. The additional parameter θ in the DEVSS-G is taken to be $\theta = \eta_{\mathrm{m}}$ and $\theta = \eta_{\mathrm{d}}$ for the matrix and droplet, repectively. If $\lambda_{\mathrm{d}} \to \infty$ (solid particle) we take $\theta = G_{\mathrm{d}}\Delta t$, with Δt the time step (see Sec. 2.3.3).

We apply the method of D'Avino and Hulsen [22] for decoupling the momentum balance from the constitutive equation. For this, we evaluate the weak form at the new time step t_{n+1} and replace the extra-stress $\boldsymbol{\tau}$ in Eq. (2.34), with the time discretized, but space continuous, constitutive equation

$$\begin{aligned}\boldsymbol{\tau}_{n+1} = G\big(\boldsymbol{c}_n - \boldsymbol{I}\big) + G\Delta t\big(- (\boldsymbol{u}_{n+1} - \boldsymbol{u}_{\mathrm{m},n+1}) \cdot \nabla \boldsymbol{c}_n \\ + (\nabla \boldsymbol{u}_{n+1})^T \cdot \boldsymbol{c}_n + \boldsymbol{c}_n \cdot \nabla \boldsymbol{u}_{n+1} + \boldsymbol{c}_n - \boldsymbol{I} + \alpha(\boldsymbol{c}_n - \boldsymbol{I})^2)\big)\end{aligned} \tag{2.37}$$

As a result we obtain a Stokes-like system in the velocity field $\boldsymbol{u}_{n+1}$ and pressure field p_{n+1}, both at the new time step t_{n+1}.

After computing $\boldsymbol{u}_{n+1}$ and p_{n+1}, the log-conformation field $\boldsymbol{s}_{n+1}$ is obtained by the weak form of Eq. (2.10) combined with SUPG and first and second-order schemes based on backwards differencing (Gear) for time discretization:

first order

$$\hat{\boldsymbol{s}}_{n+1} = \boldsymbol{s}_n \tag{2.38}$$

$$\big(\boldsymbol{w}+\tau(\boldsymbol{u}_{n+1}-\boldsymbol{u}_{\mathrm{m},n+1})\cdot\nabla\boldsymbol{w}, \frac{\boldsymbol{s}_{n+1}-\boldsymbol{s}_n}{\Delta t} + (\boldsymbol{u}_{n+1}-\boldsymbol{u}_{\mathrm{m},n+1})\cdot\nabla\boldsymbol{s}_{n+1} + \boldsymbol{h}(\nabla\boldsymbol{u}_{n+1}, \hat{\boldsymbol{s}}_{n+1})\big) = 0 \tag{2.39}$$

second order

$$\hat{\boldsymbol{s}}_{n+1} = 2\boldsymbol{s}_n - \boldsymbol{s}_{n-1} \tag{2.40}$$

$$\big(\boldsymbol{w}+\tau(\boldsymbol{u}_{n+1}-\boldsymbol{u}_{\mathrm{m},n+1})\cdot\nabla\boldsymbol{w}, \frac{\frac{3}{2}\boldsymbol{s}_{n+1}-2\boldsymbol{s}_n+\frac{1}{2}\boldsymbol{s}_{n-1}}{\Delta t} + (\boldsymbol{u}_{n+1}-\boldsymbol{u}_{\mathrm{m},n+1})\cdot\nabla\boldsymbol{s}_{n+1} + \boldsymbol{h}(\nabla\boldsymbol{u}_{n+1}, \hat{\boldsymbol{s}}_{n+1})\big) = 0 \tag{2.41}$$

with $\boldsymbol{w}$ a test function of $\boldsymbol{s}$ and τ the SUPG parameter, for which we take

$$\tau = \frac{h}{2U}$$

where h is a characteristic element length and U the length of the velocity vector $\boldsymbol{u}$, evaluated in each integration point separately.

Finally the conformation tensor $\boldsymbol{c}_{n+1}$ is obtained by projection:

$$\big(\boldsymbol{e}, \boldsymbol{c}_{n+1} - \exp(\boldsymbol{s}_{n+1})\big) \tag{2.42}$$

with $\boldsymbol{e}$ a test function of $\boldsymbol{c}$.

2.3.2 Interface discretization

We will discretize the fluid velocity inside the droplet and matrix volumes using isoparametric quadratic shape functions on tetrahedrons. Therefore, the interface (grid) will be discretized using isoparametric quadratic triangular elements that conform to the volumetric mesh, i.e.,

$$\boldsymbol{x} = \sum_i \boldsymbol{x}_i \phi_i \tag{2.43}$$

where ϕ_i are the quadratic shape functions on the surface mesh. A possibility to proceed is discretize Eq. (2.29) using a Galerkin finite element method combined with a sufficiently stable high-order explicit time discretization scheme. Although this seems to work, it requires rather small time steps and is not very robust. Therefore, we use pursue a different approach.

In order to stabilize the discretization of Eq. (2.29) we rewrite this equation as follows:

$$\dot{\boldsymbol{x}} + (\boldsymbol{u} - \boldsymbol{U}) \cdot (\boldsymbol{I} - \boldsymbol{n}\boldsymbol{n}) = \boldsymbol{u} + \boldsymbol{u}_{\mathrm{t}} \tag{2.44}$$

Substituting the expression for the surface identity tensor $\boldsymbol{I} - \boldsymbol{n}\boldsymbol{n} = \boldsymbol{g}^i \boldsymbol{g}_i$, where $\boldsymbol{g}_i = \partial \boldsymbol{x}/\partial \xi^i$, $i = 1, 2$ are the (covariant) base vectors and $\boldsymbol{g}^i$, $i = 1, 2$ the dual base vectors, we get

$$\dot{\boldsymbol{x}} + (\boldsymbol{u} - \boldsymbol{U}) \cdot \boldsymbol{g}^i \frac{\partial \boldsymbol{x}}{\partial \xi^i} = \boldsymbol{u} + \boldsymbol{u}_{\mathrm{t}} \tag{2.45}$$

or, with the surface gradient operator $\nabla_{\mathrm{s}} = \boldsymbol{g}_i \dfrac{\partial}{\partial \xi^i}$,

$$\dot{\boldsymbol{x}} + (\boldsymbol{u} - \boldsymbol{U}) \cdot \nabla_{\mathrm{s}} \boldsymbol{x} = \boldsymbol{u} + \boldsymbol{u}_{\mathrm{t}} \tag{2.46}$$

This is a non-linear unsteady convection equation on the surface for the position $\boldsymbol{x}$ of the surface and resembles a multi-dimensional height-function equation (see [59, 15] and the references therein for details on the height-function equation).

Similarly to the height function equation we apply SUPG to stabilize the convection and use implicit time integration. A complication here is that the surface gradient operator ∇_{s} depends on the position of the surface $\boldsymbol{x}$. Therefore, we use a prediction of $\boldsymbol{x}$ for determining ∇_{s}. The first and second-order schemes based on backwards differencing (Gear) now become:

first order

$$\hat{\boldsymbol{x}}_{n+1} = \boldsymbol{x}_n \tag{2.47}$$

$$\left(\boldsymbol{w} + \tau (\boldsymbol{u} - \boldsymbol{U}) \cdot \hat{\nabla}_{\mathrm{s}} \boldsymbol{w}, \frac{\boldsymbol{x}_{n+1} - \boldsymbol{x}_n}{\Delta t} + (\boldsymbol{u} - \boldsymbol{U}) \cdot \hat{\nabla}_{\mathrm{s}} \boldsymbol{x}_{n+1} - \boldsymbol{u} - \boldsymbol{u}_{\mathrm{t}} \right) = 0 \tag{2.48}$$

second order

$$\hat{\boldsymbol{x}}_{n+1} = 2\boldsymbol{x}_n - \boldsymbol{x}_{n-1} \tag{2.49}$$

$$\Big(\boldsymbol{w}+\tau(\boldsymbol{u}-\boldsymbol{U})\cdot\hat{\nabla}_{\mathrm{s}}\boldsymbol{w},\, \frac{\frac{3}{2}\boldsymbol{x}_{n+1} - 2\boldsymbol{x}_n + \frac{1}{2}\boldsymbol{x}_{n-1}}{\Delta t} + (\boldsymbol{u}-\boldsymbol{U})\cdot\hat{\nabla}_{\mathrm{s}}\boldsymbol{x}_{n+1} - \boldsymbol{u} - \boldsymbol{u}_{\mathrm{t}}\Big) = 0 \tag{2.50}$$

where $(.,.)$ is a proper L^2 inner product defined on the interface S, $\boldsymbol{w}$ is the test function of $\boldsymbol{x}$, τ is the SUPG parameter, $\hat{\nabla}_{\mathrm{s}}$ is evaluated using $\hat{\boldsymbol{x}}_{n+1}$ and $\boldsymbol{u}$, $\boldsymbol{U}$, $\boldsymbol{u}_{\mathrm{t}}$ need to be evaluated at time t_{n+1}.

Remarks:

1. $\boldsymbol{U}$ is computed from the position of the center of volume of the droplet, denoted by $\boldsymbol{X}$:

   first order

   $$\boldsymbol{U} = \frac{\boldsymbol{X}_{n+1} - \boldsymbol{X}_n}{\Delta t} \tag{2.51}$$

   second order

   $$\boldsymbol{U} = \frac{\frac{3}{2}\boldsymbol{X}_{n+1} - 2\boldsymbol{X}_n + \frac{1}{2}\boldsymbol{X}_{n-1}}{\Delta t} \tag{2.52}$$

   The center of volume $\boldsymbol{X}$ is computed from the predicted position of the interface $\hat{\boldsymbol{x}}_{n+1}$ using the volume V and the linear moment of volume $\boldsymbol{Q}$:

   $$V = \int_V 1\, dx = \frac{1}{3}\int_V \nabla\cdot\boldsymbol{x}\, dx = \frac{1}{3}\int_S \boldsymbol{n}\cdot\boldsymbol{x}\, ds \tag{2.53}$$

   $$\boldsymbol{Q} = \int_V \boldsymbol{x}\, dx = \frac{1}{2}\int_V \nabla|\boldsymbol{x}|^2\, dx = \frac{1}{2}\int_S \boldsymbol{n}|\boldsymbol{x}|^2\, ds \tag{2.54}$$

   where $\boldsymbol{x} = \hat{\boldsymbol{x}}_{n+1}$ and $\boldsymbol{n}$ is the outwardly directed unit normal on the interface S. The center of volume of the drop is computed from $\boldsymbol{X} = \boldsymbol{Q}/V$.

2. For the SUPG parameter we take

$$\tau = \frac{\beta h}{2U_{\mathrm{t}}}$$

where h is a characteristic element length, β is a scalar between 0 and 1 and $U_{\mathrm{t}} = |(\boldsymbol{u} - \boldsymbol{U}) \cdot (\boldsymbol{I} - \boldsymbol{nn})|$, the length of the tangential velocity. Note, that U_{t} is evaluated in each integration point separately. We use $h = \sqrt{A_{\mathrm{e}}}$, with A_{e} the area of an element, and adjust β to get the best results. In practise we use $\beta = 1.0$ for linear elements and $\beta = 0.5$ for quadratic elements.

3. The time-discretization is semi-implicit and based on the Gear schemes. The second-order scheme is a two-step scheme which needs to be started by the first-order scheme in the first time step.

2.3.3 Time stepping scheme

The full time stepping scheme for both the interface and the fluids and/or solid is as follows. The considered time interval is divided into discrete intervals using a timestep Δt. The discrete times therefore become $t_i = i\Delta t$, $i = 0, \ldots$. A single time step from t_n to t_{n+1} is subdivided a number of substeps:

Step 1 Predict the position of the new interface $\hat{\boldsymbol{x}}_{n+1}$ using Eq. (2.49).

Step 2 The mesh is translated in x-direction such that the x-component of center of volume $\boldsymbol{X}$ does not move relative to the mesh outer boundaries. The displacement vector is given by $\boldsymbol{d}_1 = (X_{x,n+1} - X_{x,n}, 0, 0)$ within a time step.

Step 3 The additional ALE displacement of the mesh $\boldsymbol{d}_2$ within a time step is computed from the Laplace equation

$$\nabla \cdot (k^{\mathrm{e}} \boldsymbol{d}_2) = \boldsymbol{0} \tag{2.55}$$

with $\boldsymbol{d}_2$ set to the (relative) displacement of the interface $\hat{\boldsymbol{x}}_{n+1} - \hat{\boldsymbol{x}}_n - \boldsymbol{d}_1$ as a Dirichlet boundary condition an the interface. On all other boundaries $\boldsymbol{d}_2$ is set to zero. Note, that due to these boundary conditions the nodes of the volume mesh at the interface and the interface mesh coincide at all times. The ALE motion of the mesh according to Eq. (2.55) is a generalization of the ALE technique introduced by Hu *et al.* for rigid particles [52]. In Eq. (2.55) k^{e} is a function that controls the deformation of the domain. As suggested in [52] we take k^{e} constant on an element and equal to the inverse of the volume of the element. In this way the deformation of the mesh is largely performed by the big elements and the small ones around the interface deform less. The mesh coordinates are updated: $\boldsymbol{x}_{\mathrm{m},n+1} = \boldsymbol{x}_{\mathrm{m},n} + \boldsymbol{d}_1 + \boldsymbol{d}_2$ and the mesh velocity at t_{n+1} is computed from

$$\boldsymbol{u}_{\mathrm{m}} = (\tfrac{3}{2}\boldsymbol{x}_{\mathrm{m},n+1} - 2\boldsymbol{x}_{\mathrm{m},n} + \tfrac{1}{2}\boldsymbol{x}_{\mathrm{m},n-1})/\Delta t \tag{2.56}$$

Step 4 The velocity $\boldsymbol{u}_{n+1}$, pressure p_{n+1} and conformation $\boldsymbol{c}_{n+1}$ are computed from Eqs. (2.34)–(2.42).

Step 5 The (corrected) position of the interface $\boldsymbol{x}_{n+1}$ is computed from Eq. (2.50).

This describes the second-order time integration scheme. It must be started in the first time step by the appropriate first-order variants of the equations and $\boldsymbol{u}_{\mathrm{m}} = (\boldsymbol{x}_{\mathrm{m},n+1} - \boldsymbol{x}_{\mathrm{m},n})/\Delta t$ instead of Eq. (2.56), which in the first step leads to $\boldsymbol{u}_{\mathrm{m}} = \boldsymbol{0}$.

2.3.4 Computation of D and θ

As reported in Section 2.1, it is known that, when drops and elastic particles are suspended in a Newtonian fluid under shear flow, they attain a shape similar to an ellipsoid, whose semiaxes define the deformation and orientation of the suspended body. The evaluation of the deformation and orientation of the systems considered in this work is just based on such result: in order

to determine their deformation parameter D, and orientation angle θ, the assumption is made that during deformation, the drop/elastic particle has an ellipsoidal shape. Under such assumption, which has to be verified, as explained below, the coordinates of the nodes on the interface between the suspended and the suspending phase can be fitted with an ellipsoid by a least-squares algorithm. The fit returns a set of nine parameters, which are the coefficients of the equation of the ellipsoid for which the sum of the square distances between the analytical surface and the discrete points is the lowest. In Cartesian coordinates, such equation reads:

$$ax^2 + by^2 + cz^2 + dxy + exz + fyx + gx + hy + iz = 1 \tag{2.57}$$

Once the equation of the ellipsoid is known, the Cartesian components of the semiaxes can be determined and, from them, the Taylor deformation parameter and the orientation angle can be computed.

In general, it is always possible to do the above described fit of a set of discrete points, and so to compute the deformation parameter and orientation angle of the fitting analytical ellipsoid. However, this does not ensure that the surface where the points lie is actually ellipsoidal. Therefore, it is necessary to check that. This is done by computing for each interfacial node the relative distance to the closest point of the analytical surface. When the points of the numerical surface are no further than 2–3% with respect to the fitting analytical ellipsoid, we assume that the deformed shape of the system under investigation is actually ellipsoidal.

2.3.5 Computational time

As written in Section 2.1, in this chapter the behavior of drops and elastic particles suspended in a Newtonian fluids under unbounded shear flow is studied as a validation for our code. The simulations are performed on *Dell PowerEdge M600* machines equipped with two quad core *Intel Xeon E5410*@2.33GHz processors. The computational time ranges from a few hours (in the order of four/five) for a Newtonian drop in a Newtonian fluid

to few days (in the order of two/three) for a neo-Hookean elastic particle in a Newtonian fluid.

2.4 Convergence tests

Before running simulations, convergence tests have to be performed in space and time. This also helps in optimizing the mesh resolution and time-step such that the results are sufficiently reliable without wasting too much computational time.

2.4.1 Interface motion

To check the accuracy of our approach for tracking the interface, we consider a fluid subjected to extensional flow with strain rate $\dot{\epsilon}$.

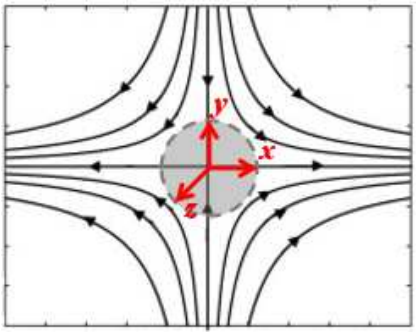

Figure 2.3: Schematic representation of a fluid domain under extensional flow.

If we take a sphere made of fluid points (the shaded area displayed in Figure 2.3) initially centered at the stagnation point of the flow field, the temporal evolution of the points on its surface is analytically known and is given by

$$\begin{aligned} x(t) &= x_0 e^{\dot{\epsilon}t} \\ y(t) &= y_0 e^{-\dot{\epsilon}t/2} \\ z(t) &= z_0 e^{-\dot{\epsilon}t/2} \end{aligned} \tag{2.58}$$

where x_0, y_0, and z_0 are the initial coordinates of each point on the sphere. We numerically solve the position of the surface using the scheme described

in Sec. 2.3.2, with an initially spherical quadratic triangular mesh and taking $\boldsymbol{u} = (\dot{\epsilon}x, -\dot{\epsilon}y/2, -\dot{\epsilon}z/2)$. Then, we compare the numerical and analytical results after 0.5 strain units, which means $\dot{\epsilon}t = 0.5$, by computing the maximum error

$$E_{\max} = \max_{i=1,\ldots,N_{\text{nod}}} |\boldsymbol{x}_{i,\text{num}} - \boldsymbol{x}_{i,\text{an}}|$$

and the (nodal) L^2 error

$$E_2 = \Big[\frac{1}{N_{\text{nod}}} \sum_{i=1}^{N_{\text{nod}}} (|\boldsymbol{x}_{i,\text{num}} - \boldsymbol{x}_{i,\text{an}}|^2)\Big]^{\frac{1}{2}}$$

where N_{nod} is the number of mesh nodes, $\boldsymbol{x}_{i,\text{num}}$ is the position of the i-th node of the mesh computed numerically, whereas $\boldsymbol{x}_{i,\text{an}}$ is the intersection of the line through $\boldsymbol{x}_{i,\text{num}}$ and the origin with the ellipsoid that analytically describes the temporal evolution of the fluid points. The error will be presented relative to the radius of the original sphere.

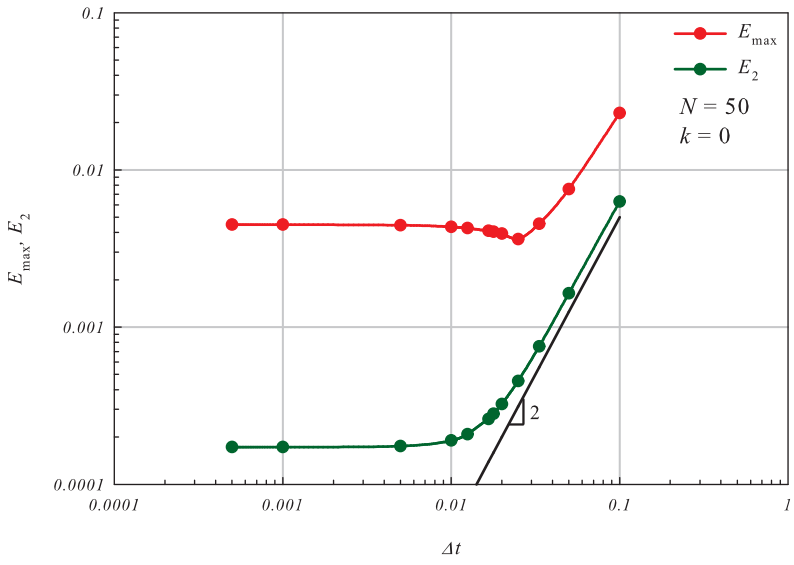

Figure 2.4: $E_{\max}$ (red curve) and E_2 (green curve) *vs.* Δt for $N = 50$, $k = 0$. The straight line shows that the error behaves as $\mathcal{O}(\Delta t^2)$ for large Δt. For small Δt, the error is dominated by the spatial error.

In Figure 2.4, the error for a fixed mesh (number of elements on the equator of the sphere $N = 50$) and motion of the interface nodes only in the normal direction (i.e., $\boldsymbol{u}_{\mathrm{t}} = \mathbf{0}$ or $k = 0$) is shown *vs.* the dimensionless time step Δt (the characteristic time for non-dimensionalization being $1/\dot{\epsilon}$). As expected, for large time steps the error is dominated by time errors, and it varies according to $\mathcal{O}(\Delta t^2)$, since we use a second-order time discretization. For small Δt, the error is dominated by spatial errors. The transition from spatial to time errors is around $\Delta t = 10^{-2}$ for this problem. The large difference between $E_{\max}$ and E_2 is because in this problem the error is mainly located at the tips of the ellipsoid due to the higher curvature there.

Now we fix the time step to $\Delta t = 10^{-3}$, to be sure the time errors are negligible, and then vary the mesh. In Figure 2.5, the errors are shown for varying N from 10 until 200. It is clear that the spatial errors decrease as N^{-3}, or as h^3, with h the size of the elements in the interface mesh. This confirms that the spatial convergence is optimal using quadratic elements.

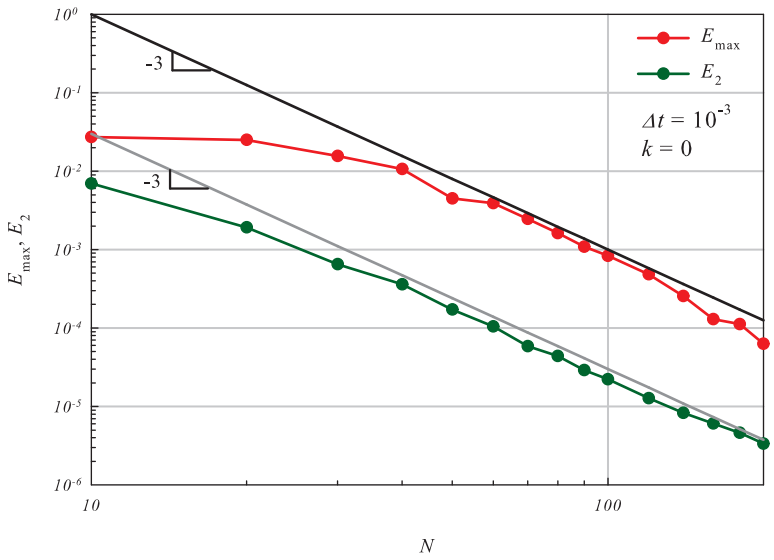

Figure 2.5: $E_{\max}$ (red curve) and E_2 (green curve) *vs.* N for $\Delta t = 10^{-3}$, $k = 0$. The straight line shows that the error behaves as $\mathcal{O}(N^{-3})$ for large N (small element size).

Finally we include an additional tangential motion to make the mesh

more uniform during deformation, $\boldsymbol{u}_\mathrm{t} \neq \mathbf{0}$ or $k \neq 0$. Unfortunately, there is no single optimal value for k. Writing $k = k'\dot{\epsilon}$, it turns out that the optimal value of k' for this problem depends on N and therefore on the element size. For example, for $N = 30$, 50 and 70, we find optimal values ranges for k' to be $k' = 15$–20, 10–15 and 5–7, respectively, i.e. optimal k' decreases for smaller element sizes. Including tangential motion can decrease the error significantly, especially for E_max. In Figure 2.6, we show the error *vs.* Δt (for $N = 50$) again, but now for both $k = 0$ and $k = 10\dot{\epsilon}$. We see, that E_max has been reduced by an order of magnitude, but also E_2 has been reduced by a factor of more than two.

In conclusion, we can say that the proposed scheme has optimal error rates in time and space, and choosing the tangential movement (factor k) wisely can reduce the error significantly.

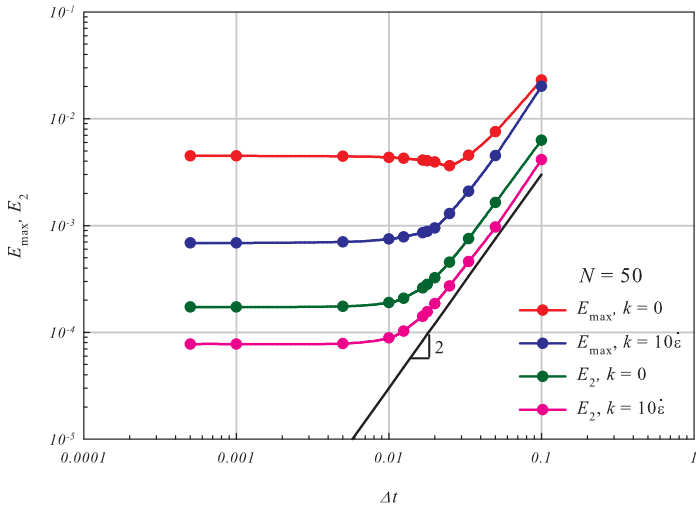

Figure 2.6: E_max (red and blue curve) and E_2 (green and pink curve) *vs.* Δt for $k = 0$ and $k = 10\dot{\epsilon}$, respectively. Mesh is fixed ($N = 50$). The straight line shows that the error behaves as $\mathcal{O}(\Delta t^2)$ for large Δt. For small Δt, the error is dominated by the spatial error.

2.4.2 Newtonian drop in a Newtonian fluid

As reported in Section 2.2, we consider a single liquid drop or elastic particle suspended in a fluid under unbounded shear flow, which means, with reference to Figure 2.1, $H \gg D_0$. We found $H/D_0 = 15$ to be sufficient to obtain the unbounded shear condition in all our results.

As an example, in this section, the convergence tests for a Newtonian drop suspended in a Newtonian fluid (in the absence of interfacial slip) under unbounded shear flow are presented for $Ca = 0.1$, and $\lambda = 1.0$. The k-factor of Equation (2.30) is set to $10\dot{\gamma}$.

Due to the applied flow, the initially spherical drop deforms until it attains an ellipsoid-like shape with a fixed orientation with respect to the flow direction. Thus the Taylor deformation parameter D, and the orientation angle θ can be chosen as the quantities for evaluating convergence.

In Figure 2.7a, D is reported *vs.* dimensionless time for $\Delta t = 0.001$, and for three values of the number of mesh nodes on the equator of the initial sphere, i.e., 28, 40, and 50. With 40 nodes, the convergence is achieved, and the results do not change anymore if we increase the number to 50, as highlighted in the zoomed box, where it is shown that a small difference exists between the results for 28 and 40 nodes, but there is no difference between the results for 40 and 50 nodes up to four digits (the symbols referring to such values completely overlap). In Figure 2.7b, the orientation angle θ is reported *vs.* time for the same Δt and the same values of the number of nodes on the interface as in Figure 2.7a. Even there, with 40 nodes on the equator, the convergence is achieved up to four digits (as also pointed out in the box). We can, then, conclude that under the given flow conditions, 40 nodes on the equator of the sphere are sufficient for the convergence of the simulation results.

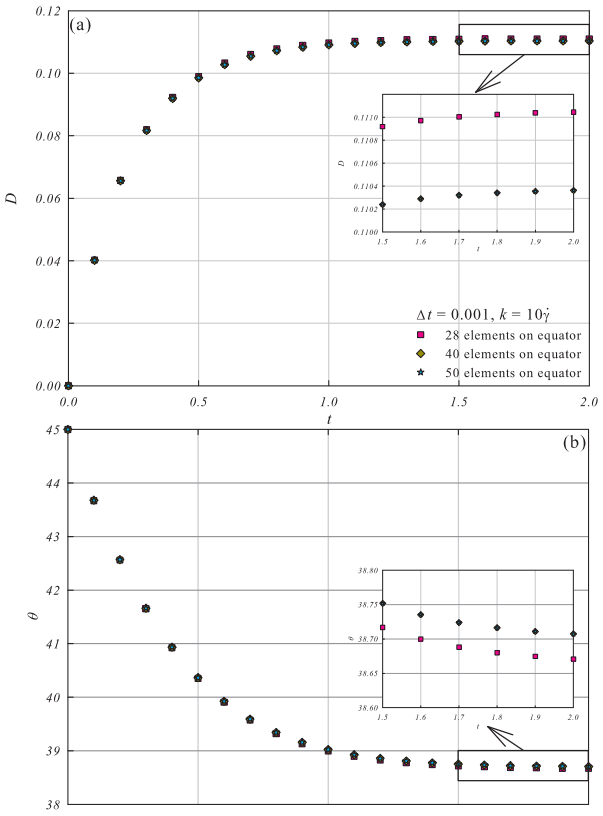

Figure 2.7: Convergence tests for a Newtonian drop in a Newtonian fluid under unbounded shear flow with $Ca = 0.1$ and $\lambda = 1.0$. a) D vs. dimensionless time t for three values of the number of nodes on the drop-matrix interface; b) θ vs. t for the same three values of the number of nodes on the interface. For both panels, $\Delta t = 0.001$, $k = 10\dot{\gamma}$.

In Figure 2.8a, D is shown *vs.* time for 40 nodes on the equator of the initially spherical drop - matrix interface, and for three values of the time-step for numerical integration, i.e., $\Delta t = 0.0075, 0.005, 0.002$; below $\Delta t = 0.005$, the results do not change up to four digits, as it is more clearly shown in the box, where a zoom of the last part of the curves corresponding to the different Δt-values is displayed. The same happens for θ, as it is shown in Figure 2.8b. The fact that below $\Delta t = 0.005$ the results converge in time up to four digits confirms the validity of the preliminary choice of $\Delta t = 0.001$ for the spatial convergence tests reported in Figure 2.7. In the end, we can

conclude that 40 nodes on the equator of the initial sphere, which means 926 nodes on the drop-matrix interface, and $\Delta t = 0.005$ ensure the convergence of the numerical results both in time and space under the given flow conditions.

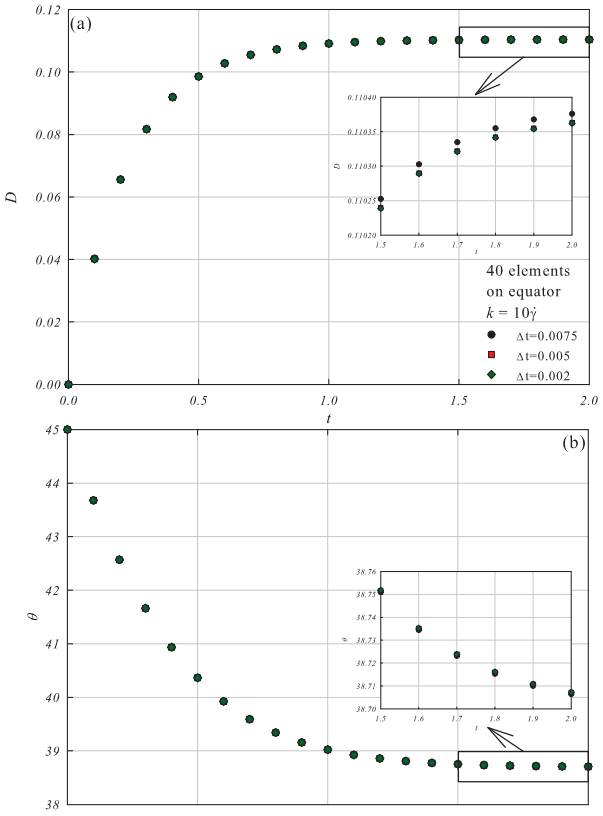

Figure 2.8: Convergence tests for a Newtonian drop in a Newtonian fluid under unbounded shear flow with $Ca = 0.1$ and $\lambda = 1.0$. a) D vs. dimensionless time t for three values of the time-step; b) θ vs. t for the same three values of the time-step. For both panels, the number of nodes on the drop-matrix interface is 926 (40 on the equator), $k = 10\dot{\gamma}$.

It has been verified that such values of the mesh and timestep resolutions are suitable for the simulation of all the systems considered in this thesis, for all the values of the physical parameters investigated.

In Figure 2.9, deviation with respect to an ellipsoid of the deformed drop at the steady state is shown. For each of the 926 nodes on the drop-matrix

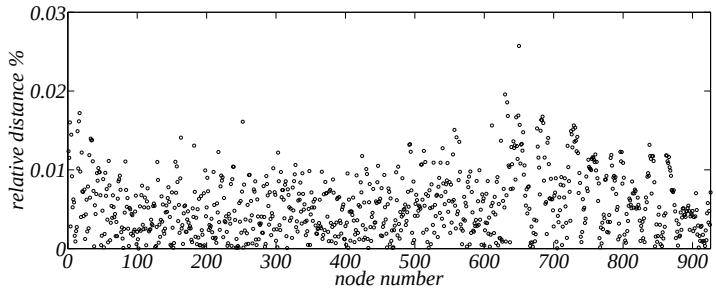

Figure 2.9: Normalized distance between the interface mesh nodes and the fitting ellipsoid at the steady state for a Newtonian drop in a Newtonian fluid under unbounded shear flow with $Ca = 0.1$ and $\lambda = 1.0$. The number of nodes on the drop-matrix interface is 926.

interface, the distance to the analytical fitting ellipsoid, normalized by the distance of the node from the center of volume of the deformed drop is plotted. It can be seen that such distance is always in the order of $2 \cdot 10^{-4}$, which means that the fitting ellipsoid is never further than about 0.02% from the actual interface between the drop and the matrix.

In the following, whenever D- and θ-values are presented, the shape of the system to which they refer has always been verified to be ellipsoidal.

2.5 Validation of the code

2.5.1 Deformation of a Newtonian drop in a Newtonian fluid

The no-slip case

A Newtonian drop is suspended in a Newtonian fluid under unconfined shear flow, in the absence of interfacial slip. As known from Taylor [95], in the moderate capillary number regime, the drop deforms into an ellipsoid and attains a fixed orientation with respect to the direction of the flow.

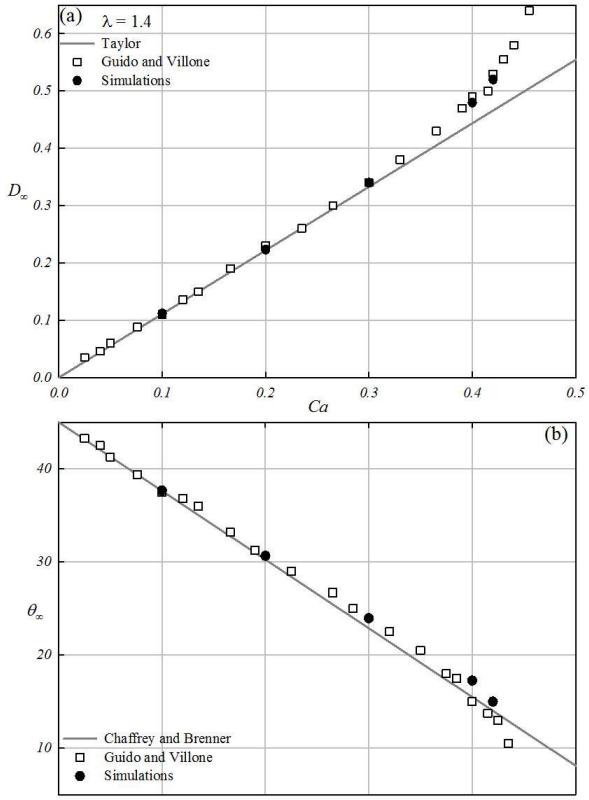

Figure 2.10: Deformation of a Newtonian drop in a Newtonian fluid under unbounded shear flow. a) D_∞ vs. Ca. Gray solid line: predictions from Equation (1.1); white squares: experimental data from [49]; black circles: our numerical simulations; b) θ_∞ vs. Ca. Gray solid line: predictions from Equation (2.59); white squares: experimental data from [49]; black circles: our numerical simulations. For both panels, $\lambda = 1.4$.

In Figure 2.10a, the steady state values of the Taylor deformation parameter D_∞ emerging from our numerical simulations are plotted *vs.* the capillary number Ca as black circles. The viscosity ratio is $\lambda = 1.4$. Such results are compared with the predictions obtained from Equation (1.1) for $\lambda = 1.4$ (the solid gray line), and with experimental data from Guido and Villone [49] for the same viscosity ratio (the white squares). It can be seen that for Ca less than about 0.3, the linear prediction, the experimental, and the numerical data substantially overlap, then the experimental points detach from the pre-

dictions of Equation (1.1), which is confirmed by our numerical results, that show a very satisfactory quantitative agreement with the experiments in the whole range of Ca explored. In Figure 2.10b, the steady orientation angle θ_∞ is plotted *vs.* Ca for the same λ-value as in panel (a). Our numerical results are displayed as black circles and compared with experimental results from [49] (the white squares), and theoretical predictions due to Chaffey and Brenner [13] (the gray solid line), according to which the steady orientation angle of a deformed drop (in radians) is:

$$\theta_\infty = \frac{\pi}{4} - \frac{(19\lambda + 16)(2\lambda + 3)}{80(1 + \lambda)} Ca \tag{2.59}$$

In the whole range of Ca investigated, a very good quantitative agreement among the theory, the experiments and the simulations is found.

The case with slip

A Newtonian drop is suspended in a Newtonian fluid under unconfined shear flow, in the presence of interfacial slip. In analogy to what is shown in the no-slip case, the drop deforms into an ellipsoid and attains a fixed orientation with respect to the direction of the flow. The steady deformation and orientation angle are affected by the extent of the slip.

In Figure 2.11, the steady values of the Taylor deformation parameter D_∞ emerging from our numerical simulations are plotted *vs.* the capillary number Ca, for three values of the slip parameter α ($\alpha = 0$ (no-slip), 0.1, 1.0), as circles. The viscosity ratio is $\lambda = 1.0$. Such findings are compared with the perturbative predictions given by Ramachandran and Leal in [85], displayed on the graph as solid lines of the same color as the corresponding data set. It can be seen that, at fixed Ca, the effect of interfacial slip is of suppressing the deformation of the drop. In the whole Ca-range explored, i.e., for $Ca \leq 0.1$, the numerical data overlap the theoretical predictions.

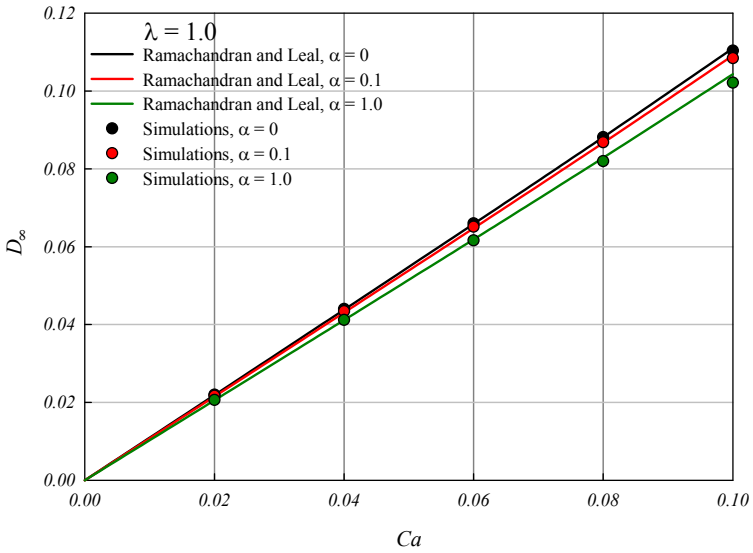

Figure 2.11: Steady deformation parameter D_∞ of a Newtonian drop in a Newtonian fluid under unbounded shear flow, in the presence of interfacial slip, as function of the capillary number Ca. The circles represent numerical simulations, the solid lines represent theoretical predictions from [85]. The viscosity ratio is $\lambda = 1.0$.

2.5.2 Deformation of a viscoelastic drop in a Newtonian fluid

In the moderate Ca regime, even viscoelastic drops suspended in Newtonian fluids subjected to unbounded shear flow deform into ellipsoids with a fixed orientation with respect to the flow axis. In this case, besides the viscosity ratio λ, the number $p_\mathrm{d} = \frac{\Psi_{1,\mathrm{d}}\Gamma}{2R_0\eta_\mathrm{d}^2}$ is a physical parameter of the system.

In 2002, Greco [43] performed perturbative analytical calculations of the deformation and orientation of a viscoelastic drop in a viscoelastic fluid under unbounded shear flow, from which it emerges that no differences arise for the deformation parameter with respect to what shown by Taylor for a Newtonian drop in a Newtonian fluid, whereas the orientation angle (in radians) is:

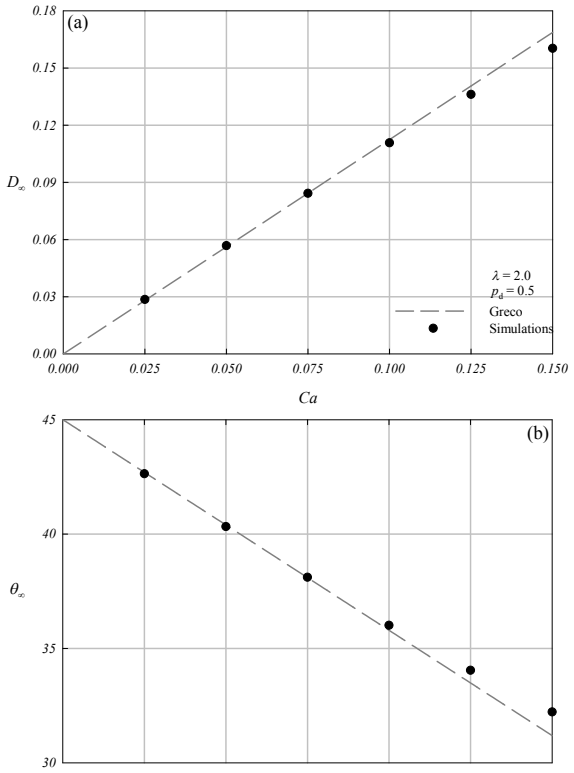

Figure 2.12: Deformation of an UCM viscoelastic drop in a Newtonian fluid under unbounded shear flow. a) D_∞ vs. Ca. b) θ_∞ vs. Ca. For both panels, $\lambda = 2.0$, $p_\mathrm{d} = 0.5$; dashed line: theoretical predictions from [43]; black circles: our numerical simulations.

$$\theta_\infty = \frac{\pi}{4} - Ca\frac{(16+19\lambda)(3+2\lambda)}{80(1+\lambda)} + \\ - Ca\left[p\frac{176+436\lambda+323\lambda^2}{30(1+\lambda)(16+19\lambda)} + p_\mathrm{d}\frac{9\lambda^2+6\lambda^3}{8(1+\lambda)(16+19\lambda)}\right] \quad (2.60)$$

From the general result, the cases of a viscoelastic drop in a Newtonian matrix ($p = 0$) and of a Newtonian drop in a viscoelastic matrix ($p_\mathrm{d} = 0$) can be derived. In Figure 2.12a, the theoretical prediction from [43] for the steady deformation parameter $D_\infty(Ca)$ of a viscoelastic drop in a Newtonian matrix with $\lambda = 2.0$ and $p_\mathrm{d} = 0.5$ is plotted as a gray dashed line, and compared with our data (the black circles) for an UCM drop. It is evident that, for

$Ca \leq 0.1$, the points quantitatively overlap the curve, then a slight negative deviation starts to be seen. For the steady orientation angle θ_∞, as displayed in Figure 2.12b, where the same symbols as in panel (a) are used, analogous remarks can be made, the deviation of the simulation results with respect to the theory for $Ca > 0.1$ being positive.

2.5.3 Deformation of an elastic particle in a Newtonian fluid

An initially spherical neo-Hookean elastic particle in a Newtonian fluid subjected to unbounded shear flow deforms because of the applied flow until it attains an ellipsoidal steady shape with a fixed orientation with respect to the flow direction. The Taylor deformation parameter D, and the orientation angle θ are evaluated.

In Figure 2.13a, the temporal trends of the deformation parameter D are plotted for eight values of the elastic capillary number Ca_e going from 0.01 to 0.5. The deformation of the particle in the shear plane is higher as Ca_e increases. From a dynamic point of view, the higher Ca_e, the more time the particle needs to reach the steady deformed shape. In Figure 2.13b, the temporal trends of the orientation angle θ are plotted for the same eight values of Ca_e as in panel (a): as Ca_e tends to 0, the particle tends to orient at 45° with respect to the flow direction, whereas, as Ca_e increases, its orientation progressively tends to align with the flow axis (it is verified that the major semiaxis L does not go out of the shear plane). It can be also noticed that for higher Ca_e-values, the particle needs more time to reach its steady orientation.

As reported in Section 1.2.3, in 1967, Roscoe [90] investigated from a theoretical point of view the rheological behavior of an initially spherical viscoelastic particle in a viscous liquid in the linear Ca_e-regime, showing that steady-state solutions are possible such that the particle deforms into an ellipsoid of fixed orientation, with the deformation and the orientation depending on a flow parameter. In 2011, Gao et al. [36] employed a (non-

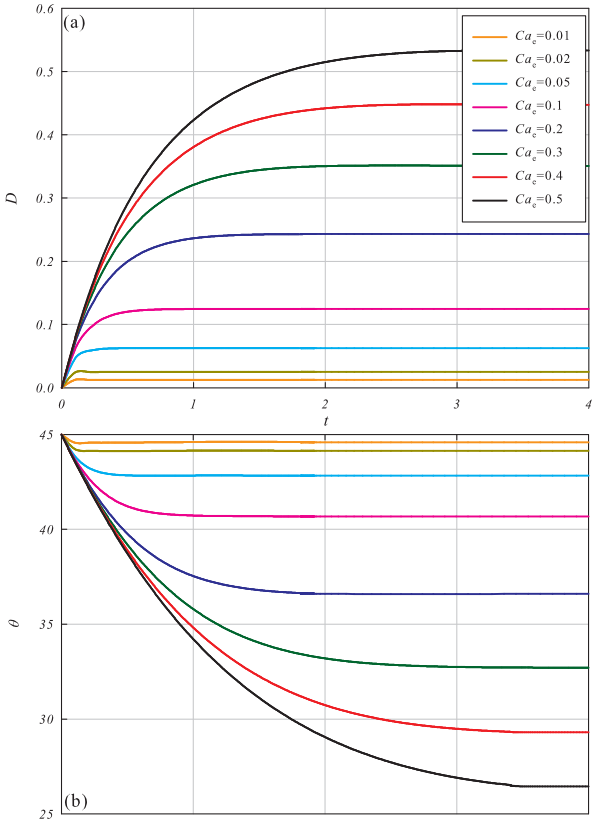

Figure 2.13: Dynamics of the deformation of a neo-Hookean elastic particle in a Newtonian fluid under unbounded shear flow. a) D vs. dimensionless time t for eight values of Ca_e; b) θ vs. t for the same eight Ca_e-values.

perturbative) polarization technique to study the behavior of a neo-Hookean sphere suspended in a Newtonian fluid under unbounded shear flow, obtaining results that successfully overlap Roscoe ones in the linear Ca_e-regime (i.e., for $Ca_e \leq 0.2$), and extend them outside it. In Figure 2.14a, the steady values of D taken from Figure 2.13a are plotted *vs.* Ca_e as black circles. On the same graph, the theoretical predictions by Roscoe and Gao et al. are reported as a gray dashed line and red diamonds, respectively. It clearly emerges that a very satisfactory quantitative agreement is achieved with both for $Ca_e \leq 0.2$, and with Gao et al for $Ca_e > 0.2$. So it is for the stationary

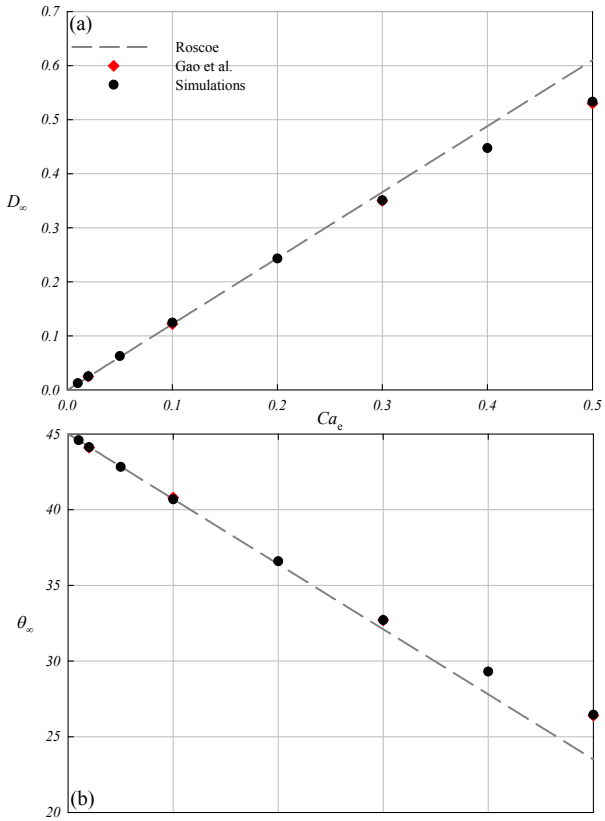

Figure 2.14: Steady deformation of a neo-Hookean elastic particle in a Newtonian fluid under unbounded shear flow. a) D_∞ vs. Ca_e; b) θ_∞ vs. Ca_e. For both panels, gray dashed line: theoretical predictions from [90]; red diamonds: theoretical predictions from [36]; black circles: our numerical simulations.

orientation angle θ_∞ too, whose values are displayed in Figure 2.14b as black circles: the comparison with Roscoe, for $Ca_e \leq 0.2$, and Gao et al., in the whole Ca_e-range, gives even in that case a very good quantitative agreement.

In [36], Gao et al. also give analytical expressions for the principal components of the extra-stress tensor in the particle, that they find to be uniform in it. For $Ca_e = 0.2$, we compare our numerical results, from which we see a uniform elastic stress in the particle as well, with their predictions; this is shown in Figure 2.15, where the temporal evolution of the principal components of the extra-stress tensor in the particle are reported (all quantities

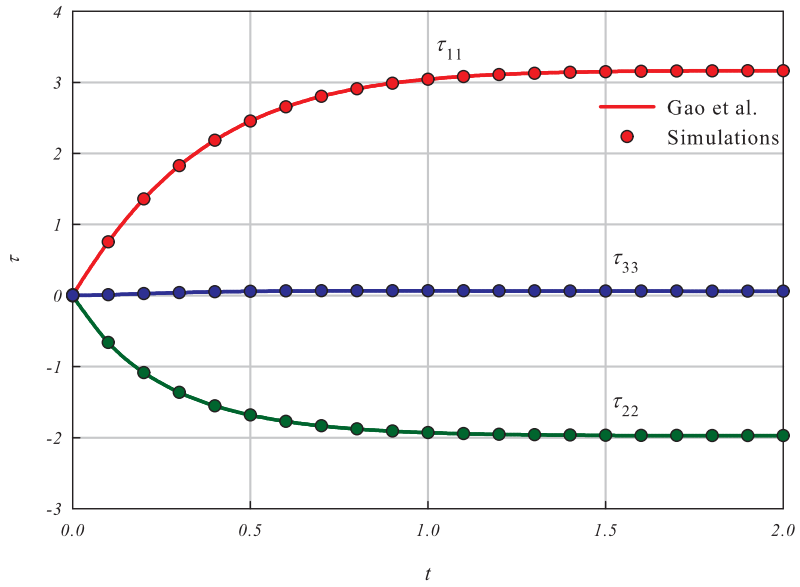

Figure 2.15: Principal components of the extra-stress tensor in a neo-Hookean elastic particle in a Newtonian fluid under unbounded shear flow with $Ca_e = 0.2$. Solid lines: theoretical predictions from [36]; circles: our numerical simulations.

being dimensionless, as usual). The solid lines are the analytic expressions given in Section 4.2 in [36], the red curve representing τ_{11} (the stress component in the direction of the major semi-axis of the ellipsoid in the shear plane), the green curve representing τ_{22} (the stress component in the direction of the minor semi-axis of the ellipsoid in the shear plane), and the blue curve representing τ_{33} (the stress component in the direction of the semi-axis of the ellipsoid orthogonal to the shear plane). With the same color code, our numerical results are displayed as circles. It clearly emerges from the figure that theoretical and numerical results quantitatively agree over the whole time-window considered, each set of points overlapping to the corresponding analytical curve.

2.6 Final remarks

In this chapter, an arbitrary Lagrangian Eulerian finite element method based numerical code for viscoelastic fluids using well-known stabilization techniques (SUPG, DEVSS, log-conformation) is adapted and extended to study the behavior of soft systems, such as liquid drops and elastic particles, suspended in flowing media in 3D.

Both drops and elastic particles are modeled as fluids (the particles being treated as drops of an upper-convected Maxwell fluid with a very large relaxation time): for this reason, the interface between the suspended objects and the matrix needs to be tracked. To do this, a finite element method with second-order time discretization is defined on the interface, where its normal velocity equals the normal component of the fluid velocity, and the tangential velocity is such that the distribution of the elements on the interface is optimized. The advantage of this approach is that at the interface the mesh does not follow the tank-treading motion of the particle, thus greatly reducing the distortion of the ALE volume mesh as compared to a Lagrangian description of the interface. In order to stabilize the interface, the SUPG method is used.

A validation of the code is done for soft systems suspended in Newtonian fluids under unbounded shear flow: for a Newtonian drop, in the no-slip case, our results are compared with Taylor predictions [95], and experimental data from Guido and Villone [49]; in the presence of interfacial slip, with theoretical predictions from Ramachandran and Leal [85]; for an upper-convected Maxwell drop in a Newtonian matrix, numerical data are compared with the front tracking finite difference simulations from Aggarwal and Sarkar [1]; for a neo-Hookean elastic particle, simulation outcomes are compared with theoretical predictions by Roscoe [90] and Gao et al [36]. In all the above mentioned cases, a very good quantitative agreement is found between the results by other authors and ours.

Chapter 3

A single-body problem: numerical simulations of an elastic particle in Newtonian and viscoelastic fluids subjected to confined shear flow

3.1 Introduction

In the present chapter, the behavior of an initially spherical elastic particle suspended in confined shear flow of a Newtonian and a Giesekus viscoelastic liquid is studied by means of 3D arbitrary Lagrangian Eulerian finite element method numerical simulations. Due to the applied flow, the particle deforms; in addition, the presence of solid walls in its vicinity can make it migrate transversally to the streamlines of the suspending medium. The effect of the geometrical and physical parameters of the system on both the deformation and the migration of the soft particle in both the Newtonian and the viscoelastic matrix is investigated.

The schematic drawing of an initially spherical elastic particle suspended

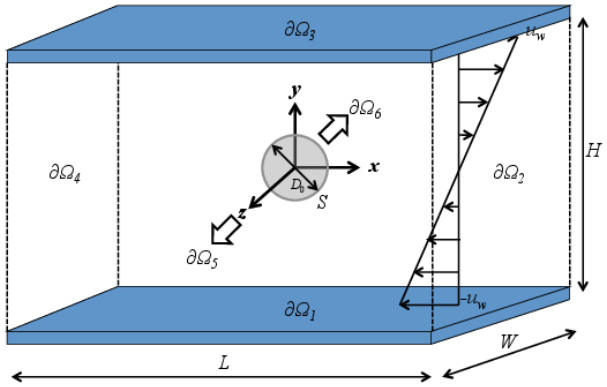

Figure 3.1: Geometry of an initially spherical elastic particle suspended in a fluid under shear flow.

in a fluid under simple shear (already displayed in Figure 2.1) is reported above. For both the suspended particle and the suspending phase, it is assumed that inertia can be neglected and that the volume is constant (i.e., the materials are incompressible). The balance and constitutive equations that describe the system, with the relative boundary conditions, for both a Newtonian and a Giesekus suspending liquid, are given in Sections 2.2.1 - 2.2.2.

In this chapter we choose to make the equations dimensionless by using the channel gap H as the characteristic length, the inverse of the imposed shear rate $1/\dot{\gamma} = H/2u_{\mathrm{w}}$ as the characteristic time, $\eta_{\mathrm{m}}\dot{\gamma}$ as the characteristic stress in the matrix and the shear modulus of the elastic material G_{p} as the characteristic stress in the particle. The elastic capillary number, defined as $Ca_{\mathrm{e}} = \eta_{\mathrm{m}}\dot{\gamma}/G_{\mathrm{p}}$, which is the ratio between the viscous forces and the elastic forces to which the particle is subjected, arises, then, from Equation (2.19). In case a viscoelastic matrix is considered, the non-Newtonian counterpart of Ca_{e} is $N = N_1/2G_{\mathrm{p}}$ (with N_1 the first normal stress difference in

the viscoelastic matrix), which is the ratio between the elastic forces in the suspending fluid and the particle, respectively. From the definitions given above, the dimensionless parameter that gives the relative weights of the elastic and viscous actions of the matrix on the particle is $p = N/Ca_e^2$. In analogy to what shown for drops by Greco in [43], p is a measure of the 'non-Newtonianness' of the problem. All the results appearing in the following sections are made dimensionless through the above mentioned characteristic quantities.

The model equations have been solved through the code presented in detail in Chapter 2. Before running simulations, convergence tests have been performed in space and time, i.e., mesh resolution and time-step have been chosen that ensure invariance of the results upon further refinements. For the simulations presented in this chapter, we have found that meshes with a number of tetrahedra in the order of $2 - 4 * 10^4$ and time-steps in the order of $1 - 2 * 10^{-3}\dot{\gamma}^{-1}$ are adequate. A detailed description of the procedures adopted to run convergence tests for the problem of our interest is given in Chapter 2. Moreover, since periodicities are imposed in the flow and the vorticity directions, the x and z-dimensions of the domain have been chosen such that the particle does not feel the influence of its periodic images along these directions: in all the cases shown in the following, the channel is 10 times the particle diameter. We have performed our simulations on blades with two hexa-core processors Intel Xeon E5649@2.53GHz and 48 GB of RAM. The computational time needed to produce the results reported in the next section ranges from 2-3 days for a Newtonian suspending fluid to 2-3 weeks for a Giesekus matrix.

3.2 Results and discussion

An initially spherical neo-Hookean elastic particle is suspended in a fluid subjected to shear flow, as shown in Figure 3.1. Unlike in Chapter 2, the particle is confined in the velocity gradient direction, which means that the

ratio of the diameter of the undeformed particle D_p and the channel gap H assumes a finite value β, to which we refer as the *blockage ratio*; on the contrary, we have $W \gg D_\mathrm{p}$, so no confinement exists in the vorticity direction. In what follows, when we refer to the vertical position of the particle y_p, we mean the y-position of its center of volume on the xy-plane (the z-coordinate being irrelevant, since $W \gg D_\mathrm{p}$). Similarly, when we mention the migration velocity of the particle, we mean the y-component of the translational velocity computed in its center of volume. The origin of the reference frame is placed at the center of the flow channel.

3.2.1 Deformation of a neo-Hookean particle in a Newtonian fluid

In this section, the case of a neo-Hookean particle suspended in Newtonian fluid in a symmetric position between the walls is considered.

Due to the applied flow, the particle deforms until it attains a steady ellipsoid-like shape with a fixed orientation with respect to the flow direction. In Figure 3.2, the projection on the velocity-gradient (xy) plane of the particle steady shape is displayed for a moderately confined situation ($\beta = 0.2$, see Figure 3.2a), and a strongly confined one ($\beta = 0.6$, in Figure 3.2b), and for four Ca_e-values, i.e., $Ca_\mathrm{e} = 0.05,\ 0.2,\ 0.35,\ 0.5$. The points shown in the graph (each color corresponding to a fixed Ca_e-value), are the nodes of the particle-matrix interface mesh lying on the above mentioned plane within a small tolerance in the z-direction. In order to highlight the deviation of the deformed particle from the initial spherical shape, the circle representing the projection of the undeformed sphere on the xy-plane is also shown in the graph as a dashed line; moreover, to facilitate the comparison of the results shown in the two panels, the coordinates of each point are normalized by the radius of the corresponding undeformed particle. From both Figures 3.2a and 3.2b, it is evident that, at fixed β, as the elastic capillary number increases, the particle becomes increasingly deformed with respect to the original shape, and progressively tends to align with the x-axis, which is

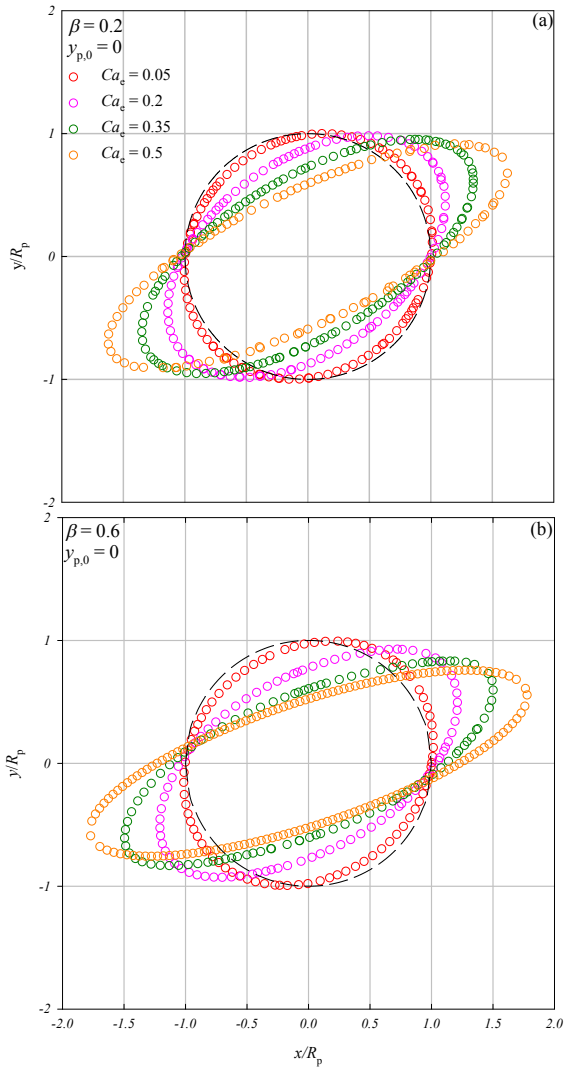

Figure 3.2: Projection on the xy-plane of the shape of a deformed neo-Hookean particle in a Newtonian fluid under confined shear flow for five Ca_e-values. a) $\beta = 0.2$; b) $\beta = 0.6$. The particle is placed in a symmetric position between the walls. The black dashed circle is the projection of the initial spherical shape of the particle.

the flow direction. On the other hand, at fixed Ca_e, the more confined particle, displayed in Figure 3.2b, is more deformed and more flow-aligned than the less confined one, shown in Figure 3.2a, such difference becoming more evident at high Ca_e-s (see, for example, the green circles, representing

the case at $Ca_e = 0.35$, and the orange circles, for which $Ca_e = 0.5$). As we

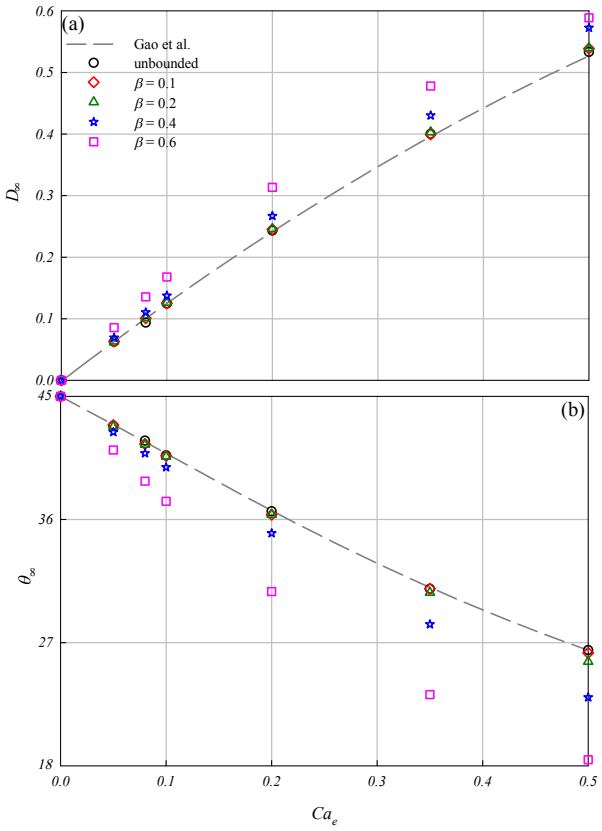

Figure 3.3: Steady deformation of a neo-Hookean elastic particle in a Newtonian fluid under confined shear flow. The particle is placed in a symmetric position between the walls. (a) D_∞ vs. Ca_e for five values of the blockage ratio β; (b) θ_∞ vs. Ca_e for the same five β-values.

see from Figure 3.2, the steady deformed shape of a neo-Hookean particle suspended in Newtonian fluid in a symmetric position between the walls is very close to an ellipsoid. The Taylor deformation parameter is defined as the ratio of the difference and the sum of the major and minor semiaxes of the ellipsoid in the shear plane. From the projection of the particle shape on the xy-plane, the steady Taylor deformation parameter D_∞ and the angle θ_∞ between the ellipsoid major semi-axis and the flow direction are evaluated at

varying β and Ca_e.

In Figure 3.3a, D_∞ is plotted as a function of the elastic capillary number Ca_e for $Ca_e \leq 0.5$, and $\beta = 0$ (unbounded case), 0.1, 0.2, 0.4, 0.6. In addition, the theoretical predictions by Gao et al. [36] (that, for $Ca_e \leq 0.2$, reproduce Roscoe [90]) for the deformation of an elastic particle in a Newtonian fluid in unconfined shear flow are reported as a gray dashed curve. It is already said in Chapter 2 that, in unbounded shear flow, our simulations show an excellent quantitative agreement with [36] for $Ca_e \leq 0.5$, as proved by the fact that the black circles lie along the gray dashed line in the whole Ca_e-range explored. By looking at the graph, it emerges that, in the confined situation, the $D_\infty - vs. - Ca_e$ trends are qualitatively similar to the trend in the unbounded case: below $Ca_e = 0.2$, D_∞ grows linearly with Ca_e, then the growth becomes less than linear. From the quantitative point of view, it can be seen that the presence of the walls has no substantial influence for a blockage ratio up to 0.2, since the red diamonds ($\beta = 0.1$) and the green triangles ($\beta = 0.2$) almost overlap the black circles for all the values of the capillary number considered; instead, for $\beta = 0.4$ and 0.6 (the blue stars and the pink squares, respectively), D_∞ appreciably increases with respect to the unbounded value, the difference progressively growing with Ca_e, and reaching about 10% for $\beta = 0.6$ and $Ca_e = 0.5$. In Figure 3.3b, the steady orientation angle θ_∞ is displayed as a function of Ca_e for the same five β-values as in panel (a). Like in Figure 3.3a, Gao et al. predictions are reported as a gray dashed line (also for θ_∞ such predictions reproduce Roscoe for $Ca_e \leq 0.2$). Similar considerations as for D_∞ can be made: below $Ca_e = 0.2$, θ_∞ linearly decreases with Ca_e, starting from the limit value of $\frac{\pi}{4}$ (i.e., 45°); the qualitative $\theta_\infty - vs. - Ca_e$ trends do not change in the confined case with respect to the unconfined one, θ_∞ decreasing with Ca_e for every β. From the quantitative point of view, for $\beta = 0.1$ and 0.2, almost no differences with the unconfined system are seen (except of $\beta = 0.2$ and $Ca_e = 0.5$, where the green triangle is below the black circle and the red diamond of about 2.5%); for $\beta = 0.4$ and 0.6, the particle has a progressively greater

tendency to align with the flow, as shown by the fact that the blue stars and the pink squares visibly lie below the other symbols, and the θ_∞-decrease becomes more evident as Ca_e increases, reaching about 30% with respect to the unbounded case for $\beta = 0.6$ and $Ca_e = 0.5$.

As written above, when Ca_e is below 0.2, both D_∞ and θ_∞ are linear with it for every β. Thus, in that low-Ca_e regime, we can write:

$$D_\infty = \frac{5}{4}(1 + A(\beta))Ca_e \tag{3.1}$$

$$\theta_\infty - \frac{\pi}{4} = -\frac{3}{4}(1 + B(\beta))Ca_e \tag{3.2}$$

with $\frac{5}{4}(1 + A(\beta))$ and $-\frac{3}{4}(1 + B(\beta))$ the (β-depending) slopes of the linear trends of the steady deformation parameter and orientation angle with Ca_e, respectively (factors $\frac{5}{4}$ and $-\frac{3}{4}$ come from the consideration that, when $\beta = 0$, we have to recover Roscoe theory). From the interpolation of the data shown in Figure 3.3 for $Ca_e \leq 0.2$, we get, for every β, the corresponding A- and B-values; if we, then, interpolate the $A - vs. - \beta$ and $B - vs. - \beta$ data sets, we obtain:

$$A(\beta) = \frac{8}{5}\beta^3 \tag{3.3}$$

$$B(\beta) = \frac{11}{3}\beta^3 \tag{3.4}$$

It is worth remarking that such cubic β-dependence of A and B quantitatively confirms what qualitatively observed by looking at the results shown in Figure 3.3, namely, that a low confinement (e.g. $\beta = 0.1, 0.2$) does not significantly influence the steady deformation and orientation of the particle in the low-Ca_e range. By combining Equations (3.1) - (3.4), it is possible to express the steady orientation angle θ_∞ as a function of the steady deformation parameter D_∞. This yields:

$$\theta_\infty - \frac{\pi}{4} = -\frac{3}{5}\frac{(1 + \frac{11}{3}\beta^3)}{(1 + \frac{8}{3}\beta^3)}D_\infty \tag{3.5}$$

Notice that, since for $Ca_e \leq 0.2$ both θ_∞ and D_∞ are linearly dependent on Ca_e, such dependence disappears if we write the angle as a function of

the deformation parameter, the only parameter in Equation (3.5) being β. Then, for any fixed value of the blockage ratio β, we can plot the steady orientation of the particle θ_∞ *vs.* the corresponding steady deformation D_∞ (thus 'hiding' the variation of the elastic capillary number Ca_e); in Figure 3.4, this is done for $\beta = 0$, 0.1, 0.2, 0.4, 0.6. By looking at the graph, it can be noticed that, for every β, θ_∞ linearly decreases with D_∞ over the whole D_∞-range (hence, Ca_e-range) considered. If we compare the sets of points at varying β displayed in Figure 3.4 with the results of Equation (3.5) (see the dashed lines in Figure 3.4), we discover that such function (obtained in the limit of low Ca_e, where both D_∞ and θ_∞ can be considered to be linearly dependent on that parameter) quantitatively describes the $\theta_\infty(D_\infty)$-trend over the whole range of Ca_e explored, even if D_∞ and θ_∞ are individually no longer linear functions of Ca_e.

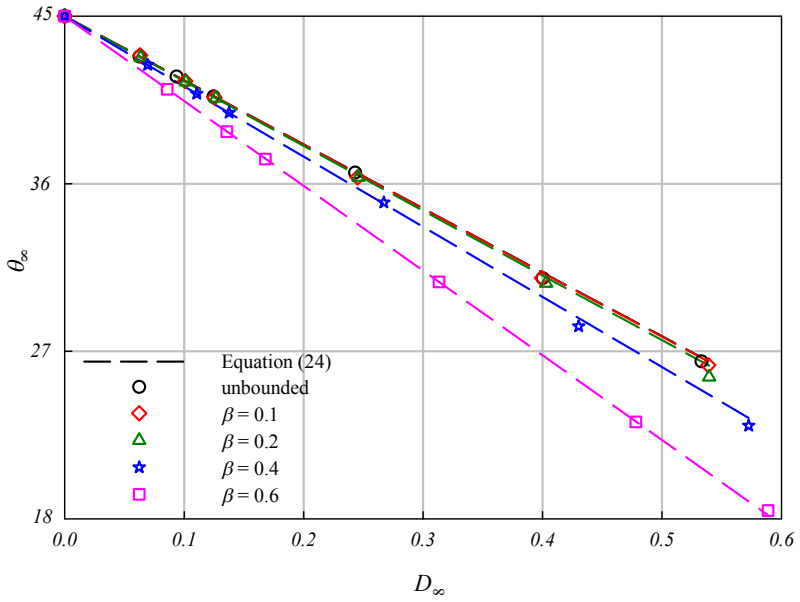

Figure 3.4: Steady orientation θ_∞ of a neo-Hookean elastic particle in a Newtonian fluid under confined shear flow as a function of its steady deformation parameter D_∞ for five values of the blockage ratio β. The particle is placed in a symmetric position between the walls. The dashed lines show the trends of the fitting function given in Equation (3.5)

3.2.2 Migration of a neo-Hookean particle in a Newtonian fluid

An initially spherical neo-Hookean elastic particle is now suspended out of the velocity-vorticity symmetry plane (i.e., the mid plane) of a channel filled with a Newtonian fluid under shear flow (so, it is $y_{p,0} \neq 0$). In analogy to what is shown in Section 3.2.1, the particle deforms because of the applied flow, but, due to the asymmetry of its initial position along the velocity gradient direction (it starts closer to one wall of the channel than to the other), the deformed shape is no longer ellipsoidal (thus, symmetric). A new phenomenon correspondingly arises, which is the cross-streamline migration of the particle.

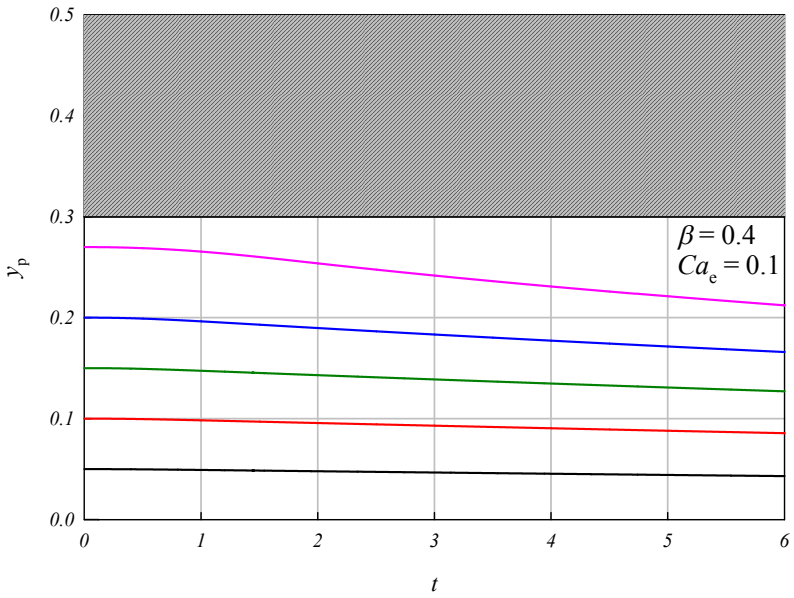

Figure 3.5: Trajectories, at varying initial position, of a neo-Hookean particle in a Newtonian fluid under confined shear flow. The blockage ratio is $\beta = 0.4$, the capillary number is $Ca_e = 0.1$. The shaded region represents the portion of the channel not physically accessible by the center of mass of the particle.

In Figure 3.5, the trajectories of the particle, with reference to the position

of its center of volume y_p, are displayed for $\beta = 0.4$ and $Ca_e = 0.1$. Five initial vertical positions are considered in the upper half of the channel, the dynamics in the lower half being analogous (mirrored) due to symmetry; in particular, such positions are $y_{p,0} = 0.05, 0.10, 0.15, 0.20, 0.27$ (notice that, given $\beta = 0.4$, a sphere touching the wall has $y_p = 0.30$). By looking at the graph, it can be seen that, wherever the particle is initially placed, it always migrates towards the center of the channel.

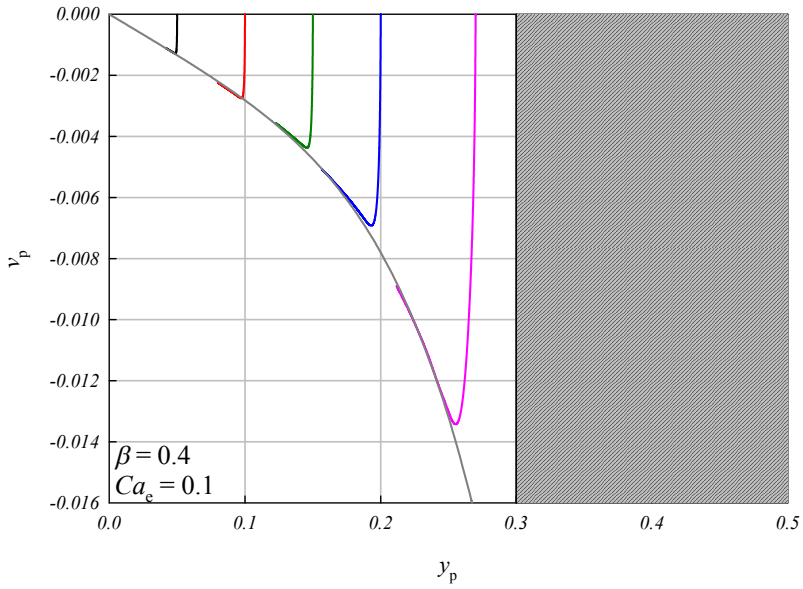

Figure 3.6: Migration velocity v_p of a neo-Hookean particle in a Newtonian fluid under confined shear flow as a function of its vertical position y_p. The gray solid line is the migration velocity master curve. The blockage ratio is $\beta = 0.4$, the capillary number is $Ca_e = 0.1$. The shaded region represents the portion of the channel not physically accessible by the center of mass of the particle.

In Figure 3.6, we plot the migration velocity of the particle *vs.* its vertical position in the upper semi-channel for the same blockage ratio, capillary number, and starting positions considered in Figure 3.5: it can be seen that the curves corresponding to different initial positions, if we exclude the very early stages of the dynamics, all arrange along a single master curve (the gray solid line in Figure 3.6), that, then, entirely rules the migration dynamics of

the particle, at fixed β and Ca_e, in the whole channel. In particular, it emerges that the migration is faster as the particle is closer to the wall, whereas the migration velocity asymptotically tends to zero as the particle approaches the center plane, where no migration is actually detected.

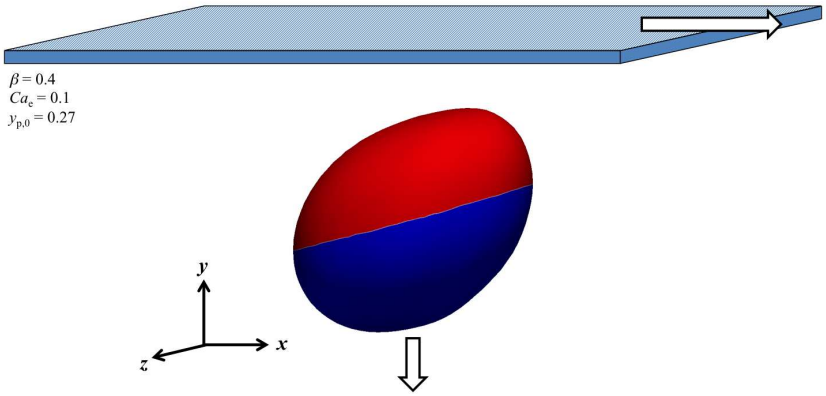

Figure 3.7: 3D view of the shape of a deformed neo-Hookean particle in a Newtonian fluid under confined shear flow; the red portion of the surface has positive y-component of the outwardly directed unit vector $\boldsymbol{n}$, whereas the blue portion has negative y-component of $\boldsymbol{n}$. The blockage ratio is $\beta = 0.4$, the capillary number is $Ca_e = 0.1$. The snapshot refers to the vertical position $y_p = 0.213$, the particle having started from $y_{p,0} = 0.27$.

As hinted above, when an initially spherical elastic particle is suspended out of the velocity-vorticity symmetry plane in a fluid under confined shear flow, it deforms attaining an asymmetric shape. A snapshot of this is given, for $\beta = 0.4$ and $Ca_e = 0.1$, in Figure 3.7, where a 3D view of the deformed shape of a particle starting from $y_{p,0} = 0.27$ is shown. The image is taken at a height $y_p = 0.213$, with the particle migrating downwards (i.e., towards the center plane of the channel). The white line marks the intersection between the particle surface and a plane that divides the body in two portions, the one (displayed in red) characterized by a positive y-component n_y of the out-

wardly directed unit vector normal to the surface $\boldsymbol{n}$, and the other (displayed in blue) with negative n_y. In other words, the white line is the *locus* of the points on the surface of the particle where the normal unit vector is parallel to the moving plates of the flow cell. Even if it is not manifest from the image, the red area exceeds the blue area. We define the 'surface imbalance' of the particle as the discrepancy of the the surface area with positive n_y and the surface area with negative n_y, normalized by one half of the the total actual surface area of the particle; in symbols:

$$\Delta S = \frac{S_{\mathrm{p},n_y^+} - S_{\mathrm{p},n_y^-}}{S_{\mathrm{p}}/2} \tag{3.6}$$

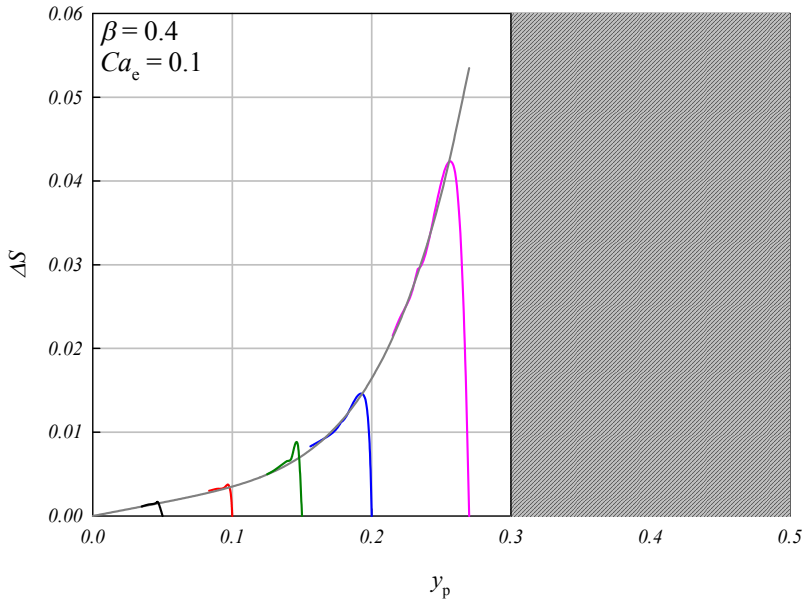

Figure 3.8: Surface imbalance ΔS of a neo-Hookean particle in a Newtonian fluid under confined shear flow as a function of its vertical position y_{p}. The gray solid line is the surface imbalance master curve. The blockage ratio is $\beta = 0.4$, the capillary number is $Ca_{\mathrm{e}} = 0.1$. The shaded region represents the portion of the channel not physically accessible by the center of mass of the particle.

For the same flow conditions as in Figures 3.5 and 3.6, such quantity is plotted in Figure 3.8 as a function of the particle vertical position y_{p}. Like

for the migration velocity v_p, the curves corresponding to the five different initial positions, excluding the very early stages, all lie on a single master curve (the gray solid line), that gives the surface imbalance of the particle in the whole channel. By looking at Figure 3.8, it should be noticed that, for the β- and Ca_e-values taken into account, the master curve is everywhere positive in the upper half of the channel, which means that the portion of the surface area with positive n_y is everywhere greater than the portion of the surface area with negative n_y. From the comparison of Figures 3.8 and 3.6, it can be seen that the magnitude of the migration velocity, whose sign is negative everywhere in the upper half of the channel, grows with the surface imbalance, i.e., the more the surface area with positive n_y overtakes the surface area with negative n_y, the faster the particle migrates downwards.

The effects of the blockage ratio β and of the capillary number Ca_e on the migration velocity of a neo-Hookean particle in a Newtonian fluid under confined shear flow are shown in Figures 3.9a and 3.9b, respectively. In Figure 3.9a, the migration velocity master curves are plotted *vs.* the vertical position of the particle y_p in the upper half of the channel, normalized by the maximum attainable height $y_\mathrm{p,max}$, for $Ca_\mathrm{e} = 0.1$ and five different values of the blockage ratio β; instead, in Figure 3.9b, the migration velocity master curves are reported for $\beta = 0.2$ and five different values of the capillary number Ca_e. From such figures, it emerges that neither the change of the particle confinement nor the change of the capillary number have any qualitative effect on the trend of the migration velocity of the particle, that is always negative in the whole upper half of the channel, with its magnitude decreasing from the wall to the center. In other words, for all the values of the parameters investigated, the particle always migrates towards the center plane of the channel, and moves faster when it is closer to the wall. From the quantitative point of view, at any fixed position $y_\mathrm{p}/y_\mathrm{p,max}$, v_p increases with both β and Ca_e, i.e., a more confined geometry and/or a more intense flow speed up the cross-stream migration.

If we put ourselves in the vicinity of the channel center plane, i.e., we

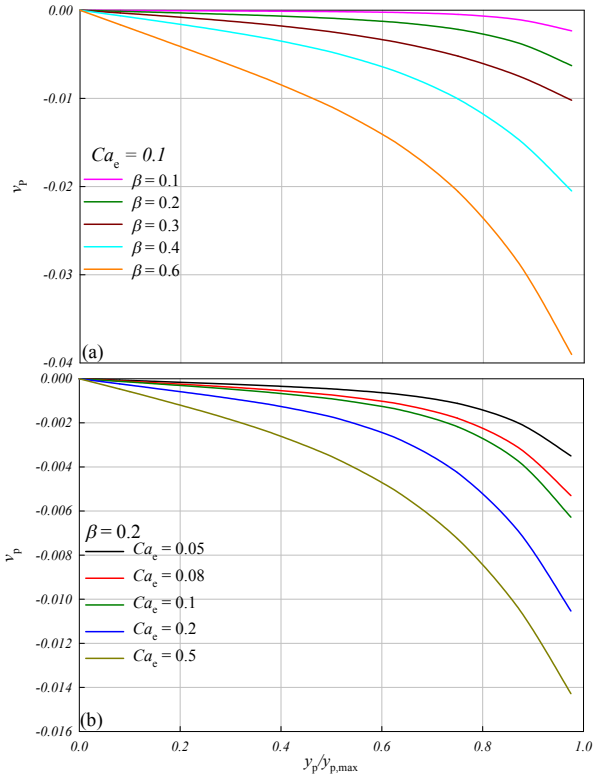

Figure 3.9: Effect of the blockage ratio β and of the capillary number Ca_e on the migration velocity v_p of a neo-Hookean particle in a Newtonian fluid under confined shear flow as a function of its normalized vertical position $y_p/y_{p,max}$. (a) Migration velocity v_p for $Ca_e = 0.1$ and four different β-values; (b) migration velocity v_p for $\beta = 0.2$, and five different Ca_e-values.

consider the region where $y_p/y_{p,max} \leq 0.1$, we can see that the migration velocity goes linearly with the vertical position of the particle. In other words, we can write:

$$v_p = f(\beta)g(Ca_e)\frac{y_p}{y_{p,max}} \tag{3.7}$$

with $f(\beta)g(Ca_e)$ the slope of the linear curve, depending on the parameters β and Ca_e. By interpolating the values of v_p arising from simulations for $y_p/y_{p,max} \leq 0.1$ at low β and Ca_e, we can give a functional form to the terms

$f(\beta)$ and $g(Ca_e)$ appearing in Equation (3.7); we obtain:

$$v_p = -2\beta^3 Ca_e \frac{y_p}{y_{p,max}} \tag{3.8}$$

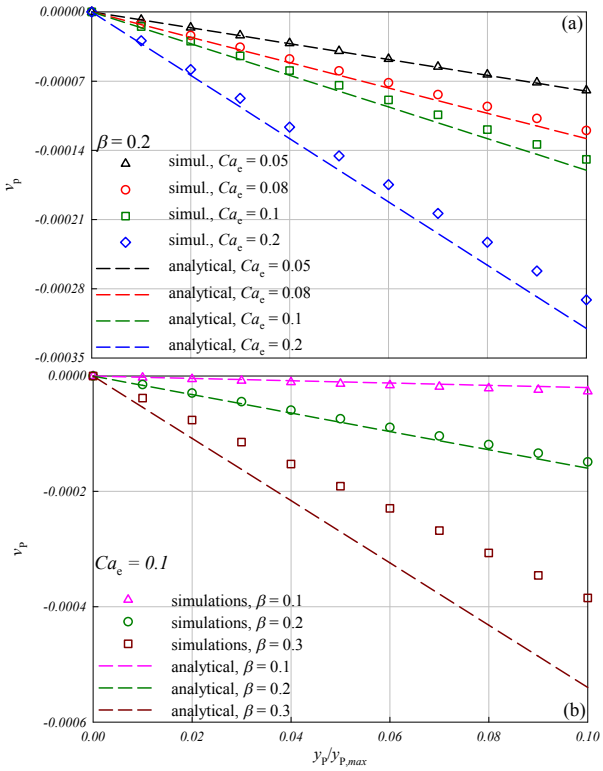

Figure 3.10: Effect of the blockage ratio β and of the capillary number Ca_e on the migration velocity v_p of a neo-Hookean particle in a Newtonian fluid under confined shear flow as a function of its normalized vertical position $y_p/y_{p,max}$ in the vicinity of the channel centerplane ($y_p/y_{p,max} < 0.1$). (a) Migration velocity v_p for $\beta = 0.2$ and four different Ca_e-values; (b) migration velocity v_p for $Ca_e = 0.1$ and three different β-values. In both panels, the dashed lines show the trends of the fitting function Equation (3.8).

Hence, the slope of the linear law that links the migration velocity to the height of the particle in the proximity of the channel center plane is a cubic function of the blockage ratio and a linear function of the capillary number. In Figure 3.10a, we report, for $y_p/y_{p,max} \leq 0.1$, $\beta = 0.2$, and Ca_e ranging from 0.05 to 0.2, the numerical migration velocities, as symbols, and the results

of Equation (3.8), as dashed lines of the same color. It can be seen that, under the given conditions, there is a fair quantitative agreement between the simulation data and the linear law (the greatest discrepancy being of less than 10% for $Ca_e = 0.2$ and $y_p/y_{p,max} = 0.1$). In Figure 3.10b, the same is done, fixed $Ca_e = 0.1$ and for $\beta = 0.1, 0.2, 0.3$: here, the agreement between simulation data and predictions from Equation (3.8) is very good for $\beta \leq 0.2$, but starts to become unsatisfactory for $\beta = 0.3$, where a discrepancy of 40% arises at $y_p/y_{p,max} = 0.1$.

Regarding the influence of the blockage ratio β and the capillary number Ca_e on the surface imbalance ΔS, remarks analogous to those made for the migration velocity may be made. The surface imbalance is always everywhere positive in the upper semi-channel (as shown, for $\beta = 0.4$ and $Ca_e = 0.1$, in Figure 3.8), and decreases as the particle gets closer to the center plane. The quantitative effect of the confinement is of enhancing the asymmetry of the particle deformation, i.e., fixed $y_p/y_{p,max}$ and Ca_e, ΔS grows with β. The same effect is produced by the capillary number: given a $y_p/y_{p,max}$-value and fixed β, ΔS grows with Ca_e. It is, then, possible to relate the particle migration velocity v_p to the surface imbalance ΔS (thus, 'hiding' the position of the particle), yielding a qualitative explanation of the fact that an inertialess elastic particle suspended out of the center plane of a channel filled with an inertialess Newtonian fluid under shear flow migrates transversally to the flow direction towards the above mentioned center plane: indeed, since no normal stresses arise in a Newtonian fluid, and the shear stress around the particle is uniform, the force exerted by the fluid on the particle from the wall side (i.e., in the upper semi-channel, on the portion of the particle surface characterized by a positive vertical component of the unit vector $\boldsymbol{n}$) overcomes the force exerted from the center side (i.e., in the upper semi-channel, on the portion of the particle surface characterized by a negative vertical component of the unit vector $\boldsymbol{n}$) due to the surface imbalance, this leading to a net transversal force in the direction of the center plane. As the surface imbalance grows, the net force acting on the elastic body grows, so

the migration speeds up.

3.2.3 Deformation of a neo-Hookean particle in a Giesekus fluid

In this section, the case of a neo-Hookean particle suspended in a flowing Giesekus liquid is examined. The constitutive parameter α_{m} (see Equation (2.6)) is chosen equal to 0.2. For simplicity, an unbounded shear flow is only considered, i.e., with $\beta = 0$. We aim at determining the effects of the non-Newtonianness of the suspending liquid on the particle deformation.

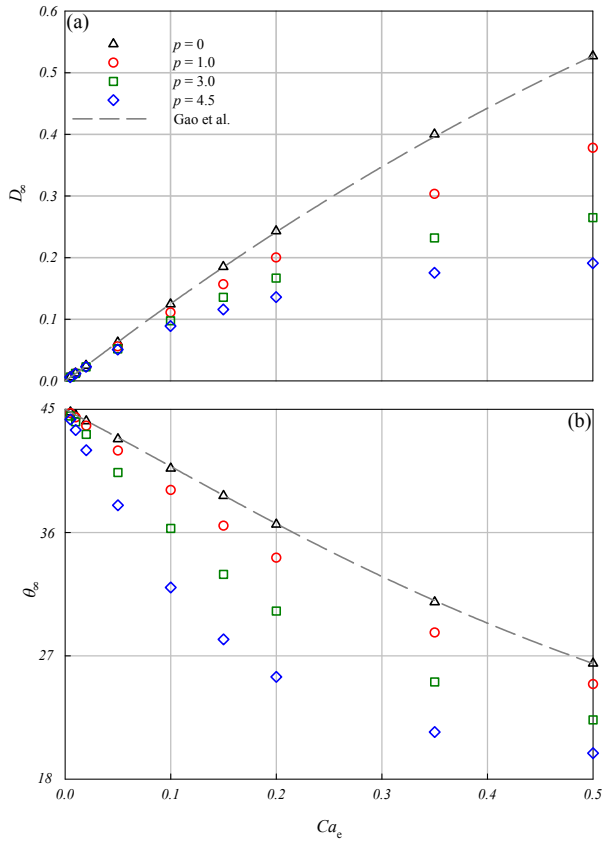

Figure 3.11: Steady deformation of a neo-Hookean elastic particle in a Giesekus viscoelastic fluid under unbounded shear flow. (a) D_∞ vs. Ca_e for five values of p; (b) θ_∞ vs. Ca_e for the same five p-values.

Due to the applied flow, the particle deforms until it attains a steady ellipsoid-like shape with a fixed orientation with respect to the flow direction; from the projection of the particle shape on the xy-plane, the steady Taylor deformation parameter D_∞ and orientation angle θ_∞ are evaluated at varying Ca_e and p. In Figure 3.11a, D_∞ is plotted as a function of the elastic capillary number Ca_e for $Ca_\mathrm{e} \leq 0.5$, and $p = 0$ (Newtonian matrix), 1.0, 3.0, 4.5; the theoretical prediction by Gao et al. [36] for the deformation of an elastic particle in a Newtonian fluid in unconfined shear flow is also reported as a gray dashed curve. It emerges from the figure that, as the elasticity of the suspending medium increases (i.e., as p increases), no significant qualitative differences are observed in the $D_\infty - vs. - Ca_\mathrm{e}$ trends, which are always linearly increasing in the low-Ca_e regime, to become less than linearly growing with increasing Ca_e; with respect to Ca_e, the 'loss of linearity' happens earlier as p increases. Quantitative differences at varying p are clearly visible for $Ca_\mathrm{e} \gtrapprox 0.1$, where, at fixed Ca_e, D_∞ decreases with p. Such result appears to be analogous to what theoretically predicted by Greco [43], and experimentally confirmed by Guido et al. [48], for Newtonian drops in unbounded shear flow of viscoelastic media. In Figure 3.11b, the steady orientation angle θ_∞ is displayed as a function of Ca_e for the same four p-values as in panel (a); like in Figure 3.11a, Gao et al. predictions are reported as a gray dashed line. The qualitative behavior of $\theta_\infty(Ca_\mathrm{e})$ at varying p is the same: starting from the limit value of $\frac{\pi}{4}$ (45°), in the low-Ca_e region θ_∞ linearly decreases with Ca_e, then the simulation results deviate upwards with respect to the linear trend. The (negative) slope of the $\theta_\infty - vs. - Ca_\mathrm{e}$ curves in the linear region changes with p, becoming increasingly steep as p grows up. Also those results are analogous to what theoretically predicted in [43], and experimentally confirmed in [48], for Newtonian drops in unbounded shear flow of viscoelastic media. An analysis analogous to that made in Section 3.2.1 can be made concerning the influence of the parameter p on the steady orientation angle θ_∞ at low Ca_e-s, yielding:

$$\theta_\infty - \frac{\pi}{4} = -\frac{3}{4}(1 + \frac{11}{75}p + \frac{2}{25}p^2)Ca_\mathrm{e} \tag{3.9}$$

3.2.4 Migration of a neo-Hookean particle in a Giesekus fluid

An initially spherical neo-Hookean elastic particle is suspended out of the velocity-vorticity symmetry plane of a channel filled with a Giesekus viscoelastic fluid under shear flow. The constitutive parameter α_{m} is again chosen equal to 0.2.

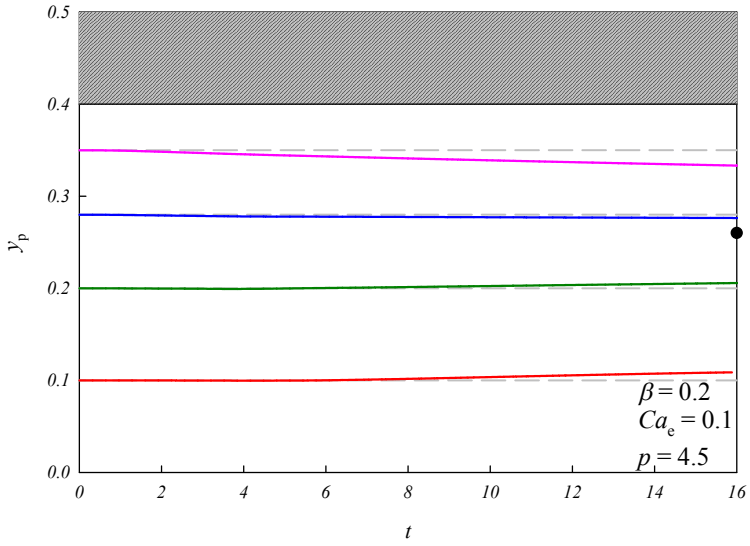

Figure 3.12: Trajectories, at varying initial position, of a neo-Hookean particle in a Giesekus fluid under confined shear flow. The blockage ratio is $\beta = 0.2$, the capillary number is $Ca_{\mathrm{e}} = 0.1$, the parameter p is equal to 4.5. The shaded region represents the portion of the channel not physically accessible by the center of mass of the particle.

In Figure 3.12, the trajectories of the particle are displayed for $\beta = 0.2$, $Ca_{\mathrm{e}} = 0.1$, and $p = 4.5$. Four initial vertical positions in the upper half of the channel are considered, i.e., $y_{\mathrm{p},0} = 0.10$, 0.20, 0.28, 0.35. Unlike the case with a Newtonian fluid, shown in Figure 3.5 above, the direction of the lateral migration of the particle now depends on its starting height. Indeed, when starting from $y_{\mathrm{p},0} = 0.28$ and 0.35, the particle migrates downwards, as in the Newtonian case, whereas, when starting from $y_{\mathrm{p},0} = 0.10$ and 0.20, it migrates upwards. Hence, at variance with the case with a Newtonian matrix, in the

presence of a viscoelastic matrix the center plane is no longer an attractor for the suspended body. Rather, the particle moves away from both the center plane and the wall of the channel towards an equilibrium position somewhere in between them (the black point in Figure 3.12, identified as explained below).

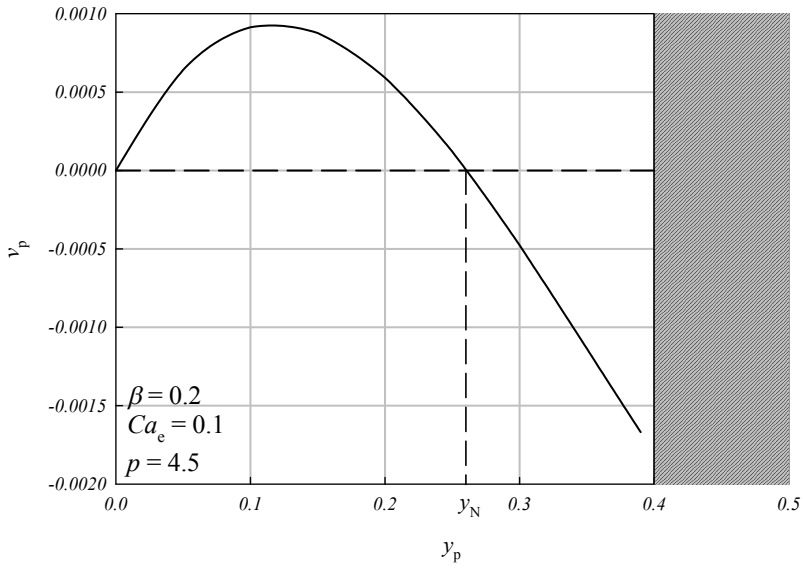

Figure 3.13: Migration velocity v_p (master curve) of a neo-Hookean particle in a Giesekus fluid under confined shear flow as a function of its vertical position y_p. The blockage ratio is $\beta = 0.2$, the capillary number is $Ca_e = 0.1$, the parameter p is equal to 4.5. The shaded region represents the portion of the channel not physically accessible by the center of mass of the particle.

As for the case with a Newtonian suspending phase, a migration velocity master curve exists, that rules the migration dynamics along the whole channel gap. The migration velocity master curve as a function of the particle vertical position is reported for $\beta = 0.2$, $Ca_e = 0.1$, and $p = 4.5$ in Figure 3.13. With respect to the Newtonian case (see Figure 3.6), there is a significative qualitative difference in the migration velocity trend, since here v_p is non-monotonic with y_p. Starting from $y_p = 0$, where $v_p = 0$, as the height in-

creases, the migration velocity first increases, reaches a maximum (at about $y_p = 0.16$), and then begins to decrease, until it becomes zero again: this happens at $y_p = 0.26$ (the abscissa of the point of intersection between the migration velocity master curve and the horizontal dashed line at $v_p = 0$ in Figure 3.13); for $y_p > 0.26$, v_p is negative. As in [100], we define the height at which the particle migration velocity is zero as the 'neutral height' y_N: given the trend of the migration velocity shown in Figure 3.13 (v_p positive below y_N and negative above it), such height identifies the stable equilibrium vertical position towards which the particle tends from every initial position in the upper semi-channel. Of course a symmetric situation exists in the lower semi-channel, with the particle migrating towards y_p = -0.26. The mid plane $y_p = 0$ is then an unstable equilibrium position, since we know that a particle suspended in an exactly symmetric position with respect to the walls does not migrate away from there, but any perturbation would make the particle move away from the center plane.

It is interesting to investigate what happens at varying elasticity of the matrix, i.e., at varying p. Then, we choose three Ca_e-values ($Ca_e = 0.1$, 0.2, 0.3), and, for each of those values, we run simulations by changing p. In Figure 3.14, the neutral height in the upper semi-channel is shown as a function of p for $Ca_e = 0.1$ (red circles), 0.2 (green triangles), 0.3 (blue squares): it can be seen that, at any fixed Ca_e, the neutral height moves towards the wall as p increases. Beyond a critical p, the neutral height goes to coincide with the upper wall. In other words, above a critical p-value the walls of the channel become attractors for the particle, and wherever the particle starts (except the very special unstable case of $y_{p,0} = 0$), it always migrates towards the closest wall. A similar phenomenon of 'attraction of the walls' was described by D'Avino et al. in [25] for a rigid sphere in confined shear flow of a Giesekus fluid; at variance with the present findings, however, a rigid sphere migrates towards the closest wall for any elasticity of the suspending fluid. Another nice result shown in Figure 3.14 is that the three series of points at three Ca_e-values all in fact arrange on a unique curve (the

gray dashed line displayed on the graph): this means that, regardless Ca_e, the parameter p effectively measures the competition of the two opposite actions to which the particle is subjected: on the one hand, the viscous stresses enhance the particle deformation, thus its migration towards the center (the limiting case being at $p = 0$, i.e., for a Newtonian matrix, where the particle always migrates towards the center of the channel); on the other hand, the elastic (normal) stresses depress the particle deformation, thus they push it to migrate towards the walls (the limiting case being at $p \to \infty$, i.e. for an undeformable particle, that always migrates towards the closest wall). In practice, we detect that, for p between 0 and ∼10, the competition between the two effects ends up in an 'equilibrium', so the migration of the particle is directed towards a neutral height in between the center plane and the wall.

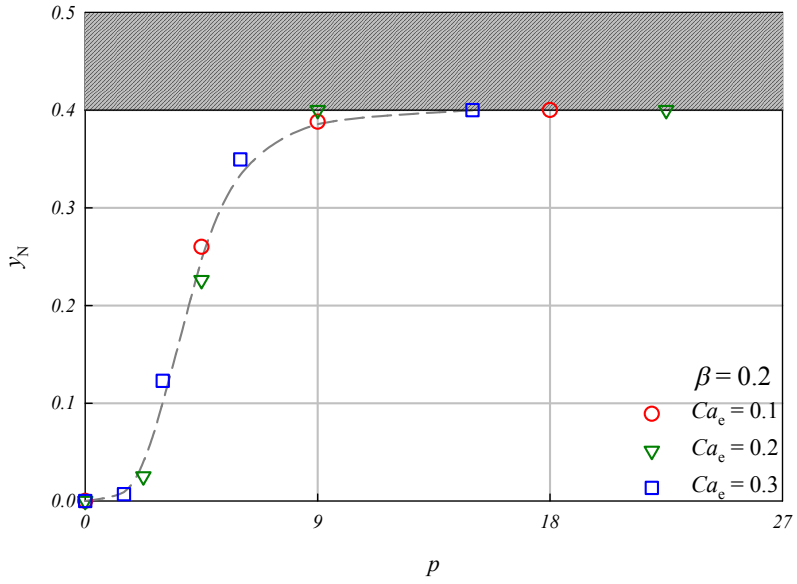

Figure 3.14: Migration of a neo-Hookean particle in a Giesekus fluid under confined shear flow: neutral height in the upper semi-channel y_N as a function of the parameter p for $Ca_e = 0.1$ (red diamonds), 0.2 (green circles), 0.3 (blue squares). The blockage ratio is $\beta = 0.2$. The shaded region represents the portion of the channel not physically accessible by the center of mass of the particle.

3.3 Final remarks

In this chapter, the deformation and cross-streamline migration of an initially spherical neo-Hookean elastic particle suspended in confined shear flow of Newtonian and Giesekus viscoelastic fluids is studied by means of 3D arbitrary Lagrangian Eulerian finite element method numerical simulations.

When suspended in a Newtonian fluid in a symmetric position with respect to the moving walls of the shear flow cell, the particle is found to deform until it attains a steady ellipsoid-like deformed shape, with a fixed orientation with respect to the flow direction. The two dimensionless parameters that govern the phenomenon are the elastic capillary number Ca_{e}, that relates the viscous forces acting on the particle and its elasticity, and the geometric blockage ratio β. The effects of such parameters on the steady deformation and orientation of the channel-mid plane-centered elastic particle are investigated: it is found that both Ca_{e}- and β-increases lead to a more deformed steady shape, and a more pronounced flow-alignment.

If the particle is initially suspended in a Newtonian liquid closer to a wall of the channel than to the other, it migrates transversally to the flow direction towards the center plane of the channel. For any given couple of values of the parameters β and Ca_{e}, a master curve describes the migration velocity trend as a function of the particle vertical position in the gap of the channel, with the migration velocity increasing as the particle is closer to a wall. Out of the center plane of the flow cell, the deformed shape of the particle is found to be asymmetric, with the portion of its surface exposed to the fluid from the side of the wall slightly overcoming the portion of the surface exposed from the side of the center of the channel. Another master curve quantitatively describes such surface imbalance as a function of the particle vertical position over the gap of the channel, for any fixed $\beta - Ca_{\mathrm{e}}$ couple: the surface imbalance is larger as the particle is closer to the wall.

When the elastic particle is suspended in a sheared Giesekus viscoelastic fluid, its steady deformation and orientation angle will depend on β, Ca_{e} and on the new parameter p, which measures the relative weight of the elastic and

viscous forces in the matrix. The effects of such parameters are investigated. In the simple case $\beta = 0$ (unbounded shear), it is found that a Ca_{e}-increase leads to both a more pronounced deformation and flow-alignment of the particle, whereas p contrasts deformation and promotes flow-alignment.

Like in a Newtonian fluid, also in a viscoelastic matrix the particle is found to migrate transversally to the flow direction when initially suspended out of the symmetry plane of the flow cell. Depending now on the value of p, however, the equilibrium position 'attracting' such migration changes. Indeed, low p-s promote migration towards the center plane, whereas high p-s promote migration towards the walls. For p below 10, the competition between the effects of the viscous and the elastic forces acting on the particle results in an equilibrium height in between the center plane and the wall.

Chapter 4

A multi-body problem: numerical simulations of the linear viscoelasticity of monodisperse emulsions of Newtonian drops in a Newtonian fluid from dilute to concentrated regime

4.1 Introduction

In this chapter, we assess the validity of Oldroyd's theory, not only in the case of dilute systems (i.e., for vanishing ϕ), but also for concentrated emulsions (indeed, as mentioned above, Oldroyd's original predictions through his cell model were derived with no limitations on the emulsion concentration ϕ). To do this, we compute the bulk linear viscoelastic properties of monodisperse emulsions of Newtonian drops in a Newtonian matrix are computed by means

of ALE FEM 3D numerical simulations for ϕ up to 0.30, $0.1 \leq \lambda \leq 100.0$, and $0.02 \leq \omega^* \leq 10.0$, where ω^* (see below) is the dimensionless frequency of the oscillatory forcing to which the emulsions are subjected. The case with interfacial slip between the drops and the suspending matrix is also considered in the analysis.

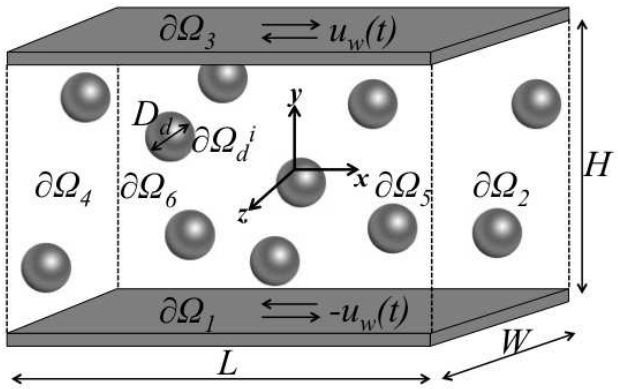

Figure 4.1: Schematic drawing of a monodisperse emulsion of Newtonian drops in a Newtonian matrix undergoing Small Amplitude Oscillatory Shear flow.

In Figure 4.1, a schematic drawing of a monodisperse emulsion of Newtonian drops with diameter D_d in a Newtonian matrix undergoing Small Amplitude Oscillatory Shear (SAOS) flow is reported. Both the dispersed phase and the matrix are assumed to be incompressible and inertialess, so the system can be modeled through the mass and momentum balances for the two phases in the constant density Stokes formulation given in Sections 2.2.1 - 2.2.2.

By extending the analysis of Batchelor [5], the bulk stress $\langle \boldsymbol{\sigma} \rangle$ of an

emulsion accounting for the slip condition is expressed as (see, e.g., [69, 86]):

$$\begin{aligned}\langle\boldsymbol{\sigma}\rangle =& \frac{1}{V}\left[\int_{\mathrm{V}-\sum \mathrm{V}_\mathrm{d}^i} \boldsymbol{\sigma}_\mathrm{m} dV + \sum_i \int_{\mathrm{V}_\mathrm{d}^i} \boldsymbol{\sigma}_\mathrm{d}^i dV\right] + \\ &- \frac{\Gamma}{V}\sum_i \int_{\mathrm{A}_\mathrm{d}^i} \left(\boldsymbol{n}_\mathrm{d}^i \boldsymbol{n}_\mathrm{d}^i - \frac{\boldsymbol{I}}{3}\right) dA + \\ &+ \frac{\eta_\mathrm{m}}{V}\sum_i \int_{\mathrm{A}_\mathrm{d}^i} [(\boldsymbol{u}_\mathrm{d}^i - \boldsymbol{u}_\mathrm{m})\boldsymbol{n}_\mathrm{d}^i + \boldsymbol{n}_\mathrm{d}^i(\boldsymbol{u}_\mathrm{d}^i - \boldsymbol{u}_\mathrm{m})] dA]\end{aligned} \tag{4.1}$$

where V is the volume of the integration domain, $\mathrm{V} - \sum \mathrm{V}_\mathrm{d}^i$ is the volume occupied by the matrix in that domain, V_d^i and A_d^i are the volume and surface area of the i-th drop, respectively. The first contribution in square brackets is the volume-averaged bulk stress, the second term accounts for the interfacial tension, the last term is due to the interfacial slip (that drops out in case of no-slip condition, since $\boldsymbol{u}_\mathrm{d}^i - \boldsymbol{u}_\mathrm{m} = \boldsymbol{0}$, as given by Equation (2.18) for $\alpha = 0$).

In this chapter, the bulk elastic and loss *moduli* of monodisperse emulsions of Newtonian drops in a Newtonian matrix are investigated in the linear regime as a function of the volume fraction of the dispersed phase ϕ, and of the frequency of the forcing wave ω, for various values of the drop-to-matrix viscosity ratio λ and the slip coefficient α. The oscillating solid boundaries of the flow cell (see Equations (2.11) and (2.12)) move according to:

$$u_\mathrm{w}(\omega, t) = \frac{H}{2}\gamma\omega\sin(\omega t) \tag{4.2}$$

where H is the gap between the plates, $\gamma \ll 1$ is the amplitude of the oscillations to which the plates are subjected, and ω is the frequency of such oscillations. To assure that, for a chosen strain amplitude γ, the emulsion response is linear, we verify that, by doubling the strain amplitude, the following relationship holds:

$$\langle\sigma_{xy}(\omega, t)\rangle|_{2\gamma} = 2\langle\sigma_{xy}(\omega, t)\rangle|_{\gamma} \tag{4.3}$$

As the system is in the linear regime, the Fourier analysis of the xy-component of the bulk stress $\langle\sigma_{xy}\rangle$ does not give rise to higher order harmonics. That

means that $\langle \sigma_{xy} \rangle$ can be expressed as:

$$\langle \sigma_{xy}(\omega, t) \rangle = \gamma(G'(\omega)\cos[\omega t] + G''(\omega)\sin[\omega t]) \tag{4.4}$$

where G' is the elastic modulus, and G'' is the loss modulus. Actual computation of $G'(\omega)$, and $G''(\omega)$ of the emulsion is described in detail in the next section.

4.2 Computational approach

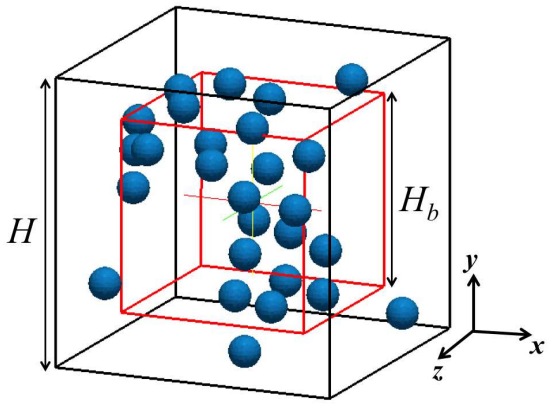

Figure 4.2: Geometry of the computational domain. $\phi = 0.05$.

In Figure 4.2, an example of the computational domain for $\phi = 0.05$ is displayed: monodisperse non-overlapping drops are randomly distributed in a cube with side H, and the upper and lower boundaries of such subdomain (along the y-direction) are solid walls that oscillate according to Equation (4.2).

Given a size of the computational domain, there are of course infinite combinations of the number of drops and their diameter that give a specific

volume fraction ϕ. For a fixed a ϕ-value, we progressively reduce the diameter of the drops D_d (and proportionally increase their number) until the *moduli* in the computational domain do not change anymore. When this condition is satisfied, we consider the system to be an emulsion. For every ϕ, the invariance of the *moduli* is reached when $D_\mathrm{d} \leq 0.167H$, as in [21].

In order to evaluate the bulk elastic and loss *moduli* of an emulsion characterized by certain values of λ and ϕ, and subjected to oscillations at a certain frequency ω, the average stress tensor $\langle \boldsymbol{\sigma} \rangle$ has to be computed in the bulk of the emulsion. By definition of bulk, an issue to be taken into account is avoiding wall effects: the viscoelastic response of the material must become independent of the distance between the walls. To ensure this, the average stress of the system is computed in a cubic subdomain concentric to the whole domain, and with its boundaries at a certain distance from the boundaries of the original 'big' cube (as an example, see the red cube in Figure 4.2). Such subdomain is considered suitable, i.e., free of wall effects, if in it and in a further smaller cube the same viscoelastic properties are computed.

Since the drops are initially randomly distributed in the domain, in principle, during oscillations they may cross the periodic boundaries of the cube; due to the numerical technique adopted, that would make the simulations crash. Since the amplitude of the oscillations can be chosen arbitrarily small, however, we make sure that such scenario is avoided. It should be noticed that this does not prevent the drops from crossing the boundaries of the 'bulky' subdomain where the quantities of interest are computed (see above); following [23, 24], when computing the integrals in Equation (4.1), we include in the integration volume all the drops whose center-of-mass belongs to the subdomain.

To simulate emulsions beyond the dilute regime, a large number of drops needs to be considered, which would enormously increase the computational requirements of our simulations, both in terms of time and memory, until, in correspondence of a critical ϕ-value, such cost would become unsustainable.

However, we find that, as ϕ increases, the bulk properties of emulsions can be effectively calculated even if only the subdomain where the average shear stress is computed is actually filled with drops, the space between it and the boundaries of the whole computational domain being filled with pure matrix.

Let us, now, explain in detail the two main aspects mentioned above: (i) how we guarantee that wall effects are negligible; (ii) how we succeed in reducing the computational cost of our simulations by building up suitable simulation domains (the 'bulky' subdomains alluded to above) containing relatively few drops with respect to the number of drops that would pertain to the complete simulation domain at a given volume fraction. To illustrate those issues, for the sake of simplicity in the exposition, we perform our discussion in 2D. The proposed methodology is general, however, and all the 3D results reported in the following are obtained in the way described here.

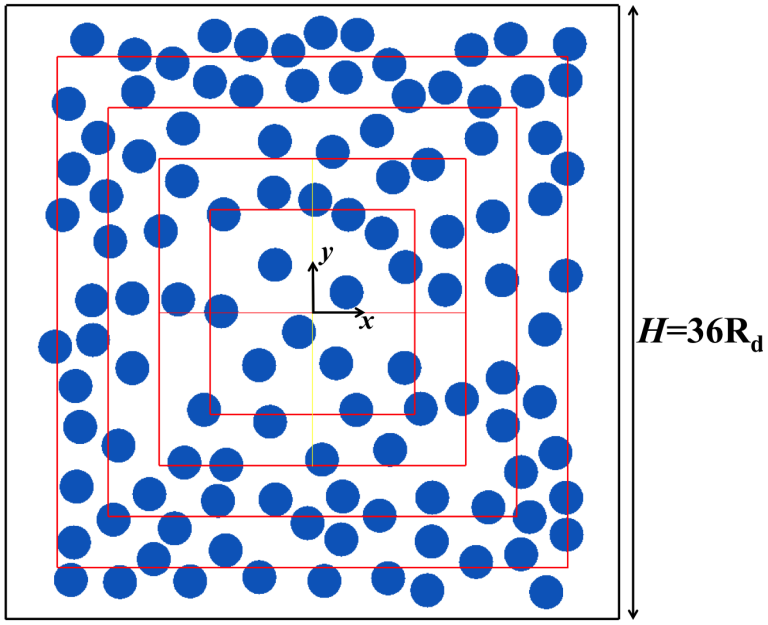

Figure 4.3: Geometry of the 2D computational domain. $\phi = 0.27$.

Let us consider a 2D square cell filled with a Newtonian fluid with monodisperse Newtonian drops with volume fraction $\phi = 0.27$. The viscosity ratio between the drops and the matrix is $\lambda = 2.0$, no slip acts between the drops

and the matrix. The side of the cell is 36 times the initial radius of the drops, and the system is subjected to Small Amplitude Oscillatory Shear flow with frequency $\omega = 0.4$ (made dimensionless as explained in Section 4.3). In Figure 4.3, a scheme of such domain in its initial configuration is reported, where the distribution of the drops is random. The upper and lower sides of the square are solid walls that move according to Equation (4.2). Due to computational reasons, in the generation of the random initial positions of the drops, the constraint is added that they cannot cross the vertical boundaries of the flowcell. If we look at a series of concentric square subcells characterized by a progressively smaller side (the red squares in Figure 4.3), the initial volume fraction of the drops in those changes with the side of the subdomain we take into account, since the overall initial distribution of the drops is random. Moreover, whereas ϕ is constant in time in the 'big' domain (the drops cannot cross the vertical boundaries of the flowcell), it can vary in the 'red' subdomains, since the drops can cross the red sides during oscillations.

In Figure 4.4, the time-averaged volume fraction of the drops is reported *vs.* the side of the subdomain in which it is computed, made dimensionless by the radius of the drops R_d, for an overall volume fraction $\phi = 0.27$, $\lambda = 2.0$, $\omega = 0.4$. Each point in the diagram is in turn the average of the results obtained for ten different random initial distributions of the drops. By looking at Figure 4.4, it can be seen that by progressively decreasing the side of the subdomain (i.e., by going left along the H/R_d-axis), ϕ initially increases: this is due to the fact that not all the room in the very external region of the original computational domain is really available to the drops, since, as hinted above, the drops must not cross the vertical boundaries of the flowcell; then, for H/R_d in the range $18 - 24$, the average volume fraction in the red box recovers the imposed value, as highlighted by the dashed horizontal line.

For each configuration of the drops, the average shear rate and shear stress are computed in all the considered subdomains. From those data, the viscoelastic *moduli* of the system are obtained and can be plotted as a

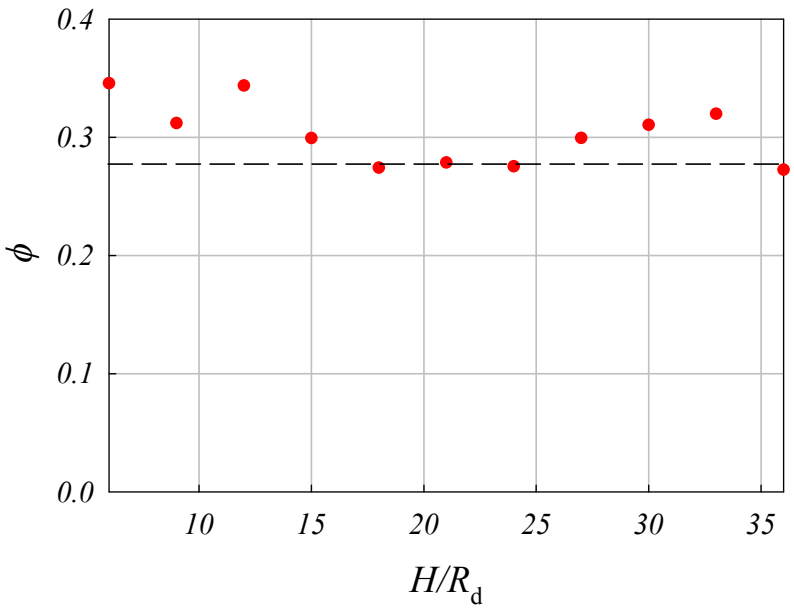

Figure 4.4: Average volume fraction of the drops ϕ in a subdomain of the 2D computational domain as a function of the dimensionless side of the subdomain H/R_{d}.

function of the side of the red box. This is done for the elastic modulus G' in Figure 4.5 (G' having been made dimensionless as written in Section **??**). It is evident from Figure 4.5 that G' changes with the side of the subdomain in which it is computed. If one looks at the range $H/R_{\mathrm{d}} = 18-24$, where ϕ does not change with H/R_{d} and is equal to the imposed one (as we have seen in Figure 4.4), it can be noticed that G' is also constant with H/R_{d} in there. The same behavior is also noticed for the loss modulus G'' (not shown). From such observations, it can be deduced that a subdomain with a side in the range 18 - 24 is in fact representative of the bulk of the emulsion. In addition, it can be observed that the G'-value computed for $H/R_{\mathrm{d}} = 36$ (the whole domain, including the solid walls) also overlaps the values computed in the boxes with $H/R_{\mathrm{d}} \in [18, 24]$, thus letting us conclude that for the considered overall volume fraction, the size of the whole computational domain is large enough

to make wall effects irrelevant in the calculation of the elastic modulus. For G'' similar results are obtained, and analogous conclusions can be drawn.

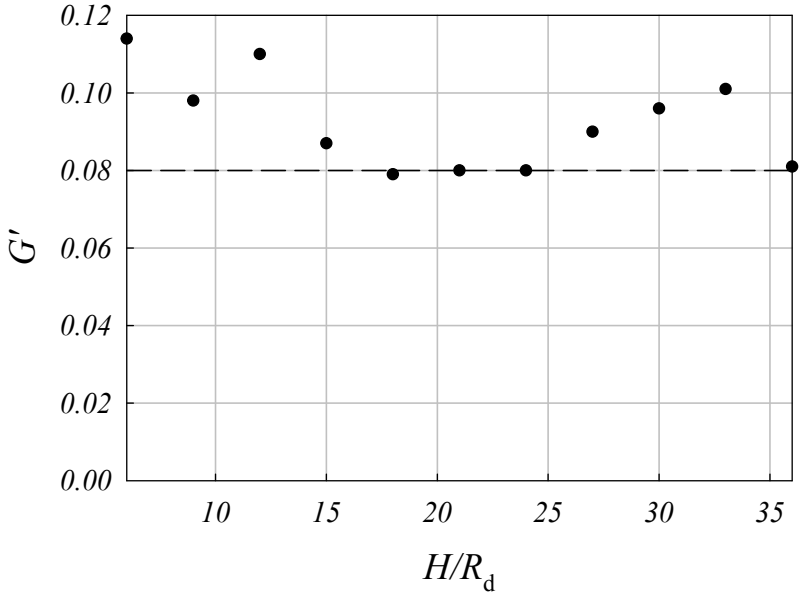

Figure 4.5: Elastic modulus G' in a subdomain of the 2D computational domain as a function of the dimensionless side of the subdomain H/R_{d}. Overall volume fraction $\phi = 0.27$

In view of developing a procedure for computational saving, let us now take the same ten random distributions of the drops from which the results in Figures 4.4-4.5 are computed, and, from each one, remove all the drops whose centers initially lie outside a square with side $H/R_{\mathrm{d}} = 24$, and replace them with pure matrix. With reference to the configuration shown in Figure 4.3, the result of such procedure is displayed in Figure 4.6. If we consider a sequence of concentric square subcells of decreasing side with $18 \leq H/R_{\mathrm{d}} \leq 24$ (e.g. the green squares in Figure 4.6), the volume fraction of the drops in each of those (averaged over time and different initial configurations) is of course the same as in the subdomains characterized by the same side with the system fully filled with drops. The choice of considering such interval

stems from the result that in a box whose side belongs to that range the volume fraction of the system is the imposed one, and the *moduli* are the 'bulky' ones.

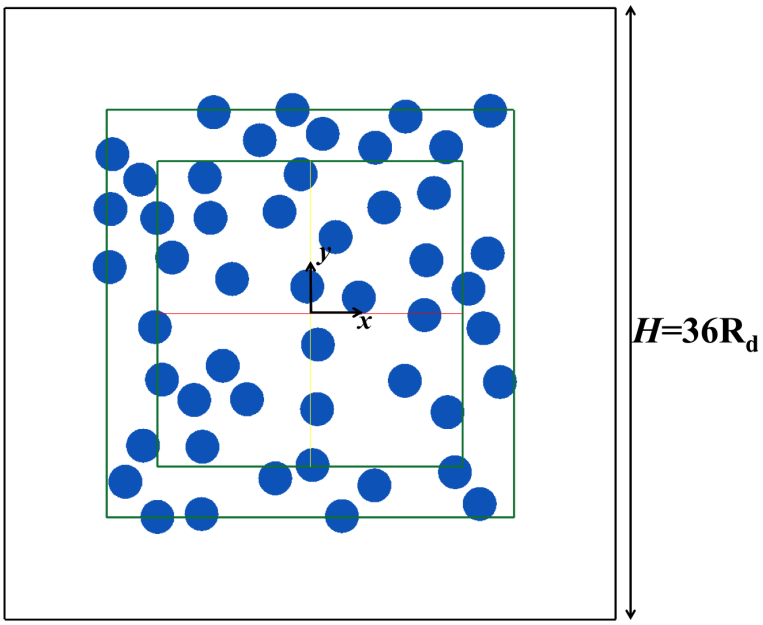

Figure 4.6: Geometry of the 2D computational domain with an empty frame. $\phi = 0.27$.

For such 'peculiar' emulsions, the *moduli* can be computed at varying H/R_{d} between 18 and 24, as done above. If we compute, then, the per cent distance between the G'-values in the full and the 'framed' system for the same side of the subdomain, as $\epsilon = 100|\frac{G'_{\mathrm{full}} - G'_{\mathrm{frame}}}{G'_{\mathrm{full}}}|$, we find that such discrepancy is always below 2.5%. This lets us argue that removing the drops in the space between the boundaries of the box with $H/R_{\mathrm{d}} = 24$ (where the 'bulky' conditions are verified), and the boundaries of the whole domain makes us commit a small error, but lets us 'save' about 55% of the drops.

We consider now a 2D square domain filled with a dilute emulsion of Newtonian drops in a Newtonian fluid (volume fraction $\phi = 0.07$), with viscosity ratio $\lambda = 2.0$, and subjected to SAOS flow with $\omega = 0.4$. The side of the cell is 60 times the initial radius of the drops. In Figure 4.7, a scheme

of such domain in its initial configuration is reported, where the distribution of the drops is random. As in the case with $\phi = 0.27$ shown in Figure 4.3, in the generation of the random initial positions of the drops, the constraint is added that they cannot cross the vertical boundaries of the flowcell.

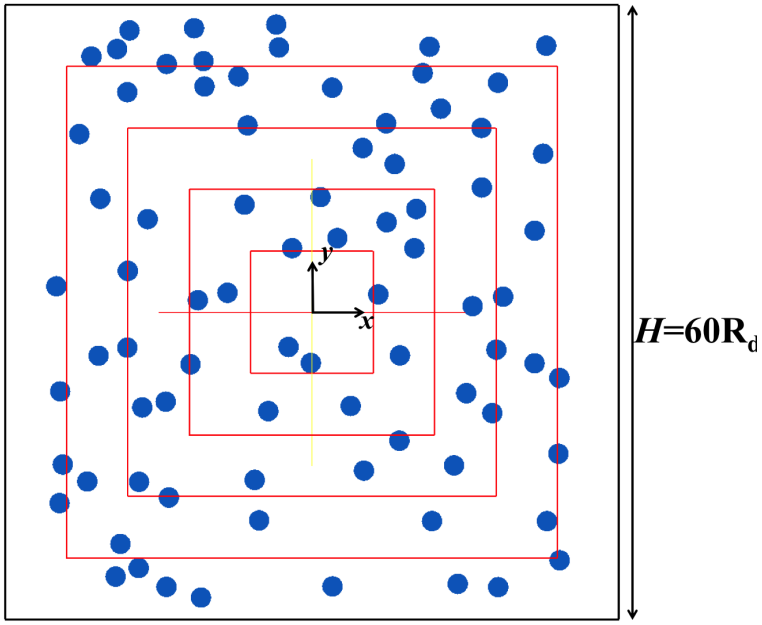

Figure 4.7: Geometry of the 2D computational domain. $\phi = 0.07$.

As we did above, we take into account several concentric square subcells with a progressively decreasing side (the red squares in Figure 4.7), and compute the average over ten random initial configurations of the time-averaged volume fraction of the drops in those subdomains. The results of such calculations are shown in Figure 4.8. As the side of the subdomain is progressively decreased from $H/R_\mathrm{d} = 60$, ϕ initially increases due to the fact that not all the room in the very external region of the computational domain is really available to the drops because of the constraint that the drops cannot cross the vertical boundaries of the flowcell; then, for H/R_d between 24 and 30, the average volume fraction is constant and equal to the imposed value $\phi = 0.07$, as highlighted by the dashed horizontal line.

The average shear rate and shear stress are computed in all the consid-

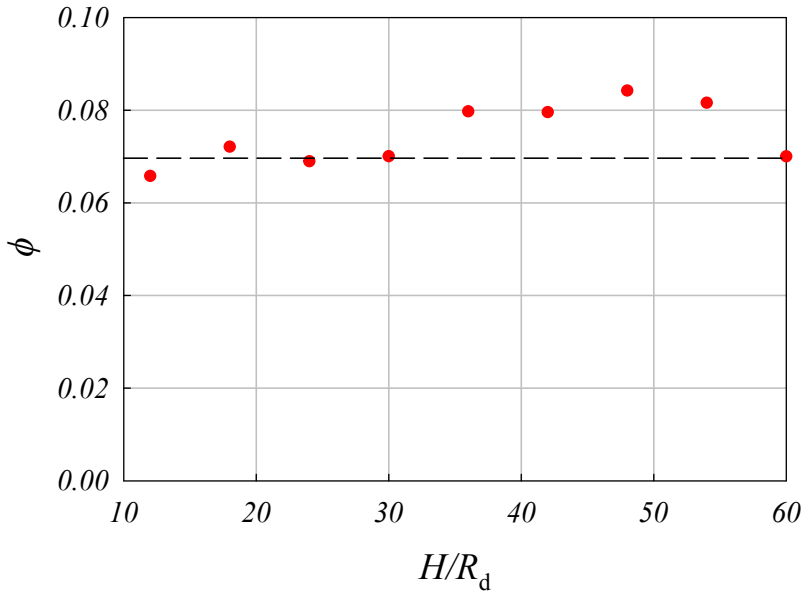

Figure 4.8: Average volume fraction of the drops ϕ in a subdomain of the 2D computational domain as a function of the dimensionless side of the subdomain H/R_d.

ered boxes, from which the viscoelastic *moduli* of the system are obtained as a function of the side of the box. The plot of G' *vs.* H/R_d for $\phi = 0.07$ is displayed Figure 4.9. As for $\phi = 0.27$ (Figure 4.5), the elastic modulus changes with the side of the subdomain in which it is computed. Where ϕ does not change and is equal to the imposed one ($H/R_d \in [24, 30]$), G' does not change as well, thus letting us deduce that a subdomain with dimensionless side in the range 24 - 30 is representative of the bulk of the emulsion. In addition, in analogy to what happens for $\phi = 0.27$, the G'-value computed when taking the whole domain, including the solid walls, also overlaps the values computed in the boxes with $H/R_d \in [24, 30]$, so also for $\phi = 0.07$ the size of the whole computational domain we have chosen is large enough to make wall effects irrelevant in the calculation of the viscoelastic properties.

In analogy to what we did for $\phi = 0.27$, we take the ten random distribu-

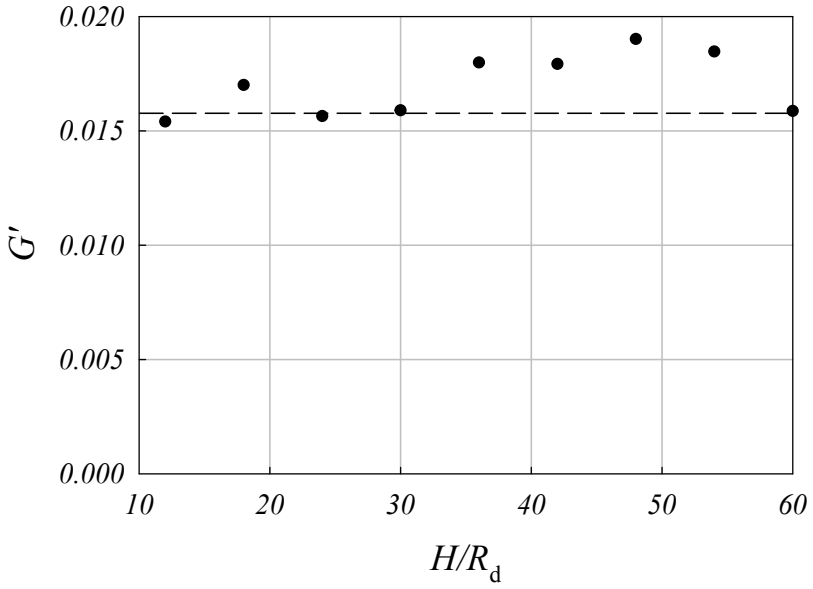

Figure 4.9: Elastic modulus G' in a subdomain of the 2D computational domain as a function of the dimensionless side of the subdomain H/R_{d}. Overall volume fraction $\phi = 0.07$.

tions of the drops we generated with an overall volume fraction $\phi = 0.07$, and we remove from each of them all the drops whose centers initially lie outside a square with side $H/R_{\mathrm{d}} = 30$, replacing them with pure matrix. Then, we compute the *moduli* of the system with an empty frame at varying H/R_{d} between 24 and 30. In that range, the per cent distance between the G'-values in the full and the framed system is between 3.5 and 7%. This makes us conclude that, if we want to compute the viscoelastic *moduli* in the box with $H/R_{\mathrm{d}} = 30$, where we have found that the 'bulky' conditions are verified, removing the drops in the space between the boundaries of such subcell and the boundaries of the domain would let us realize a computational saving, but make us commit a non-negligible error.

By comparing the results at $\phi = 0.27$ and $\phi = 0.07$, we can infer that there is a screening effect among the drops. Indeed, we see that at low volume fractions (e.g. $\phi = 0.07$), the absence of drops outside the subdomain

where we compute the viscoelastic properties of the system has a considerable influence on the calculated values, whereas, at high volume fractions (e.g. $\phi = 0.27$), the difference between the results calculated in the full and the framed system is almost negligible. From such observation, we can conclude that, in 2D, at low ϕ-values the complete system must be simulated, whereas, at high volume fractions, it is allowed to simulate a system where only the region in which the *moduli* are computed is filled with drops, without losing the representativity of the real system.

In 3D, however, the situation is even more favorable, since the hydrodynamic interactions among the suspended objects decay much faster (in space) than in 2D. Indeed, we find that, for $\phi = 0.05$, the per cent discrepancy between the G'-values computed in a 'bulky' subdomain of a cell fully filled with drops, and the corresponding value computed in a subdomain surrounded by pure matrix is less than 3%. Hence, we simulate full systems for volume fractions below 0.05; above such value, the frame approach is used. For $\phi = 0.05$, such criterion will lead to a reduction of the number of drops of about 70%; for $\phi = 0.2$, the reduction is of 87.5%. So for $\phi \geq 0.05$, we run simulations where only the portion of the flow cell where the stress is computed is filled with drops.

Given a forcing wave on the moving boundaries of the flow cell as expressed in Equation (4.2), the wall shear rate of the system is:

$$\dot{\gamma}_{\mathrm{w}}(\omega, t) \equiv \frac{u_{\mathrm{w}}}{H/2} \tag{4.5}$$

It should be emphasized that in a 'bulky' subdomain, e.g. the red box in Figure 4.2, the average of the local shear rate $\sqrt{2\boldsymbol{D} : \boldsymbol{D}}$ is, in general, different from the imposed wave (Equation (4.5)), but, due to linearity, it has the same frequency. So it can be written as follows:

$$\dot{\gamma}_{\mathrm{eff}}(\omega, t) = \gamma_{\mathrm{eff}}\omega \sin[\omega t + \theta] \tag{4.6}$$

As another consequence of linearity, the average stress in the red box can be

expressed as:

$$\begin{aligned}\langle\sigma_{xy,\mathrm{eff}}(\omega,t)\rangle =&\gamma_{\mathrm{eff}}(G'(\omega)\cos[\omega t+\theta]+\\ &+G''(\omega)\sin[\omega t+\theta])\end{aligned} \tag{4.7}$$

From Equations (4.6) and (4.7), which are written for the 'bulky' subdomain, we can, then, compute the elastic and viscous *moduli* of the emulsion from the simulation results.

Finally, it is worth specifying that single values of G' and G'' corresponding to a certain random initial spatial distribution of the drops cannot be considered as representative of the *moduli* of an emulsion because there is an influence of the initial configuration on the above mentioned values: for each set of parameters, we consider 5 different initial distributions of the drops, then G'- and G''-values are averaged, and standard deviation is computed.

The consistence of the numerical results presented in Section 4.3 is ensured by the preliminary performance of convergence tests on time-step and mesh resolution. This means that the influence of the variation of the time-step and of the mesh resolution on the simulation results is studied, and that time-step and mesh resolution are chosen so as to guarantee invariance of the physical results upon further refinements. Time and mesh convergence have been checked for all the calculations presented in this work. In this section, the results of convergence tests for $\phi = 0.05$ are reported as an example to show the sensitivity of the numerical results to time-step size and mesh resolution.

In Figure 4.10, a mesh is reported for a system characterized by a 5% volume fraction of the drops. In this work, due to the presence of numerous curvilinear surfaces, non-structured meshes with tetrahedral elements are employed. The generation of the computational grids is performed by *gmsh* [38]. Notice that the drops only lie in the 'core' of the computational domain, the reasons having been explained in Section 4.2. The resolution of the elements near the external boundaries of the domain has not a significant influence on the results, since near there only pure matrix is present. On the contrary, the resolution of the elements in the region filled with drops is

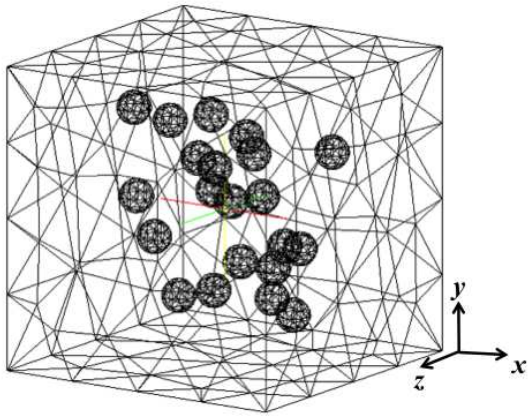

Figure 4.10: Mesh of the computational domain for $\phi = 0.05$. The dimensionless side of the triangles mapping the surface of the drops is $\Delta x^* = \frac{2\pi}{16}$. For visibility reasons, only the surface elements on the boundaries of the drops and of the computational domain are displayed.

crucial (in Figure 4.10, the dimensionless side of the triangles that map the initially spherical surface of the drops, defined as $\Delta x^* = \frac{\Delta x}{R_\mathrm{d}}$, with R_d the initial drop radius, is $\Delta x^* = \frac{2\pi}{16}$, see below).

Convergence test are performed by computing the time evolution of the xy-component of the emulsion stress tensor $\langle \sigma_{xy} \rangle$ at changing mesh resolution and time-step. As an example, the results of such tests for $\phi = 0.05$, $\lambda = 1.0$, $\gamma = 0.025$, $\omega^* = 0.4$, and no-slip are described in the following (frequency is here made dimensionless, as indicated by the superscript *, through $\widetilde{\omega} = \frac{\Gamma}{\eta_\mathrm{m} R_\mathrm{d}}$, see next section).

The stress trends obtained for a side of the elements on the surface of the drops $\Delta x^* = \frac{2\pi}{16}$, and for three different values of the dimensionless time-step ($\Delta t^* = \frac{2\pi}{150\omega^*}, \frac{2\pi}{300\omega^*}, \frac{2\pi}{600\omega^*}$, respectively) are compared: it emerges that by refining the time-step from $\Delta t^* = \frac{2\pi}{150\omega^*}$ to $\Delta t^* = \frac{2\pi}{300\omega^*}$, no quantitative change in the results happens, the discrepancy being at most of order 0.001%.

Of course, no differences arise between the trends for $\Delta t^* = \frac{2\pi}{300\omega^*}$, and $\Delta t^* = \frac{2\pi}{600\omega^*}$. Time convergence is, then, achieved with $\Delta t^* = \frac{2\pi}{150\omega^*}$.

Having fixed $\Delta t^* = \frac{2\pi}{150\omega^*}$, the stress trends are computed for three different mesh resolutions, where the length of the side of the triangles that discretize the surface of the drops is progressively decreased, the values being $\Delta x^* = \frac{2\pi}{8}, \frac{2\pi}{12}, \frac{2\pi}{16}$. The results obtained for such resolutions are compared: by refining the mesh from the coarsest to the medium, there is no quantitative change in the results (as above, the discrepancy is at most of order 0.001%), so mesh convergence is achieved with a length of the elements on the surface of the drops $\Delta x^* = \frac{2\pi}{8}$. The fact that for a size $\Delta x^* = \frac{2\pi}{8}$ mesh convergence is already achieved confirms the validity of the preliminary choice of the size $\Delta x^* = \frac{2\pi}{16}$ for the time convergence test.

In the end, we can conclude that for $\phi = 0.05$, $\lambda = 1.0$, $\gamma = 0.025$, $\omega^* = 0.4$, and no-slip, $\Delta t^* = \frac{2\pi}{150\omega^*}$ and a size of the triangles that map the surface of the drops $\Delta x^* = \frac{2\pi}{8}$ (which implies that each of these surfaces is covered with 66 nodes) ensure the convergence of the numerical results both in time and space. Such values are, then, adopted for obtaining the results at $\phi = 0.05$ shown in what follows. It is worth to precise, however, that as ϕ increases, a refinement of the mesh is necessary, whereas as ω decreases, a refinement of the time-step is needed. In the worst case, i.e. for $\phi = 0.28$ and $\omega^* = 0.02$, we use $\Delta x^* = \frac{2\pi}{16}$ and $\Delta t^* = \frac{2\pi}{6280\omega^*}$. The eventual presence of interfacial slip between the drops and the matrix has no effects on such convergence results.

The simulations have been run on blades with two hexa-core processors Intel Xeon E5649@2.53GHz and 48 GB of RAM. The computational time ranges from a few hours to 2-3 days, depending on the volume fraction of the system under investigation.

4.3 Results and discussion

In this section, the results of our numerical simulations are presented and compared with the theoretical predictions by Oldroyd for $0 < \phi < 0.3$, $\lambda = 0.1, 0.5, 1.0, 5.0, 100.0$, $0.02 \leq \omega^* \leq 10.0$, and $\alpha^* = 0, 0.1, 1.0$, with α^* the dimensionless slip parameter.

Following [86] and [85], the results to be presented in the following are made dimensionless by using $\widetilde{\omega} = \frac{\Gamma}{\eta_{\mathrm{m}} R_{\mathrm{d}}}$ as the characteristic frequency (see previous section). The capillary number $Ca = \frac{\eta_{\mathrm{m}} \gamma \omega R_{\mathrm{d}}}{\Gamma}$, which is the ratio between the viscous and the interfacial forces to which the drops are subjected, can, then, be expressed as $Ca = \frac{\gamma \omega}{\widetilde{\omega}}$, and hence is a measure of the 'strength' of the imposed flow. In the linear regime, it must be verified that $Ca \ll 1$. Since the elasticity of a Newtonian/Newtonian emulsion is wholly due to interfacial contributions (see, for example, [63]), we choose to make the elastic modulus G' dimensionless through $\frac{\Gamma}{R_{\mathrm{d}}}$, whereas the loss modulus G'' is made dimensionless through the loss modulus of the suspending fluid $G''_{\mathrm{m}} = \eta_{\mathrm{m}} \omega$ at the same frequency. The slip coefficient α of Equation (2.18) is made dimensionless through $\frac{R_{\mathrm{d}}}{\eta_{\mathrm{m}}}$. For the sake of clarity, in what follows the superscript * denoting dimensionless quantities will be always omitted.

4.3.1 The no-slip case

In Figures 4.11-4.15, results at low frequency are presented; a value of 0.4 times the characteristic frequency is chosen (the study of the effects of frequency on the viscoelastic *moduli* is shown in Figures 4.16-4.18). The dimensionless elastic modulus G' (upper panel) and loss modulus G'' (lower panel) are shown as a function of ϕ at various λ-s for the no-slip case. In these figures, our data are displayed as black circles with error bars. Each datum represents the average of the results of 5 simulations having different random initial positions of the drops at the same ϕ, and with fixed ω and λ. Oldroyd's predictions are shown as blue solid curves. The analytical expressions of $G'(\lambda, \phi, \omega)$ and $G''(\lambda, \phi, \omega)$ derived from [78] in the no-slip case are

reported explicitly in Appendix A.

In Figure 4.11, the trends of $G'(\omega = 0.4)$ and $G''(\omega = 0.4)$ as a function of ϕ are reported for $\lambda = 0.1$. It clearly emerges from panel (a) that the values of the elastic modulus G' obtained through simulations are in excellent quantitative agreement with Oldroyd's predictions in the whole range of ϕ-values explored. This is also found for G'' (panel (b)).

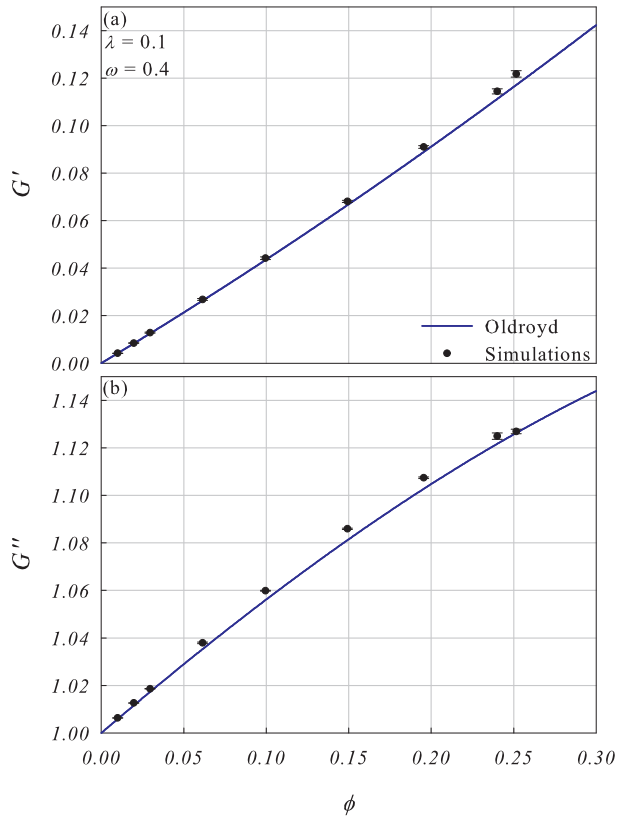

Figure 4.11: Elastic modulus G' (a) and loss modulus G'' (b) as a function of volume fraction ϕ for an emulsion of Newtonian drops in a Newtonian matrix in the linear regime. Blue curves: theoretical predictions from [78]. The viscosity ratio is chosen as $\lambda = 0.1$, the frequency is $\omega = 0.4$, there is no interfacial slip between the suspended drops and the matrix.

For $\lambda = 0.5$, the very same conclusions can be drawn as for $\lambda = 0.1$ (see Figure 4.12). Oldroyd's predictions for G' (Figure 4.12a) are quantitatively

reproduced by our numerical simulations in the whole ϕ-range explored (the discrepancies between theory and simulations are always within 5%); so it is also for G'' (Figure 4.12b).

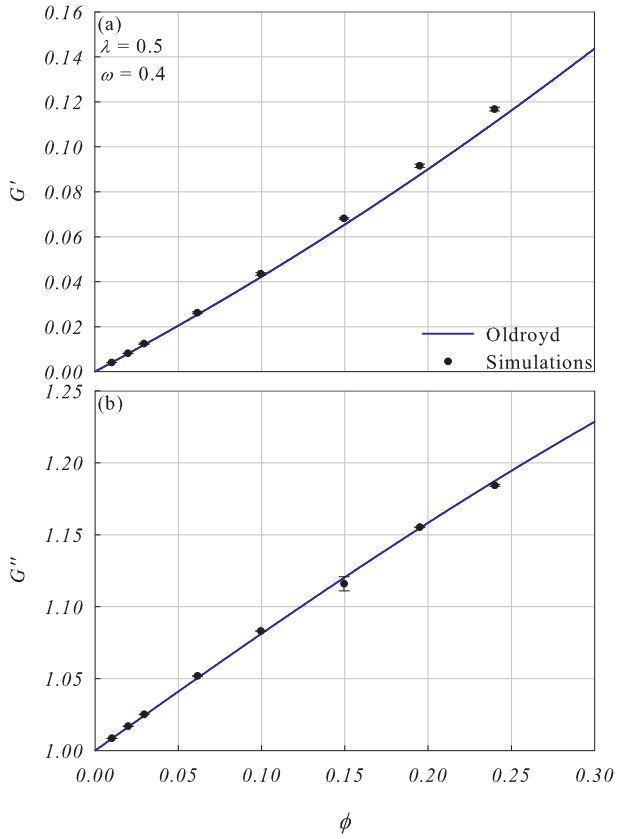

Figure 4.12: Elastic modulus G' (a) and loss modulus G'' (b) as a function of volume fraction ϕ for an emulsion of Newtonian drops in a Newtonian matrix in the linear regime. Blue curves: theoretical predictions from [78]. The viscosity ratio is chosen as $\lambda = 0.5$, the frequency is $\omega = 0.4$, there is no interfacial slip between the suspended drops and the matrix.

Figure 4.13a shows that when λ is equal to 1.0, numerical predictions for G' almost overlap Oldroyd's theoretical curve except for the largest volume fraction $\phi = 0.28$, where the numerical result overtakes the theoretical one of about 17%. Figure 4.13b shows that for G'' there is a very good agreement between the computational points and Oldroyd's predictions over all the ϕ-

range investigated.

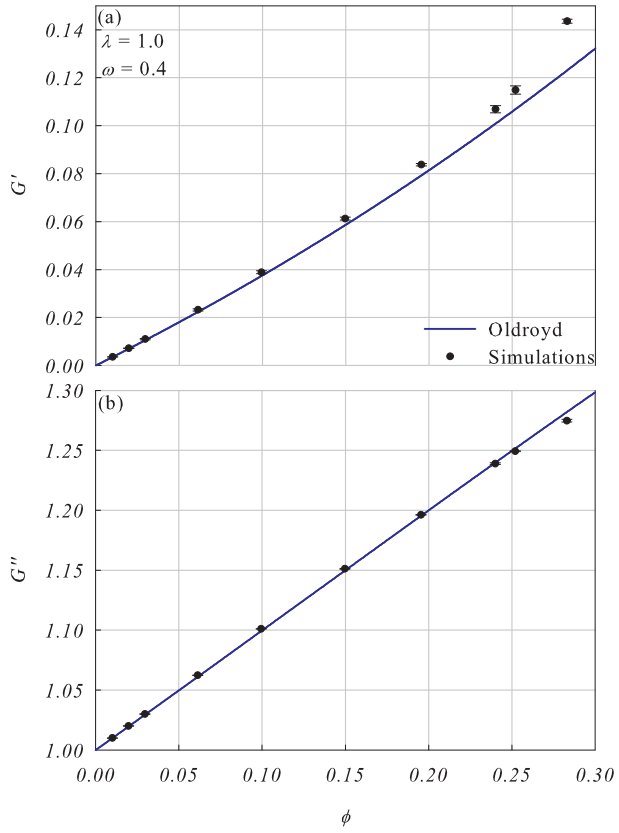

Figure 4.13: Elastic modulus G' (a) and loss modulus G'' (b) as a function of volume fraction ϕ for an emulsion of Newtonian drops in a Newtonian matrix in the linear regime. Blue curves: theoretical predictions from [78]. The viscosity ratio is chosen as $\lambda = 1.0$, the frequency is $\omega = 0.4$, there is no interfacial slip between the suspended drops and the matrix.

Figure 4.14 reports the comparison between the numerical and the theoretical results for $\lambda = 5.0$. In panel (a), it can be seen that our simulations have the same qualitative G'-trend as Oldroyd's predictions, but, beyond the dilute regime, the computational results lie above the theoretical ones, and the deviations are larger as the volume fraction is increased: the maximum difference is of about 25% for $\phi = 0.28$. The same is observed for G'' (see Figure 4.14b), where for $\phi = 0.28$ the computational point overtakes Oldroyd's

prediction of 5%.

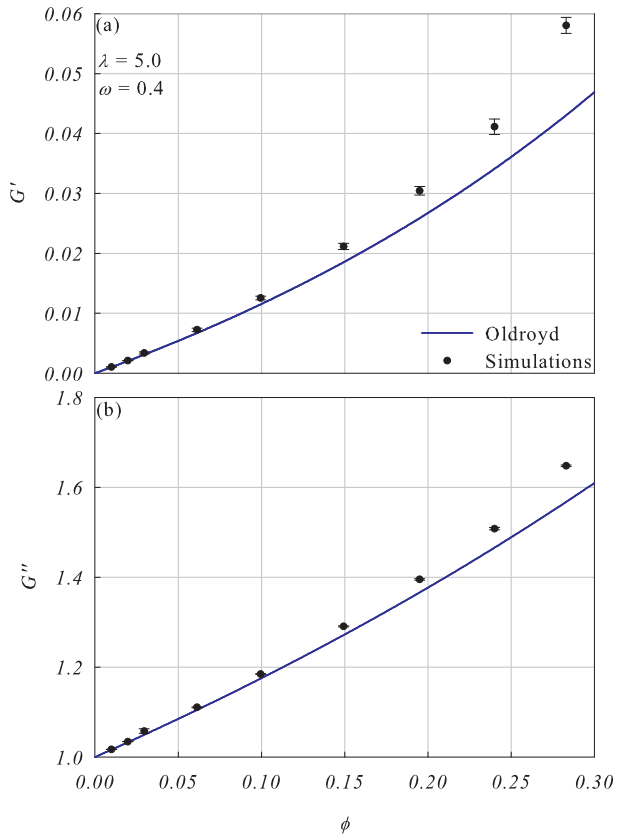

Figure 4.14: Elastic modulus G' (a) and loss modulus G'' (b) as a function of volume fraction ϕ for an emulsion of Newtonian drops in a Newtonian matrix in the linear regime. Blue curves: theoretical predictions from [78]. The viscosity ratio is chosen as $\lambda = 5.0$, the frequency is $\omega = 0.4$, there is no interfacial slip between the suspended drops and the matrix.

Finally, in Figure 4.15, the computational results for the 'extreme' condition $\lambda = 100.0$ are shown. In panel (a), G' is considered: although the numerical points show a trend qualitatively similar to Oldroyd's predictions, no quantitative agreement is found. It should be noticed that the error bars of the black points are quite wide, the reason being that the very high viscosity of the drops compared to the matrix contrasts their deformation, i.e., the system tends to behave like an hard-sphere suspension and, as such, is

characterized by very low G'-values, that are hardly computable within the numerical accuracy.

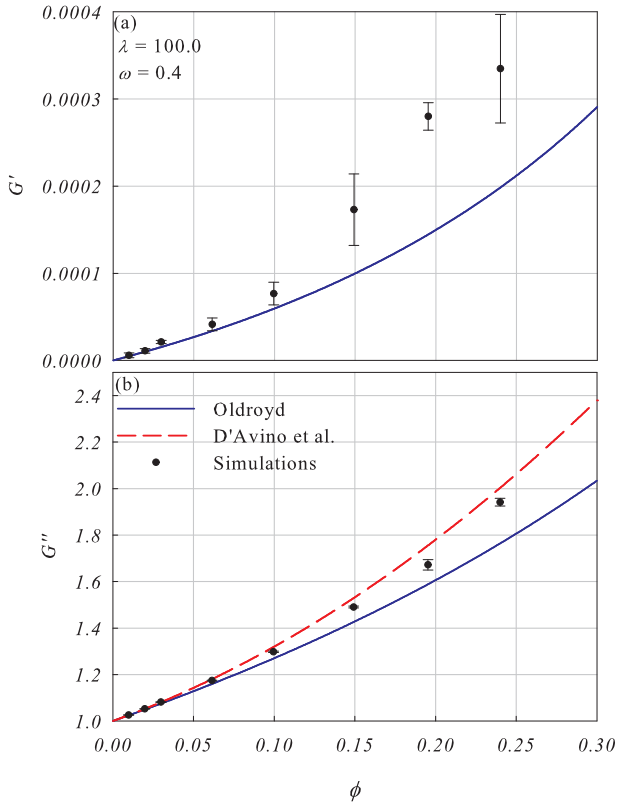

Figure 4.15: Elastic modulus G' (a) and loss modulus G'' (b) as a function of volume fraction ϕ for an emulsion of Newtonian drops in a Newtonian matrix in the linear regime. Blue solid curves: theoretical predictions from [78], red dashed curve in panel (b): numerical predictions for a suspension of rigid spheres in a Newtonian liquid in the linear regime from [21]. The viscosity ratio is chosen as $\lambda = 100.0$, the frequency is $\omega = 0.4$, there is no interfacial slip between the suspended drops and the matrix.

In panel (b), G'' is displayed. In addition to the Oldroyd's predictions, we report with the red dashed curve the numerical predictions of the loss modulus of a monodisperse suspension of hard spheres in a Newtonian fluid as a function of ϕ given in [21]. One can observe that the computed values of G'' do not agree with Oldroyd's theoretical predictions; on the other hand, our numerical results almost quantitatively agree with [21], i.e., with the results

for hard-sphere suspensions, the highest discrepancy in the explored ϕ-range being of about 4.5%. As remarked above, the latter result is expected, as an hard-sphere suspension can be thought of as the asymptotic case of an emulsion with infinite viscosity ratio λ. This evidence confirms the comment by Oldroyd's on his own theory on the limitation to small λ-values.

In Figures 4.16-4.18, the elastic modulus G' (upper panel) and loss modulus G'' (lower panel) are shown as a function of ω for $\phi = 0.10, 0.20, 0.26$, at various λ-s, for the no-slip case. As in Figures 4.11-4.15, Oldroyd's predictions are shown as blue curves. As it is also evident from the graphs, the frequency range is chosen in such a way that, according to Oldroyd's model, invariance of the *moduli* is obtained at the borders of the interval if ω is further decreased or increased. It is worth remarking that the decrease of G'' with frequency shown in Figures 4.16-4.18, which could appear in disagreement with the well known trends for emulsions (see, for example, [41]), depends on the characteristic G''-value used in non-dimensionalization $G''_{\mathrm{m}} = \eta_{\mathrm{m}}\omega$ (see above). In other words, our decrease means a less-than-linear increase of G'' with ω.

In Figure 4.16, the trends of G' and G'' as a function of ω are reported for $\lambda = 0.1$, and for $\phi = 0.10, 0.20, 0.26$. From panel (a), it emerges that for $\phi = 0.10$, there is a strong quantitative agreement on G' between the numerical simulations (the grey circles) and Oldroyd's predictions (the blue solid line) over the whole range of frequency investigated, i.e. for $0.02 \leq \omega \leq 10$. As the volume fraction increases to $\phi = 0.20$, and, then, to $\phi = 0.26$, the quantitative agreement between the numerical data (the grey diamonds and triangles) and Oldroyd's predictions (the blue dashed and dash-dot lines) still holds over the whole frequency-range. Figure 4.16b compares numerical and theoretical G''-*vs.*-ω trends. It is interesting to notice that Oldroyd predicts the curves obtained at different ϕ-s to reciprocally intersect, G'' increasing with ϕ at low ω-s and decreasing with it at high ω-s. Numerical data (the symbols being the same as in panel (a)) qualitatively confirm Oldroyd's predictions, the agreement being strongly quantitative over the whole range of frequencies

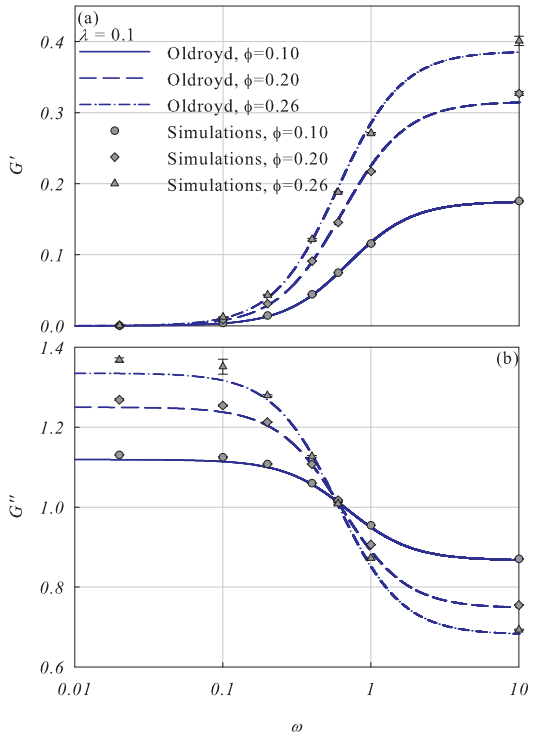

Figure 4.16: Elastic modulus G' (a) and loss modulus G'' (b) as a function of frequency ω, and for three values of the volume fraction ϕ, for an emulsion of Newtonian drops in a Newtonian matrix in the linear regime. Blue curves: theoretical predictions from [78]. There is no interfacial slip between the suspended drops and the matrix, the viscosity ratio is chosen as $\lambda = 0.1$, ω-axis is log-scale.

considered for $\phi = 0.10$ and 0.20.

In Figure 4.17, the elastic and loss *moduli* as a function of the frequency are shown for $\lambda = 1.0$, and $\phi = 0.10, 0.20, 0.26$. In Figure 4.17a, it can be seen that, as for $\lambda = 0.1$, there is an excellent quantitative agreement between numerical simulations and Oldroyd's theoretical curve (the blue solid line) in the whole range of frequencies considered as the volume fraction is equal to 0.10. As ϕ increases, such agreement is still qualitatively verified, but slight quantitative discrepancies arise at high frequencies, as it emerges by looking at the distances between the grey diamonds and the blue dashed line ($\phi = 0.20$), and between the grey triangles and the blue dash-dot line

($\phi = 0.26$) for $\omega = 1.0, 10.0$. In Figure 4.17b, it is shown that according to simulation data, at low ω-s G'' increases with ϕ, then, as the frequency increases, the trends at different volume fractions tend to collapse to same value of the loss modulus, such value being 1.0. This behavior fits quantitatively with Oldroyd's predictions for $\phi = 0.10$. As ϕ increases, slight discrepancies appear between numerical data and Oldroyd's theory at low frequencies.

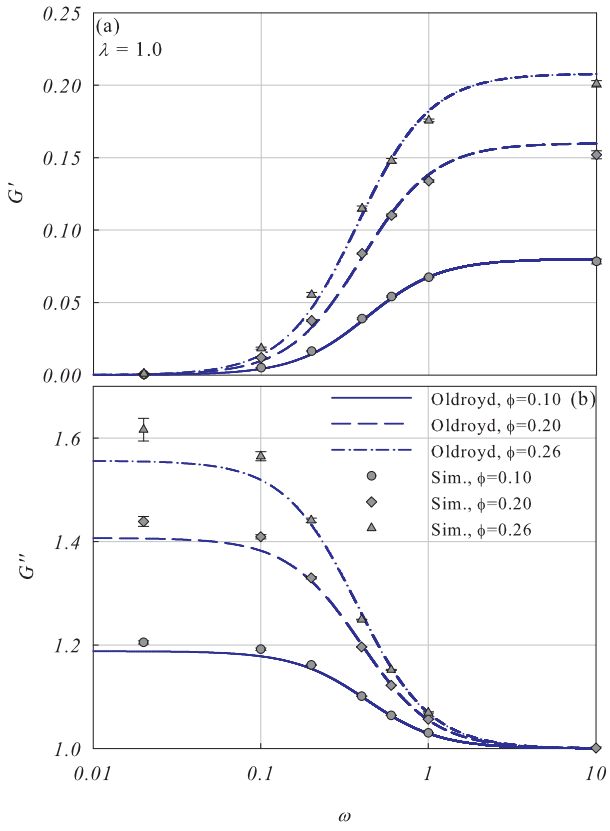

Figure 4.17: Elastic modulus G' (a) and loss modulus G'' (b) as a function of frequency ω, and for three values of the volume fraction ϕ, for an emulsion of Newtonian drops in a Newtonian matrix in the linear regime. Blue curves: theoretical predictions from [78]. There is no interfacial slip between the suspended drops and the matrix, the viscosity ratio is chosen as $\lambda = 1.0$, ω-axis is log-scale.

Figure 4.18 reports the comparison between the numerical and the the-

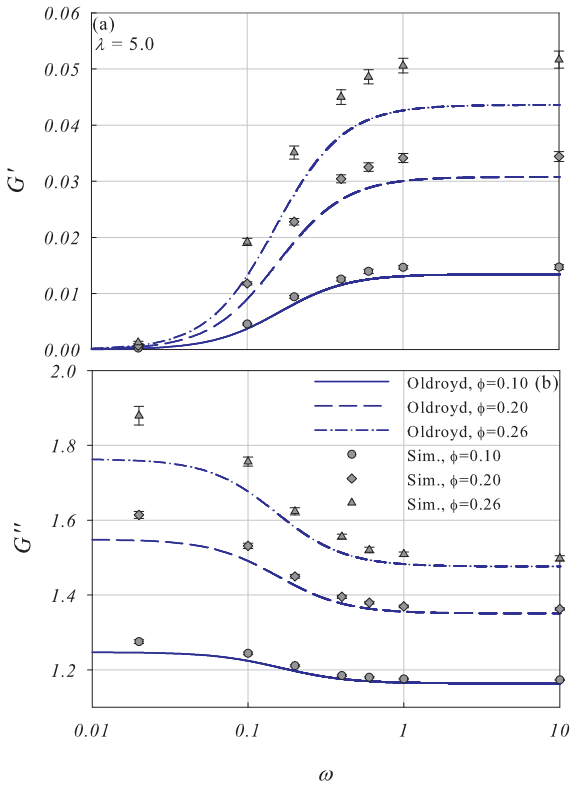

Figure 4.18: Elastic modulus G' (a) and loss modulus G'' (b) as a function of frequency ω, and for three values of the volume fraction ϕ, for an emulsion of Newtonian drops in a Newtonian matrix in the linear regime. Blue curves: theoretical predictions from [78]. There is no interfacial slip between the suspended drops and the matrix, the viscosity ratio is chosen as $\lambda = 5.0$, ω-axis is log-scale.

oretical results for $\lambda = 5.0$, and again for $\phi = 0.10, 0.20, 0.26$. In panel (a), it can be seen that our simulations have the same qualitative $G'(\omega)$ trend as Oldroyd's predictions for every ϕ, but, beyond the dilute regime, the computational results lie above the theoretical ones, the deviations being larger as the volume fraction and the frequency are increased (the largest discrepancy - about 20% - is got for $\phi = 0.26$ and $\omega = 10.0$). In panel (b), results on G'' are reported, from which a qualitative difference with respect to the cases of $\lambda = 0.1$ and $\lambda = 1.0$ emerges. Indeed, simulations show that for $\lambda = 5.0$, G'' grows with ϕ over the whole ω-range explored. For such λ-value, this is also

predicted by Oldroyd's model. Numerical points slightly overcome Oldroyd's theoretical curves.

In [27], the frequency response of an emulsion of PDMS300 drops in a PIB2300 matrix is experimentally studied; the viscosity ratio of the system is 0.5, and the volume fraction is 5%. If the data presented in such paper are made dimensionless in the same way as ours, a quantitative agreement is found for both G' and G'' when the same flow conditions are experienced.

4.3.2 The case with slip

According to Oldroyd's model, in an emulsion, the effect of interfacial slip between the drops and the suspending matrix, which is modulated by the slip parameter α, that can range from 0 (no-slip) to ∞ (free slipping drops), is increasingly more visible as the viscosity ratio, the frequency, and the volume fraction increase. In Figures 4.19 and 4.20, the elastic modulus G' (upper panel) and loss modulus G'' (lower panel) are shown as a function of ϕ for $\lambda = 1.0$ (Figure 4.19) and $\lambda = 5.0$ (Figure 4.20), $\omega = 1.0$, and two values of the slip parameter α, i.e, $\alpha = 0.1$, 1.0. In these figures, our data are displayed as symbols with error bars, whereas the corresponding Oldroyd's predictions are shown as solid curves of the same color. Each datum represents the average of the results of 5 simulations with different random initial positions of the drops at the same ϕ, ω, λ, and α. The analytical expressions of $G'(\lambda, \phi, \omega, \alpha)$ and $G''(\lambda, \phi, \omega, \alpha)$ derived from [78] in the case with interfacial slip are reported explicitly in Appendix B. Very recently, such theoretical predictions have been confirmed for vanishing ϕ by Ramachandran et al (see [86, 85]).

In Figure 4.19, the trends of $G'(\lambda = 1.0, \omega = 1.0)$ and $G''(\lambda = 1.0, \omega = 1.0)$ as a function of ϕ are reported for $\alpha = 0.1$ (black symbols) and $\alpha = 1.0$ (red symbols). It emerges from panel (a) that, as the slip parameter increases, i.e., there is more slip at the drop-matrix interfaces, the elastic modulus of the emulsion decreases: this is expectable and can be ascribed to the fact that the more slip there is, the less the drops deform (see [85]), and

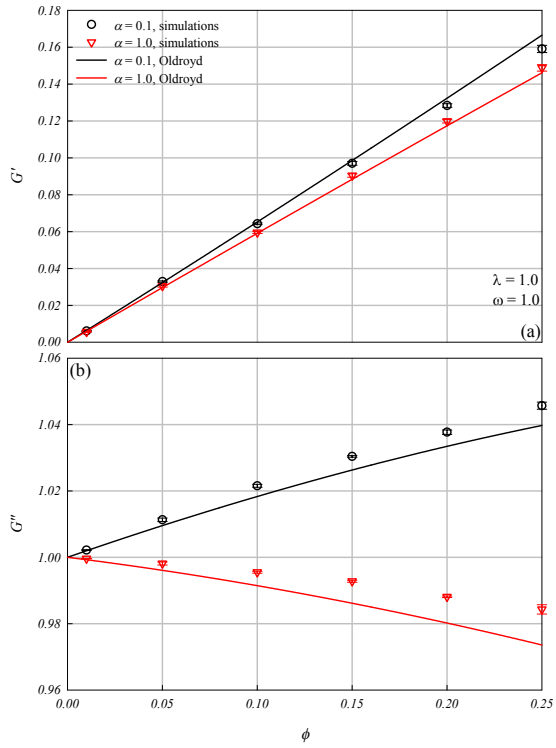

Figure 4.19: Elastic modulus G' (a) and loss modulus G'' (b) as a function of volume fraction ϕ for an emulsion of Newtonian drops in a Newtonian matrix in the linear regime. Black curve: theoretical predictions from [78] for $\alpha = 0.1$; red curve: theoretical predictions from [78] for $\alpha = 1.0$. The viscosity ratio is chosen as $\lambda = 1.0$, the frequency is $\omega = 1.0$.

it is the deformation of the drops that gives rise to the elastic behavior of emulsions. For both the values of the slip parameter, the simulation results are in excellent quantitative agreement with Oldroyd's predictions in the whole range of ϕ-values explored, also well outside the dilute regime, the highest discrepancy being of 4.5% at $\phi = 0.25$, $\alpha = 0.1$. For G'' (panel (b)), a decrease at increasing α is also detected; like for G', such result is expected, because interfacial slip lowers the effective viscosity of an emulsion (see again [85]), thus the loss modulus. Moreover, a change in the qualitative trend of the *modulus* is seen as interfacial slip increases; indeed, for $\alpha = 0.1$, G'' increases with ϕ, but, when α is equal to 1.0, $G''(\phi)$ is decreasing. Such

qualitative behavior is shown by both our numerical data and Oldroyd's predictions, with quantitative differences always within 10% as ϕ increases.

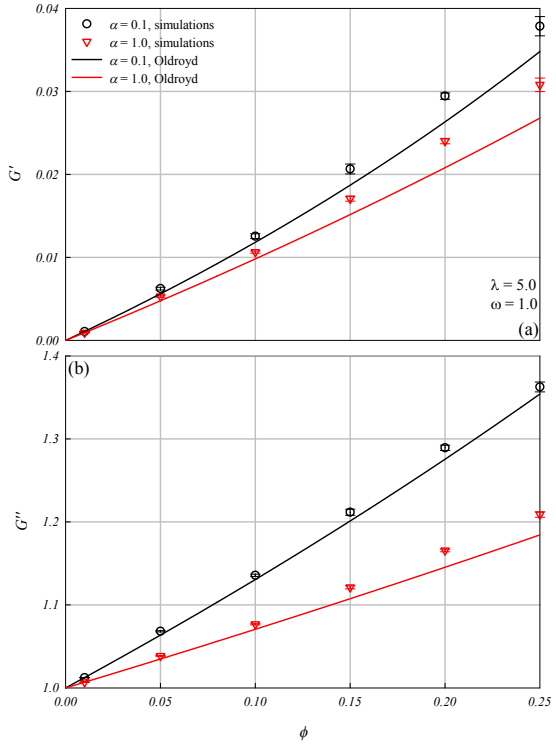

Figure 4.20: Elastic modulus G' (a) and loss modulus G'' (b) as a function of volume fraction ϕ for an emulsion of Newtonian drops in a Newtonian matrix in the linear regime. Black curve: theoretical predictions from [78] for $\alpha = 0.1$; red curve: theoretical predictions from [78] for $\alpha = 1.0$. The viscosity ratio is chosen as $\lambda = 5.0$, the frequency is $\omega = 1.0$.

In Figure 4.20, the trends of G' and G'' as a function of ϕ are reported for $\lambda = 5.0$, $\omega = 1.0$, and $\alpha = 0.1$ (black symbols), 1.0 (red symbols). Again, increasing slip decreases the two *moduli* of the emulsion. In panel (a), G' is displayed: a fair qualitative agreement emerges between numerical and theoretical points for both the α-values considered, with the theory progressively underestimating the modulus with respect to simulations as ϕ goes beyond the diluted regime (at $\phi = 0.25$, $\alpha = 0.1$, the discrepancy is about 13%). For what matters G'' (panel (b)), at variance to what shown in Figure 4.19, Oldroyd's model predicts no qualitative change in the $G''(\phi)$-trend as α in-

creases, since the red curve stays below the black one, but the sign of their slopes is the same. The agreement between Oldroyd's model and computational outcomes is quantitative in the whole range of concentration explored, the differences between points and curves being always below 2%.

4.4 Final remarks

In this chapter, the viscoelastic *moduli* of monodisperse emulsions of Newtonian drops in a Newtonian matrix subjected to Small Amplitude Oscillatory Shear flow are computed by means of arbitrary Lagrangian Eulerian finite element method 3D numerical simulations for a drop-to-matrix viscosity ratio in the range $10^{-1} - 10^{2}$, a volume fraction of the dispersed phase up to the concentrated regime (~ 0.3), and a dimensionless frequency of the forcing wave in the range $0.02 - 10$, also in the presence of interfacial slip between the drops and the suspending matrix.

In the no-slip case, at low frequency (e.g. $\omega = 0.4$ in Figures 4.11 - 4.15), the simulations predict increasing values of both the *moduli* as the volume fraction goes up. At any given ϕ, an increase in λ has an opposite effect on the *moduli*, enhancing G'' and suppressing G'.

For what matters the frequency response (Figures 4.16 - 4.18), if we make ω change at fixed λ and ϕ, we see that the numerical results show opposite trends of the two *moduli*: indeed, G' increases with ω, whereas G'' decreases with it. Increasing ϕ makes G' increase at every ω regardless λ. The behavior of G'' is, instead, quite peculiar: at low λ-s, at low frequencies G'' increases with ϕ, the opposite occurring at high frequencies (see Figure 4.16b); at high λ-s, G'' always increases with ϕ, i.e., over the whole ω-range considered (see Figure 4.18b).

The simulations yield that the presence of interfacial slip between the drops and the suspending matrix lowers both the *moduli*. Such effect, governed by the slip parameter α, is increasingly more visible as the viscosity ratio, the frequency, and the volume fraction increase, as shown in Figures

4.19 and 4.20.

All such numerical findings, both in the case without slip and with slip, agree with Oldroyd's predictions, the agreement in fact being quantitative in a wide range of ϕ- and ω-values, when λ is low or moderate. At high λ-values, trends shown by the numerical simulations always qualitatively agree with Oldroyd's predictions, but the quantitative agreement is lacking.

We are now in position to comment on the validity of Oldroyd's theory. Indeed, Oldroyd himself declared that his theory can be considered reliable only in the dilute regime, but not outside it, because it fails to reproduce known results beyond the dilute regime when λ diverges, i.e., when drops become analogous to hard spheres. Our simulations, in fact, confirm that Oldroyd's theory does not work for ϕ outside the dilute regime at very high λ-s (see the extreme case $\lambda = 100.0$ displayed in Figure 4.15). This occurrence is perhaps to be attributed to hydrodynamic interactions among the 'hard spheres', which are neglected in Oldroyd's approach, while being automatically included in the simulations. On the other hand, the fair agreement between our numerical data and Oldroyd's analytical predictions at 'ordinary' λ-values, valid from dilute to concentrated emulsions, lets us argue that a too extreme conclusion had been drawn by the author in his original paper. Apparently, the exclusion of hydrodynamic interactions in Oldroyd's analytical calculations has in practice no effects when ordinarily deformable drops are considered.

In conclusion, Oldroyd's theory can be considered reliable in a wide range of volume fractions, well outside the low-ϕ regime, when the viscosity contrast of the dispersed and the continuous phase is up to order unity. Also, within the same limitations concerning the λ-value (i.e., for $\lambda \leq 1$), we numerically validate, for the first time, Oldroyd's complete theory over a wide range of concentrations and frequencies in the presence of interfacial slip.

In view of the fair agreement between our numerical simulations and Oldroyd's complete theory, the predictions of models that, reduced to the case of Newtonian drops and matrix, give similar results to it (e.g., Palierne

[80], Bousmina [10]) will also agree with our results. Needless to say that, since we quantitatively agree with Oldroyd's predictions over a wide range of values of the considered parameters, no quantitative agreement will be found with theories yielding results different from Oldroyd's.

Chapter 5

Conclusions

In this thesis, a finite element method-based code is developed and applied to study the dynamics of soft systems (e.g., drops, elastic particles) suspended in Newtonian and viscoelastic fluids under flow.

In Chapter 2, an arbitrary Lagrangian Eulerian finite element method based numerical code for viscoelastic fluids using well-known stabilization techniques (SUPG, DEVSS, log-conformation) is adapted and extended to study the behavior of soft systems, such as liquid drops and elastic particles, suspended in flowing media in 3D.

Both drops and elastic particles are modeled as fluids (the particles being treated as drops of upper-convected Maxwell fluid with a very large relaxation time): for this reason, the interface between the suspended objects and the matrix needs to be tracked. To do this, a finite element method with second-order time discretization is defined on the interface, where its normal velocity equals the normal component of the fluid velocity, and the tangential velocity is such that the distribution of the elements on the interface is optimized. The advantage of this approach is that at the interface the mesh does not follow the tank-treading motion of the particle, thus greatly reducing the distortion of the ALE volume mesh as compared to a Lagrangian description of the interface. In order to stabilize the interface, the SUPG method is used.

A validation of the code is done for soft systems suspended in Newtonian

fluids under unbounded shear flow: for a Newtonian drop, in the absence of interfacial slip, our results are compared with Taylor predictions [95], and experimental data from Guido and Villone [49]; in the case with slip, we compare with the theoretical predictions from Ramachandran and Leal [85]; for an upper-convected Maxwell drop in a Newtonian matrix, numerical data are compared with the front tracking finite difference simulations from Aggarwal and Sarkar [1]; for a neo-Hookean elastic particle, simulation outcomes are compared with theoretical predictions by Roscoe [90] and Gao et al [36]. In all the above mentioned cases, a very good quantitative agreement is found between the results by other authors and ours.

In Chapter 3, the code is applied to a single-body problem: the deformation and cross-streamline migration of an initially spherical neo-Hookean elastic particle suspended in confined shear flow of Newtonian and Giesekus viscoelastic fluids is studied by means of 3D arbitrary Lagrangian Eulerian finite element method numerical simulations.

When suspended in a Newtonian fluid in a symmetric position with respect to the moving walls of the shear flow cell, the particle is found to deform until it attains a steady ellipsoid-like deformed shape, with a fixed orientation with respect to the flow direction. The two dimensionless parameters that govern the phenomenon are the elastic capillary number Ca_{e}, that relates the viscous forces acting on the particle and its elasticity, and the geometric blockage ratio β. The effects of such parameters on the steady deformation and orientation of the channel-mid plane-centered elastic particle are investigated: it is found that both Ca_{e}- and β-increases lead to a more deformed steady shape, and a more pronounced flow-alignment.

If the particle is initially suspended in a Newtonian liquid closer to a wall of the channel than to the other, it migrates transversally to the flow direction towards the center plane of the channel. For any given couple of values of the parameters β and Ca_{e}, a master curve describes the migration velocity trend as a function of the particle vertical position in the gap of the channel, with the migration velocity increasing as the particle is closer to

a wall. Out of the center plane of the flow cell, the deformed shape of the particle is found to be asymmetric, with the portion of its surface exposed to the fluid from the side of the wall slightly overcoming the portion of the surface exposed from the side of the center of the channel. Another master curve quantitatively describes such surface imbalance as a function of the particle vertical position over the gap of the channel, for any fixed $\beta - Ca_{\mathrm{e}}$ couple: the surface imbalance is larger as the particle is closer to the wall.

When the elastic particle is suspended in a sheared Giesekus viscoelastic fluid, its steady deformation and orientation angle will depend on β, Ca_{e} and on the new parameter p, which measures the relative weight of the elastic and viscous forces in the matrix. The effects of such parameters are investigated. In the simple case $\beta = 0$ (unbounded shear), it is found that a Ca_{e}-increase leads to both a more pronounced deformation and flow-alignment of the particle, whereas p contrasts deformation and promotes flow-alignment.

Like in a Newtonian fluid, also in a viscoelastic matrix the particle is found to migrate transversally to the flow direction when initially suspended out of the symmetry plane of the flow cell. Depending now on the value of p, however, the equilibrium position 'attracting' such migration changes. Indeed, low p-s promote migration towards the center plane, whereas high p-s promote migration towards the walls. For p below 10, the competition between the effects of the viscous and the elastic forces acting on the particle results in an equilibrium height in between the center plane and the wall.

Finally, in Chapter 4, a multi-body problem is considered: the viscoelastic *moduli* of monodisperse emulsions of Newtonian drops in a Newtonian matrix subjected to Small Amplitude Oscillatory Shear flow are computed by means of arbitrary Lagrangian Eulerian finite element method 3D numerical simulations for a drop-to-matrix viscosity ratio in the range $10^{-1} - 10^{2}$, a volume fraction of the dispersed phase up to the concentrated regime (~ 0.3), and a dimensionless frequency of the forcing wave in the range $0.02 - 10$, also in the presence of interfacial slip between the drops and the suspending matrix.

In the no-slip case, at low frequency, the simulations predict increasing values of both the *moduli* as the volume fraction goes up. At any given ϕ, an increase in λ has an opposite effect on the *moduli*, enhancing G'' and suppressing G'.

For what matters the frequency response, if we make ω change at fixed λ and ϕ, we see that the numerical results show opposite trends of the two *moduli*: indeed, G' increases with ω, whereas G'' decreases with it. Increasing ϕ makes G' increase at every ω regardless λ. The behavior of G'' is, instead, quite peculiar: at low λ-s, at low frequencies G'' increases with ϕ, the opposite occurring at high frequencies; at high λ-s, G'' always increases with ϕ, i.e., over the whole ω-range considered.

The simulations yield that the presence of interfacial slip between the drops and the suspending matrix lowers both the *moduli*. Such effect, governed by the slip parameter α, is increasingly more visible as the viscosity ratio, the frequency, and the volume fraction increase.

All such numerical findings, both in the case without slip and with slip, agree with Oldroyd's predictions, the agreement in fact being quantitative in a wide range of ϕ- and ω-values, when λ is low or moderate. At high λ-values, trends shown by the numerical simulations always qualitatively agree with Oldroyd's predictions, but the quantitative agreement is lacking. Then, Oldroyd's theory can be considered reliable in a wide range of volume fractions, well outside the low-ϕ regime, when the viscosity contrast of the dispersed and the continuous phase is up to order unity. Also, within the same limitations concerning the λ-value (i.e., for $\lambda \leq 1$), we numerically validate, for the first time, Oldroyd's complete theory over a wide range of concentrations and frequencies in the presence of interfacial slip.

In conclusion, the code presented in this thesis shows to be very flexible, and capable of treating in a robust and detailed way several soft systems of technological interest, even in the presence of confinement and rheological complexity. At the moment, its main limitation is given by the impossibility of treating very large deformations, such as the ones detected in [93] or Large

Amplitude Oscillatory Shear (LAOS) flow of emulsions, that would make the FEM meshes distort too much and, consequently, the simulations crash. To do this, a 3D remeshing algorithm will need to be implemented, that is a challenging issue, due to the necessity of mapping an arbitrarily deformed shape, where no analytical description is available. Future work will also include the analysis of different systems (e.g., cells) and flow regimes (e.g., tube flow), that are of great interest in the field of microfluidics.

Appendix A

Oldroyd's formulas in the no-slip case

From [78], in the absence of interfacial slip between the drops and the matrix, the following expressions for the *moduli* of a monodisperse emulsion of Newtonian drops in a Newtonian fluid subjected to Small Amplitude Oscillatory Shear flow can be derived:

$$G' = \frac{(\eta\tau - \xi)\omega^2}{1 + \tau^2\omega^2} \tag{A.1}$$

$$G'' = \frac{\eta\omega + \xi\tau\omega^3}{1 + \tau^2\omega^2} \tag{A.2}$$

where η is the overall viscosity of the emulsion, τ is its relaxation time, and ξ is a further parameter 'naturally' arising in Oldroyd's deduction. Such quantities can be in turn expressed as follows:

$$\eta = \eta_{\mathrm{m}} \frac{10(\lambda + 1) + 3(5\lambda + 2)\phi}{10(\lambda + 1) - 2(5\lambda + 2)\phi} \tag{A.3}$$

$$\tau = \frac{1}{4}\tau_{\mathrm{em}} \frac{(19\lambda + 16)[2\lambda + 3 - 2(\lambda - 1)\phi]}{10(\lambda + 1) - 2(5\lambda + 2)\phi} \tag{A.4}$$

$$\xi = \frac{1}{4}\eta_{\mathrm{m}}\tau_{\mathrm{em}} \frac{(19\lambda + 16)[2\lambda + 3 + 3(\lambda - 1)\phi]}{10(\lambda + 1) - 2(5\lambda + 2)\phi} \tag{A.5}$$

with η_{m} the viscosity of the matrix, λ the ratio between the viscosities of the drops and the suspending phase, ϕ the volume fraction of the suspended

phase, and $\tau_{\mathrm{em}} = \frac{\eta_{\mathrm{m}} R_{\mathrm{d}}}{\Gamma}$ the *emulsion time* (where R_{d} is the initial radius of the monodisperse drops, and Γ is the interfacial tension between the two liquids). The blue curves displayed in Figures 4.11 - 4.18 are built according to these laws.

Appendix B

Oldroyd's formulas in the case with interfacial slip

Even in the case where interfacial slip acts between the suspended drops and the suspending matrix, Equations (A.1) and (A.2) still hold true. Instead, the expressions of η, τ, and ξ become:

$$\eta = \eta_{\mathrm{m}} \frac{10(\lambda+1) + 3(5\lambda+2)\phi + 10\alpha\lambda(3\phi+5)}{10(\lambda+1) - 2(5\lambda+2)\phi + 10\alpha\lambda(5-2\phi)} \tag{B.1}$$

$$\begin{aligned}\tau = &\frac{1}{4}\tau_{\mathrm{em}} \frac{(19\lambda+16)[2\lambda+3-2(\lambda-1)\phi]}{10(\lambda+1) - 2(5\lambda+2)\phi + 10\alpha\lambda(5-2\phi)} + \\ &\frac{1}{4}\tau_{\mathrm{em}} \frac{2\alpha\lambda[2(19\lambda-40)\phi - 5(19\lambda+24)]}{10(\lambda+1) - 2(5\lambda+2)\phi + 10\alpha\lambda(5-2\phi)}\end{aligned} \tag{B.2}$$

$$\begin{aligned}\xi = &\frac{1}{4}\eta_{\mathrm{m}}\tau_{\mathrm{em}} \frac{(19\lambda+16)[2\lambda+3+3(\lambda-1)\phi]}{10(\lambda+1) - 2(5\lambda+2)\phi + 10\alpha\lambda(5-2\phi)} + \\ &\frac{1}{4}\eta_{\mathrm{m}}\tau_{\mathrm{em}} \frac{2\alpha\lambda[3(19\lambda-40)\phi + 5(19\lambda-24)]}{10(\lambda+1) - 2(5\lambda+2)\phi + 10\alpha\lambda(5-2\phi)}\end{aligned} \tag{B.3}$$

with η_{m} the viscosity of the matrix, λ the ratio between the viscosities of the drops and the suspending phase, ϕ the volume fraction of the suspended phase, $\tau_{\mathrm{em}} = \frac{\eta_{\mathrm{m}} R_{\mathrm{d}}}{\Gamma}$ the *emulsion time* (where R_{d} is the initial radius of the monodisperse drops, and Γ is the interfacial tension between the two liquids), and α the dimensionless slip parameter (see Section 4.3). The black and red curves displayed in Figures 4.19 - 4.20 are built according to these laws.

Bibliography

[1] Aggarwal, N., Sarkar, K.. Deformation and breakup of a viscoelastic drop in a Newtonian matrix under steady shear. J. Fluid Mech. 2007;584:1-21.

[2] Aggarwal, N., Sarkar, K.. Effects of matrix viscoelasticity on viscous and viscoelastic drop deformation in a shear flow. J. Fluid Mech. 2008;601:63-84.

[3] Bagchi, P.. Mesoscale Simulation of Blood Flow in Small Vessels. Biophys. J. 2007;92:1858-1877.

[4] Barthes-Biesel, D., Rallison, J.. The time-dependent deformation of a capsule freely suspended in a linear shear flow. J. Fluid. Mech. 1981;113:251-267.

[5] Batchelor, G.K.. The stress system in a suspension of force free particles. J. Fluid Mech. 1970;41:545-570.

[6] Bawzdziewicz, J., Cristini, V., Loewenberg, M.. Critical behavior of drops in linear flows. I. Phenomenological theory for drop dynamics near critical stationary states. Phys. Fluids 2002;14:2709-2718.

[7] Bawzdziewicz, J., Cristini, V., Loewenberg, M.. Multiple stationary states for deformable drops in linear Stokes flows. Phys. Fluids 2003;15:37-40.

[8] Bogaerds, A., Grillet, A., Peters, G., Baaijens, F.. Stability analysis of polymer shear flows using the extended pom-pom constitutive equations. J. Non-Newtonian Fluid Mech. 2002;108:187-208.

[9] Bogaerds, A., Hulsen, M., Peters, G., Baaijens, F.. Time dependent finite element analysis of the linear stability of viscoelastic flows with interfaces. J. Non-Newtonian Fluid Mech. 2003;116:33-54.

[10] Bousmina, M.. Rheology of polymer blends: linear model for viscoelastic emulsions. Rheol. Acta 1999;38:73-83.

[11] Bousmina, M., Palierne, J.F., Utracki, L.A.. Modeling of structured polyblend flow in laminar shear field. Polym. Eng. Sci. 1999;39:1049-1059.

[12] Brooks, A., Hughes, T.. Streamline upwind/Petrov-Galerkin formulations for convection dominated flows with particular emphasis on the incompressible Navier-Stokes equations. Comp. Meth. Appl. Mech. Eng. 1982;32:199-259.

[13] Chaffey, C.E., Brenner, H.. A second-order theory for shear deformation of drops. J. Colloid Interface Sci. 1967;24:258-269.

[14] Chinyoka, T., Renardy, Y., Renardy, M., Khismatullin, D.B.. Two-dimensional study of drop deformation under simple shear for Oldroyd-B liquids. J. Non-Newtonian Fluid Mech. 2005;130:45-56.

[15] Choi, Y., Hulsen, M.. Simulation of extrudate swell using an extended finite element method. Korea-Australia Rheol. J. 2011;23:147-154.

[16] Choi, J.C., Schowalter, W.R.. Rheological properties of nondilute suspensions of deformable particles. Phys. Fluids 1975;18:420-427.

[17] Coupier, G., Kaoui, B., Podgorski, T., Misbah, C.. Noninertial lateral migration of vesicles in bounded Poiseuille flow. Phys. Fluids 2008;20:111702.

[18] Cristini, V., Bawzdziewicz, J., Loewenberg, M.. Drop breakup in three-dimensional viscous flows. Phys. Fluids 1998;10:1781-1783.

[19] Cristini, V., Guido, S., Alfani, A., Bawzdziewicz, J., Loewenberg, M.. Drop breakup and fragment size distribution in shear flow. J.Rheol. 2003;47:1283-1298.

[20] Das, C., Wang, H., Mewis, J., Moldenaers, P.. Rheology and microstructures formation of immiscible model polymer blends under steady state and transient flows. J. Polym. Sci. B: Polym. Phys. 2005;43:3519-3533.

[21] D'Avino, G., Greco, F., Hulsen, M.A., Maffettone, P.L.. Rheology of viscoelastic suspensions of spheres under small and large amplitude oscillatory shear by numerical simulations. J Rheology 2013;57:813-839.

[22] D'Avino, G., Hulsen, M.. Decoupled second-order transient schemes for the flow of viscoelastic fluids without a viscous solvent contribution. J. Non-Newtonian Fluid. Mech. 2010;165:1602-1612.

[23] D'Avino, G., Maffettone, P.L., Hulsen, M.A., Peters, G.W.M.. A numerical method for simulating concentrated rigid particle suspensions in an elongational flow using a fixed grid.. J. Comput. Phys. 2007;226:688-711.

[24] D'Avino, G., Maffettone, P.L., Hulsen, M.A., Peters, G.W.M.. Numerical simulation of planar elongational flow of concentrated rigid particle suspensions in a viscoelastic fluid. J. Non-Newtonian Fluid Mech. 2008;150:65-79.

[25] D'Avino, G., Maffettone, P.L., Greco, F., Hulsen, M.A.. Viscoelasticity-induced migration of a rigid sphere in confined shear flow. J Non-Newtonian Fluid Mech 2010;165:466-474.

[26] D'Avino, G., Romeo, G., Villone, M.M., Greco, F., Netti, P.A., Maffettone, P.L.. Single line particle focusing induced by viscoelasticity of the suspending liquid: theory, experiments and simulations to design a micropipe flow-focuser. Lab Chip 2012;12:1638-1645.

[27] Deyrail, Y., El Mesri, Z., Huneault, M., Zeghloul, A., Bousmina, M.. Analysis of morphology development in immiscible newtonian polymer mixtures during shear flow. J. Rheology 2007;51:781-797.

[28] Dittrich, P.S., Manz, A.. Lab-on-a-chip: microfluidics in drug discovery. Nature Reviews Drug Discovery 2006;5:210-218.

[29] Doddi, S.K., Bagchi, P.. Lateral migration of a capsule in a plane Poiseuille flow in a channel. Int. J. Multiphase Flow 2008;34:966-986.

[30] Eshelby, J.D.. The determination of the elastic eld of an ellipsoidal inclusion, and related problems. Proc. R. Soc. Lond. A 1957;241:376-396.

[31] Eshelby, J.D.. The elastic eld outside an ellipsoidal inclusion. Proc. R. Soc. Lond. A 1959;252:561-569.

[32] Fattal, R., Kupferman, R.. Constitutive laws for the matrix-logarithm of the conformation tensor. J. Non-Newtonian Fluid Mech. 2004;123:281-285.

[33] Finken, R., Kessler, S., Seifert, U.. Micro-capsules in shear flow. J. Phys. Condens. Matter 2011;23:1-18.

[34] Frölich, H., Sack, R.. Theory of the rheological properties of dispersions. Proc. R. Soc. Lond. A 1946;185:415-430.

[35] Gao, T., Hu, H.H.. Deformation of elastic particles in viscous shear flow.. J. Comput. Phys. 2009;228:2132-2151.

[36] Gao, T., Hu, H.H., Ponte Castaneda, P.. Rheology of a suspension of elastic particles in a viscous shear flow. J. Fluid Mech. 2011;687:209-237.

[37] Gao, T., Hu, H.H., Ponte Castaneda, P.. Shape Dynamics and Rheology of Soft Elastic Particles in a Shear Flow. Phys. Rev. Lett. 2012;108:058302.

[38] Geuzaine, C., Remacle, J.F.. Gmsh: A 3-d finite element mesh generator with built-in pre- and post- processing facilities. Internat. J. Numer. Methods Engrg. 2009;79:1309-1331.

[39] Goddard, J.D., Miller, C.. Nonlinear effects in the rheology of dilute suspensions. J. Fluid Mech. 1967;28:657-673.

[40] Goldsmith, H., Marlow, J.. Flow behavior of erythrocytes. I. Rotation and deformation in dilute suspensions. Proc. R. Soc. Lond. B 1972;182:351-384.

[41] Graebling, D., Muller, R., Palierne, J.F.. Linear viscoelastic behavior of some incompatible polymer blends in the melt. Interpretation of data with a model of emulsion of viscoelastic liquids. Macromolecules 1993;26:320-329.

[42] Grajewski, M.K., Turek, S.. Mathematical and numerical analysis of a robust and efficient grid deformation method in the finite element context. SIAM J. Sci. Comp. 2009;31:1539-1557.

[43] Greco, F.. Drop deformation for non-Newtonian fluids in slow flows. J. Non-Newtonian Fluid Mech. 2002;107:111-131.

[44] Griggs, A.J., Zinchenko, A.Z., Davis, R.H.. Low-Reynolds-number motion of a deformable drop between two parallel plane walls. Int. J. Multiphase Flow 2007;22:187-206.

[45] Guenette, R., Fortin, M.. A new mixed finite element method for computing viscoelastic flows. J. Non-Newtonian Fluid Mech. 1995;60:27-52.

[46] Guido, S., Greco, F.. Dynamics of a liquid drop in a flowing immiscible liquid. Rheology Reviews 2004; 99-142.

[47] Guido, S., Preziosi, V.. Droplet deformation under confined Poiseuille flow. Adv. Colloid Interface Sci. 2010;161:89-101.

[48] Guido, S., Simeone, M., Greco, F.. Deformation of a Newtonian drop in a viscoelastic matrix under steady shear flow Experimental validation of slow flow theory.. J. Non-Newtonian Fluid Mech. 2003;114: 65-82.

[49] Guido, S., Villone, M.. Three-dimensional shape of a drop under simple shear flow. J. Rheol. 1998;42:395-415.

[50] Hooper, R., Toose, M., Macosko, C.W., Derby, J.J.. A comparison of boundary element and finite element methods for modeling axisymmetric polymeric drop deformation. Int. J. Numer. Meth. Fluids 2001;37:837-864.

[51] Hooper, R., de Almeida, V.F., Macosko, C.W., Derby, J.J.. Transient polymeric drop extension and retraction in uniaxial extensional flows. J. Non-Newtonian Fluid Mech. 2001;98:141-168.

[52] Hu, H., Patankar, N., Zhu, M.. Direct numerical simulations of fluid-solid systems using the arbitrary Lagrangian-Eulerian technique. J. Comput. Phys. 2001;169:427-462.

[53] Hulsen, M., Fattal, R., Kupferman, R.. Flow of viscoelastic fluids past a cylinder at high Weissenberg number: stabilized simulations using matrix logarithms. J. Non-Newtonian Fluid Mech. 2005;127:27-39.

[54] Huo, Y., Groeninckx, G., Moldenaers, P.. Rheology and morphology of polystyrene/polypropylene blends with in situ compatibilization. Rheol. Acta 2007;46:507-520.

[55] Janssen, P.J.A., Anderson, P.D.. Surfactant-covered drops between parallel plates. Chem. Eng. Research & Design 2008;86:1388-1396.

[56] Kaoui, B., Biros, G., Misbah, C.. Why Do Red Blood Cells Have Asymmetric Shapes Even in a Symmetric Flow?. Phys. Rev. Lett. 2009;103:188101.

[57] Kaoui, B., Ristow, G.H., Cantat, I., Misbah, C., Zimmermann, W.. Lateral migration of a two-dimensional vesicle in unbounded Poiseuille flow. Phys. Rev. E 2008;77:021903.

[58] Kennedy, M.R., Pozrikidis, C., Skalak, R.. Motion and deformation of liquid drops, and the rheology of dilute emulsions in simple shear flow. Comput. Fluids 1994;23:251-278.

[59] Keunings, R.. An algorithm for the simulation of transient viscoelastic flows with free surfaces. J. Comput. Phys. 1986;62:199-220.

[60] Kitade, S., Ichikawa, A., Imura, N., Takahashi, Y., Noda, I.. Rheological properties and domain structures of immiscible polymer blends under steady and oscillatory shear flows 1997. J. Rheology 1997;41:1039-1060.

[61] Lam, Y.C., Jiang, L., Tue, C.Y., Tam, K.C., Li, L.. Interfacial slip between polymer melts studied by confocal microscopy and rheological measurements. J. Rheol 2003;47:795-807.

[62] Lan, H., Khismatullin, D.B.. A numerical study of the lateral migration and deformation of drops and leukocytes in a rectangular microchannel. Int. J. Multiphase Flow 2012;47:73-84.

[63] Larson, R.G.. The structure and rheology of complex fluids. Oxford University Press 1999.

[64] Lee, P.C., Park, H.E., Morse, D.C., Macosko, C.W.. Polymer-polymer interfacial slipin multilayered films. J. Rheol. 2009;53:893-915.

[65] Levitt., L., Macosko, C.M., Pearson, S.D.. Influence of Normal Stress Difference on Polymer Drop Deformation. Polym. Eng. and Sci. 1996;36:1647-1655.

[66] Li, H., Ma, G.. Modeling performance of a two-dimensional capsule in a microchannel flow: Long-term lateral migration. Phys. Rev. E 2010;82:026304.

[67] Li, X., Pozrikidis, C.. Wall-bounded shear flow and channel flow of suspensions of liquid drops. Int. J. Multiphase Flow 2000;26:1247-1279.

[68] Lin, C.C.. A mathematical model for viscosity in capillary extrusion of two-component polyblends. Polym. J. 1979;11:185-192.

[69] Luo, H., Pozrikidis, C.. Effect of surface slip on Stokes flow past a spherical particle in an infinite fluid and near a plane wall. J. Eng. Math. 2008;62:1-21.

[70] Lyngaae-Jorgensen, J., Thomsen, L.D., Rasmussen, K., Sondergaard, K., Andersen, F.E.. On the influence of interfacial slip on melt flow properties of polymer blends. Int. Polym. Process. 1988;2:123-130.

[71] Maffettone, P.L., Greco, F.. Ellipsoidal drop model for single drop dynamics with non-Newtonian fluids. J. Rheol. 2004;48:83-100.

[72] Maffettone, P.L., Minale, M.. Equation of change for ellipsoidal drops in viscous flow. J. Non-Newtonian Fluid Mech. 1998;78:227-241.

[73] Mortazavi, S., Tryggvason, G.. A numerical study of the motion of drops in Poiseuille flow. Part 1. Lateral migration of one drop. J. Fluid Mech. 2000;411:325-350.

[74] Mukherjee, S., Sarkar, K.. Effects of viscosity ratio on deformation of a viscoelastic drop in a Newtonian matrix under steady shear. J. Non-Newtonian Fluid Mech. 2009;160:104-112.

[75] Mukherjee, S., Sarkar, K.. Effects of matrix viscoelasticity on the lateral migration of a deformable drop in a wall-bounded shear. J. Fluid Mech. 2013;727:318-345.

[76] Murata, T.. Deformation of an elastic particle suspended in an arbitrary flow field. J. Phys. Soc. Japan 1981;50:1009-1016.

[77] Nawab, M,A,, Mason, S.G.. The preparation of uniform emulsion by electrical dispersion. J. Colloid Sci. 1958;13:179-187.

[78] Oldroyd, J.G.. The elastic and viscous properties of emulsions and suspensions. Proc. R. Soc. Lond. A 1953;218:122-132.

[79] Pal, R.. Rheology of polymer-thickened emulsions. J. Rheol. 1992;36:1245-1256.

[80] Palierne, J.F.. Linear rheology of viscoelastic emulsions with interfacial tension. Rheol. Acta 1999;29:204-214.

[81] Pamme, N.. Continuous flow separations in microfluidic devices. Lab Chip 2007; 7:1644-659.

[82] Park, H.E., Lee, P.C., Macosko, C.W.. Polymer-polymer interfacial slip by direct visualization and by stress reduction. J. Rheol. 2010;54:1207-1218.

[83] Pozrikidis, C.. Effects of surface viscosity on the finite deformation of a liquid drop and the rheology of dilute emulsions in simple shearing flow. J. Non-Newtonian Fluid Mech. 1994;51:161-178.

[84] Pozrikidis, C.. Numerical Simulation of Cell Motion in Tube Flow. Ann. Biomed. Eng. 2005;33:165-178.

[85] Ramachandran, A., Leal, L.G.. The effect of interfacial slip on the rheology of a dilute emulsion of drops for small Capillary numbers. J. Rheol. 2012;56:1555-1587.

[86] Ramachandran, A., Tsigklifis, K., Roy, A., Leal, L.G.. The effect of interfacial slip on the dynamics of a drop in flow: Part I. Stretching, relaxation, and breakup. J. Rheol. 2012;56:45-97.

[87] Renardy, Y.. Drop oscillations under simple shear in a highly viscoelastic matrix. Rheol. Acta 2008;47:89-96.

[88] Renardy, Y., Renardy, M., Assighaou, S., Benyahia, L.. Numerical simulation of drop retraction after a strain jump. Phys. Rev. E 2009;79:046323.

[89] Risso, F., Colle-Paillot, F., Zagzoule, M.. Experimental investigation of a bioartificial capsule flowing in a narrow tube. J. Fluid Mech. 2006;547:149-173.

[90] Roscoe, R.. On the rheology of a suspension of viscoelastic spheres in a viscous liquid.. J. Fluid Mech. 1967;28:273-293.

[91] Segre, G., Silberberg, A.. Radial Particle Displacements in Poiseuille Flow of Suspensions. Nature 1961;189:209-210.

[92] Shapira, M., Haber, S.. Low Reynolds number motion of a droplet in shear flow including wall effects. Int. J. Multiphase Flow 1990;16:305-321.

[93] Sibillo, V., Pasquariello, G., Simeone, M., Cristini, V., Guido, S.. Drop deformation in microconfined shear flow. Phys. Rev. Lett. 2006;97.

[94] Taylor, G.I.. The viscosity of a fluid containing small drops of another fluid. Proc. R. Soc. Lond. A 1932;138:41-48.

[95] Taylor, G.I.. The formation of emulsions in definable fields of flow. Proc. R. Soc. Lond. A 1934;6:501-523.

[96] Van Puyvelde, P., Velankar, S., Moldenaers, P.. Rheology and morphology of compatibilized polymer blends. Current Opinion in Colloid & Interface Science 2001;6:457-463.

[97] Verhulst, K., Cardinaels, R., Moldenaers, P., Afkhami, S., Renardy, Y.. Influence of viscoelasticity on drop deformation and orientation in shear flow. Part 2: Dynamics. J. Non-Newtonian Fluid Mech. 2009;156:44-57.

[98] Vinckier, I., Moldenaers, P., Mewis, J.. Transient rheological response and morphology evolution of immiscible polymer blends. J. Rheology 1997;41:705-718.

[99] Vitkova, V., Mader, M., Podgorski, T.. Deformation of vesicles flowing through capillaries. Europhys. Lett. 2004;68:398-404.

[100] Villone, M.M., D'Avino, G., Hulsen, M.A., Greco, F., Maffettone, P.L.. Simulations of viscoelasticity-induced focusing of particles in pressure-driven micro-slit flow. J. Non-Newtonian Fluid Mech. 2011;166:1396-1405.

[101] Wan, D., Turek, S.. Fictitious boundary and moving mesh methods for the numerical simulation of rigid particulate flows. J Comput Phys 2007;222:28-56.

[102] Yon, S., Pozrikidis, C.. A Finite-Volume/Boundary-Element Method for flow past interfaces in the presence of surfactants, with application to shear flow past a viscous drop. Comput. Fluids 1998;27:879-902.

[103] Zhao, R., Macosko, C.W.. Slip at polymer-polymer interface: rheological measurements on coextruded multilayers. J. Rheol. 2002;46:145-167.